



<https://theses.gla.ac.uk/>

Theses Digitisation:

<https://www.gla.ac.uk/myglasgow/research/enlighten/theses/digitisation/>

This is a digitised version of the original print thesis.

Copyright and moral rights for this work are retained by the author

A copy can be downloaded for personal non-commercial research or study,
without prior permission or charge

This work cannot be reproduced or quoted extensively from without first
obtaining permission in writing from the author

The content must not be changed in any way or sold commercially in any
format or medium without the formal permission of the author

When referring to this work, full bibliographic details including the author,
title, awarding institution and date of the thesis must be given

Enlighten: Theses

<https://theses.gla.ac.uk/>
research-enlighten@glasgow.ac.uk

ANALYSIS OF DEFECTIVE TUBULAR WELDED JOINTS

by

Christopher Wilson Hodgson

Department of Mechanical Engineering

University of Glasgow

Submitted for the Degree of MSc

June 1989

© CW Hodgson 1989

ProQuest Number: 10970926

All rights reserved

INFORMATION TO ALL USERS

The quality of this reproduction is dependent upon the quality of the copy submitted.

In the unlikely event that the author did not send a complete manuscript and there are missing pages, these will be noted. Also, if material had to be removed, a note will indicate the deletion.



ProQuest 10970926

Published by ProQuest LLC (2018). Copyright of the Dissertation is held by the Author.

All rights reserved.

This work is protected against unauthorized copying under Title 17, United States Code
Microform Edition © ProQuest LLC.

ProQuest LLC.
789 East Eisenhower Parkway
P.O. Box 1346
Ann Arbor, MI 48106 – 1346

<u>CONTENTS</u>	ii
<u>ACKNOWLEDGEMENTS</u>	x
<u>SUMMARY</u>	xi
<u>NOTATION</u>	xiii
1.0 <u>Introduction</u>	1
1.1 Computing Environment	3
<u>SECTION A: Stress Concentration in Butt Welds</u>	
2.0 <u>Introduction</u>	6
2.1 Background	6
2.2 Definitions	6
2.3 Aim	7
2.4 Experiments (The Welding Institute)	7
2.5 FE Stress Analyses	8
2.6 Previous Work	9
Annexe 2.1 Programme of stress analyses	13
Annexe 2.2 Detailed experimental geometries for comparisons	16
3.0 <u>Results</u>	24
3.1 2-D Results	24
3.1.1 Introduction	24
3.1.2 Comparisons with experimental results	24
3.1.3 FE Stress Analyses	26
3.1.4 Comparisons with parametric equations	28
3.2 3-D Results	30
3.2.1 Introduction	30
3.2.2 Comparisons with experimental results	30
3.2.3 FE Stress Analyses	31
3.3 2-D / 3-D Comparisons	32
Annexe 3.1 Experimental comparison	33
Annexe 3.2 Length and thickness ratio effect on 2-D models	34
Annexe 3.3 Theoretical comparisons	36
Annexe 3.4 Comparison of 2-D and 3-D results	38

4.0	<u>Discussion and Conclusions to Section A</u>	88
4.1	Discussion	88
4.2	Conclusion	89
<u>SECTION B: Failure in Tubular Welded Joints</u>		
5.0	<u>Introduction</u>	90
5.1	The problem	90
5.2	Previous work	90
6.0	<u>Computational Fracture Mechanics</u>	95
6.1	Crack driving force	95
6.2	Stress intensity factors	95
6.3	Computation of K	96
6.4	Virtual crack extension	97
6.5	Linesprings	98
6.6	EPFM	99
7.0	<u>Plane-strain Analyses</u>	107
7.1	Theoretical model	107
7.2	FE Modelling	107
7.3	Results	108
7.4	Conclusion	109
8.0	<u>3-D Analyses (straight crack)</u>	116
8.1	Theoretical model	116
8.2	FE Modelling	116
8.3	Results	116
8.4	Conclusion	117
9.0	<u>Tubular Joint Analyses</u>	122
9.1	Modelling	122
9.2	Results	125
9.3	Conclusion	127
Annexe 9.1	Experimental T-Joint and Crack Geometries	128
Annexe 9.2	Comparison of FE, experimental and theoretical SCF's	129
Annexe 9.3	Y for experimental crack geometries	130
Annexe 9.4	Stress Field at Saddle in T-Joint	131
Annexe 9.5	Stress Field in Flat Plate	132

10.0	<u>Discussion and Conclusions to Section B</u>	156
10.1	Discussion	156
10.2	Conclusion	156
<u>SECTION C: Grind Repair of Tubular Welded Joints</u>		
11.0	<u>Introduction</u>	158
11.1	Background	158
11.2	Aim	158
11.3	FE Stress analysis	158
12.0	<u>Results</u>	160
12.1	Presentation of Results	160
12.2	Preparatory Work	160
12.3	Analysis of BG Grooves	161
12.4	Analysis of TWI Grooves	162
Annexe 12.1	BG geometry; SCF at weld toe	163
Annexe 12.2	TWI geometry; SCF at weld toe	164
Annexe 12.3	BG geometry; SCF due to presence of groove	165
Annexe 12.4	BG geometry; reduction of fatigue life due to depth of groove	166
Annexe 12.5	TWI geometry; SCF due to presence of groove	167
13.0	<u>Discussion and Conclusions to Section C</u>	179
13.1	Discussion	179
13.2	Conclusion	180
14.0	<u>Overall Conclusions</u>	182
	<u>References</u>	184

Figures

fig 2.1a	Definition of t_1 , t_2 and transition ratio
fig 2.1b	Definition of positive and negative offset
fig 2.1c	Definition of positive and negative misalignment
fig 2.1d	Definition of global offset
fig 2.2a(i)	2-D boundary conditions - initial study (BC1)
fig 2.2a(ii)	2-D boundary conditions - initial study (BC2)
fig 2.2b	2-D boundary conditions - experimental comparisons and later study (BC3)
fig 2.2c	2-D - WI experimental strain gauge positions
fig 2.2d	3-D - WI experimental strain gauge positions
fig 2.3	Offset welded joint in a flat plate
fig 2.4	Misaligned welded joint in a flat plate
fig 3.1	Comparison of FE results with W3-10
fig 3.2	Comparison of FE results with W1-15
fig 3.3	Comparison of FE results with W4-25
fig 3.4	Comparison of FE results with W5-36
fig 3.5	Comparison of FE results with W9-47
fig 3.6a	Effect of varying length on offset SCF's
fig 3.6b	Effect of varying length on combined offset and misalignment SCF's
fig 3.6c	Effect of varying length and thickness ratio on combined offset and misalignment SCF's
fig 3.7	Stress along top surface of 2-D model
fig 3.8	Effect on SCF of varying transition ratio
fig 3.8a	Effect on SCF of varying transition ratio (BC1)
fig 3.8b	Effect on SCF of varying transition ratio (BC2)
fig 3.8c	Effect on SCF of varying transition ratio (BC3, SESAM results)
fig 3.8d	Effect on SCF of varying transition ratio (BC3, extrapolated results)
fig 3.9	Effect on SCF of varying thickness ratio
fig 3.9a	Effect on SCF of varying thickness ratio (BC1)
fig 3.9b	Effect on SCF of varying thickness ratio (BC2)
fig 3.9c	Effect on SCF of varying thickness ratio (BC3, SESAM results)
fig 3.9d	Effect on SCF of varying thickness ratio (BC3, extrapolated Results)
fig 3.9e	Effect on SCF of varying transition and thickness ratios (BC3, extrapolated results)

fig 3.10	Effect on SCF of varying offset
fig 3.10a	Effect on SCF of varying offset (BC1)
fig 3.10b	Effect on SCF of varying offset (BC2)
fig 3.10c	Effect on SCF of varying offset (BC3, SESAM results)
fig 3.10d	Effect on SCF of varying offset (BC3, extrapolated results)
fig 3.11	Effect on SCF of varying misalignment
fig 3.11a	Effect on SCF of varying misalignment (BC1)
fig 3.11b	Effect on SCF of varying misalignment (BC2)
fig 3.11c	Effect on SCF of varying misalignment (BC3, SESAM results)
fig 3.11d	Effect on SCF of varying misalignment (BC3, extrapolated results)
fig 3.12	Comparison of FE and theoretical results for offsets
fig 3.13	Comparison of FE and theoretical results for misalignments
fig 3.14	Accuracy of Eqns for varying offsets Accuracy of Eqns for varying misalignments
fig 3.15a	Comparison of FE results with 4 point bending test specimen: Applied force = 400kN
fig 3.15b	Comparison of FE results with 4 point bending test specimen: Applied force = 2800kN
fig 3.16a	SCF along inner surface of 3-D models; no offset or misalignment, showing effect of refining the mesh
fig 3.16b	SCF along inner surface of 3-D model near to weld; no offset or misalignment showing effect of refining the mesh
fig 3.17a	SCF along inner surface of 3-D model with -0.2 offset
fig 3.17b	SCF along inner surface of 3-D model with +0.2 offset
fig 3.18a	SCF along inner surface of 3-D model with -2.0° misalignment
fig 3.18b	SCF along inner surface of 3-D model with +2.0° misalignment
fig 3.19a	SCF along inner surface of 3-D model with offset and misalignment (offset -0.2, misalignment -2.0°)
fig 3.19b	SCF along inner surface of 3-D model with offset and misalignment (offset 0.2, misalignment 2.0°)
fig 3.20	Principal stress contour plot for 3-D model
fig 3.21	Principal stress contour plot for 3-D model with offset
fig 3.22	Principal stress contour plot for 3-D model with misalignment

fig 3.23	Principal stress contour plot for 3-D model with offset and misalignment
fig 5.1	Types of welded tubular joints
fig 5.2	Example of a complex node
fig 5.3	Example of a simple T-Joint
fig 6.1	Strain energy release
fig 6.2	Modes of fracture
fig 6.3	Stress state near a crack tip
fig 6.4	Mesh for 2-D plane strain model
fig 6.5	K from $\frac{1}{4}$ point nodal displacements
fig 6.6	Virtual crack extension
fig 6.7	Linesprings
fig 7.1	Edge crack in a finite width strip.
fig 7.2a	Plane strain focussed mesh.
fig 7.2b	Crack tip nodes
fig 7.3	J-Integral values at various contours
fig 7.4	Effect of change of aspect ratios on computed J-Integral
fig 7.5	Different formats used to define crack tip node clusters
fig 7.6	Effect of varying the number of DOF's at the crack front
fig 8.1	3-D focussed mesh containing straight crack
fig 8.2	Variation of element aspect ratio for fig 7.2a
fig 8.3	Comparison of theoretical, 2-D and averaged 3-D solutions
fig 8.4	Variation of results through depth of solid model
fig 9.1	FEMGEN generated crack mesh

fig 9.2	20 noded isoparametric hexahedron element
fig 9.3	SESAM transition elements
fig 9.4	Meshing of solid weld
fig 9.5	SESAM crack mesh
fig 9.6	Focussing of mesh in SESAM crack superelement
fig 9.7	Fully meshed T-Joint
fig 9.8	Fully meshed $\frac{1}{4}$ T-Joint with weld toe crack at chord saddle position
fig 9.9	Load Cases, UCL models
fig 9.10	Effect of assuming symmetry on a cracked joint
fig 9.11	Nodal clusters on a semi-elliptical crack
fig 9.12a	SESAM vs. ABAQUS cracked T-Joint axial loading
fig 9.12b	SESAM vs. ABAQUS cracked T-Joint out of plane bending
fig 9.13	Through thickness stress distribution UCL T-Joint
fig 9.14	SIF UCL Crack 1
fig 9.15	SIF UCL Crack 2
fig 9.16	SIF UCL Crack 3
fig 9.17	SESAM vs. weight function (UCL)
fig 9.18	SIF for flat plate vs. T-Joint (UCL Crack 1)
fig 9.19	SIF for flat plate vs. T-Joint (UCL Crack 2)
fig 12.1	BG experimental geometry
fig 12.2	TWI experimental geometry
fig 12.3	Typical grind repair mesh
fig 12.4	Typical grind repair stress contours
fig 12.5	Grind repair: Strain along weld toe and groove base
fig 12.6	Stress variation on groove surface
fig 12.7	Effect of varying groove radius

- fig 12.8 Effect of varying groove radius on different groove depths
- fig 12.9 Comparison of 3-D FE results with 2-D eqns
- fig 12.10 TWI groove geometry
- fig 12.11 Comparison of FE and experimental results (TWI geometry)

Acknowledgements

Support from a number of organisations for various parts of the work described in this thesis is gratefully acknowledged. These organisations include the Science and Engineering Research Council (SERC) through the Marine Technology Directorate (MTD Ltd) under grant numbers GR/C/7139.2 and GR/F/09839, The Department of Energy (Project No TA 93/22/293) and the other participants in the managed programme "Defect Assessment in Offshore Structures" ie MoD, British Gas, BP, British Steel, Britoil, Brown & Root, Conoco, Earl & Wright, Halcrow Offshore, Mobil, Shell, UKAEA and Veritec.

Thanks are also due to Drs MJ Cowling and RD Thomson for their assistance and encouragement throughout this work and to Prof BF Scott for allowing the use of Departmental facilities.

Finally, thanks are due to my wife, Patricia, for her continued support throughout duration of the work.

The thesis is wholly the work of C.W. Hodgson and has not been submitted elsewhere. All finite element analyses represent original contributions

SUMMARY

Oilfield exploration and production facilities are frequently required to operate in hostile environments, thus significantly increasing both the chances of, and damage caused by, failure of a structure. Many offshore oil installations consist of tubular sections connected by structural welds. Stress concentrations due to the joint geometry increase the possibility of fatigue cracking and it is common to find that the life of a joint is reduced by the presence of cracks. It is incumbent on the operator to carry out a repair on identified and significant cracks. The FE analysis of defective tubular joints is frequently used as a guide to the general behaviour of such joints rather than for specific analyses of real life faults.

This work undertook the FE analysis of tubular welded joints. By comparing the FE derived results with accredited results from other sources it was hoped to justify both the future use of FE techniques in solving these problems and the experimental and analytical techniques used to obtain results. The high level of agreement found between FE, theoretical and empirical solutions in this work has supported the use of FE techniques in this area. In addition, the results have contributed to the general level of knowledge concerning the behaviour of defective tubular welded joints.

Three areas are covered in this work: firstly the SCFs due to axial offset and angular misalignment in butt welded tubular joints; secondly the effect of the presence of cracks in complex nodes and thirdly, the possible application of grind repair techniques to remove crack-like defects from these nodes.

The SCFs resulting from axial offsets and angular misalignments, over the range found in typical offshore structures, were found to be acceptably low. Significant increases in SCF were found for larger offsets and misalignments. The current design guidance is adequate in this sphere but must be adhered to.

The full 3-D FE analysis of weld-toe cracks in tubular joints is the only way to allow for the effect of different weld geometries. This is particularly important for shallow cracks. For deeper cracks the weld toe

effect is less significant and quasi 2-D solutions may be used. Furthermore, for deeper cracks mode I opening ceases to dominate and FE solutions based on the virtual crack extension method become less reliable.

Although grind repair techniques provide a solution to some cases of fatigue cracking at welded joints, the assessment of the fatigue life of the repair will require the development of a new S-N curve, similar to the Dept of Energy's Class T curve for as-welded joints.

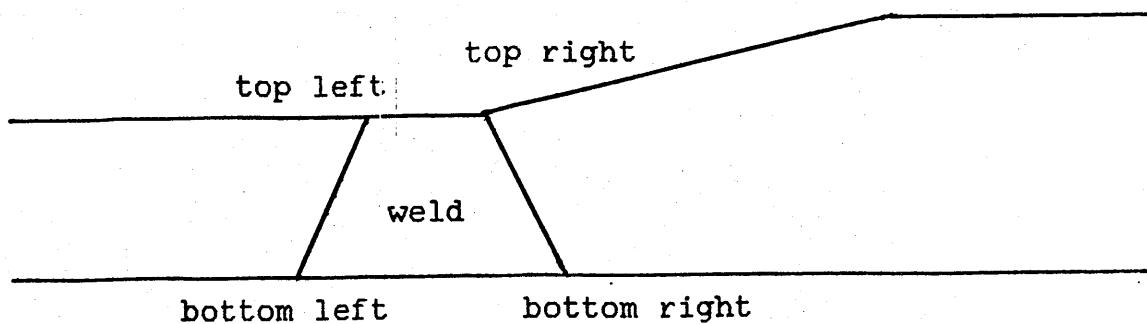
Two principal areas of concern were highlighted by this work. Firstly, FE analysis requires subjective assessments by the analyst regarding load and boundary conditions and is thus dependent on the quality, training and experience of the analyst. Secondly, it was found that, in some instances, the level of agreement between 2-D solutions and 3-D results was poor, implying that care must be taken when using 2-D solutions as a simple means of solving 3-D problems.

Notation

a	Crack depth at deepest point
c	Crack half length
e	Offset
h	Height of peaking due to misalignment
n	Index from parametric equations
r	First (Radial) polar coordinate, usually measured from crack tip
t	Material thickness
t_1	Material thickness (thinner section)
t_2	Material thickness (thicker section)
u	Nodal displacement; local X direction
v	Nodal displacement; local Y direction
w	Nodal displacement; local Z direction
DOF	Degree of Freedom
E	Young's modulus
E'	Effective Young's modulus
G	Crack driving "force"
J	J-Integral
K	Stress concentration factor (SCF) Stress intensity factor (SIF)
K_I	SIF for mode I opening
K_{II}	SIF for mode II opening
K_{III}	SIF for mode III opening
K_T	Stress concentration factor (SCF)
$K_{\text{misalignment}}$	SCF due to misalignment
K_{offset}	SCF due to offset
K_{total}	SCF due to combined offset and misalignment
L	Length of model (effective)
Y	Geometric factor for crack environment (non-dimensionalised K_T)
α	Node geometry factor: ratio of 2 x length of chord to outer diameter of chord Misalignment (degrees)

β	Node geometry factor: ratio of outer diameter of brace to outer diameter of chord
γ	Node geometry factor: ratio of outer diameter of chord to 2 x chord material thickness
θ	Second (angular) polar coordinate, usually measured from crack tip
	Position of point on chord/brace intersection (saddle = 90°)
σ	Normal stress
τ	Shear stress
	Ratio of brace material thickness to chord material thickness
ν	Poisson's ratio
trans ratio	Ratio $x_t:y_t$
thick ratio	Ratio $t_1:t_2$

Identification of weld corners



1.0 INTRODUCTION

As the needs of society continue to grow, mankind is forced to search farther and farther afield to find usable energy resources. This is particularly true of fossil fuels and especially oil. The result is that oilfield exploration and production facilities are required to operate in increasingly hostile environments, such as within the Arctic Circle and the North Sea. The problems created by these environments are twofold: firstly the chance of a catastrophic failure in equipment is significantly increased and secondly, the consequences of such a failure are greatly multiplied. To counter this twin threat facilities must be designed in such a way as to maximise their reliability and efficient maintenance and repair programmes must be developed. Both these requirements demand of the engineer an improved knowledge of the behaviour of the structures he builds and operates.

The large, complex structures, such as are found in the Offshore Oil Industry, have a viable working life typically measured in decades. In many cases the jacket consists of an intricate arrangement of tubular sections connected by structural welds. Fabrication does not always occur under ideal conditions and, as well as the effects of stress concentrations, due to the joint geometry and the possible inhomogeneity of the weld material itself it is not uncommon to find that the joint's viability is further reduced by the presence of discontinuities.

Two main types of welded joint are commonly to be found, welds are commonly used to join tubular sections end to end and to join a number of tubular sections at nodes.

It is generally expected that complex joints, such as T and K-Joints, are the most likely sites of the high local stress fields which can result in rapid crack growth in, and failure of, key components. This consideration is reflected in the construction process. Frequently, the nodes are welded in a workshop environment where weld quality and fit up alignments can be accurately controlled. This involves using short members which are then welded to full length pieces on site. The likely outcome of this process is to shift offsets, misalignments and weld defects from the welds at the nodes to the welds on the tubular members. However this latter problem is alleviated

by the fact that the butt welds joining sections end to end are relatively simple to make and should be of a fairly high standard.

Thus, for practical purposes, the most productive fields for further investigation are different at the two weld sites. For nodes, the high level of accuracy of the fit up dimensions allied with the difficulty of accurately welding imply that weld defects are the most likely source of error. Conversely, for the latter, butt welded, joints, the ease of welding coupled with the problems of accurately positioning the members, suggests that the effect of offsets and misalignment at these joints is the most fruitful line of research.

These results should enable the design engineer to avoid unnecessarily highly stressed areas and the maintenance engineer to pinpoint these areas which can then be regularly monitored to assess degradation due to operating conditions. The routine checking of joints will highlight a number of defects as they arise. Prominent among these defects will be the presence of cracks. On finding a crack, the maintenance engineer is faced with a dilemma, a number of methods exist for removing the crack (repair welding, grinding etc) yet in some circumstances these may result merely in a further weakening of the joint. A non-critical crack is best left untouched, a critical crack must be dealt with. To enable the engineer to assess the importance of a crack and the best way of dealing with it requires not only a broad based study of the effect of cracks in tubular welded joints but also an investigation of the effectiveness of the possible repair methods.

In the light of these factors, this work undertook to study the three principal areas of concern outlined above. Firstly, the presence of crack like discontinuities in the welds at nodes, secondly, the effect of offset and misalignments in butt welded tubular sections and thirdly, the effectiveness of grind repair as a method of removing discontinuities from members.

1.1 Computing Environment

An FE analysis typically consists of three separate phases, each of which is performed by a separate piece of software. During pre-processing, the FE data is generated and stored on an interface file. In the second phase, the interface file is read by the solver, which analyses the problem and writes results either directly or into another interface file to be used in the third phase, postprocessing. In the latter, the results are combined and processed into the desired output form.

In general, software vendors can supply modules to perform all three phases but it is sometimes advisable to choose modules from different sources and adapt the interface files to allow these to link into a complete package.

1.1.1 Stress Concentration in Butt Welds

All FE work was performed using the TUJAP suite of SESAM mounted on a Microvax II.

The meshes were generated using using the PREFEM preprocessor with PRESEL the superelement assembly program being used on the larger, 3-D, models.

Analyses were carried out using the TUSTRA processor with POSTFEM being used for the postprocessing.

All the 2-D models were created using 8-noded subparametric curved quadrilateral shell elements. Typically the 2-D models contain between 300 and 400 elements (3000 to 4000 degrees of freedom). CPU time for a 2-D analysis varies between 1 and 2 hours.

The 3-D models consist of 20-noded isoparametric hexahedrons. For the earlier solid models (those with no misalignment) a 30 degree arc was used as the basic superelement. This was not ideally suited for the more complex geometries and for the later cases a 180 degree arc was used. CPU time for these analyses varied from a two to three hours for the simpler cases to more

than 12 hours for the larger models.

1.1.2 Failure in Tubular Welded Joints

In this section the full facilities required were not available in a single commercially available and so trials were conducted on four mesh generators - FEMGEN from FECS Ltd, SUPERTAB from SDRC, PIGS from PAFEC and PRETUBE, part of the SESAM suite from Veritec, when this became available. The latter is a specialised mesh generator for the modelling tubular joints containing defects. As such it is a powerful tool and reduced the time to produce a mesh from several man.months to a few man.days. The availability of this tool removed a large piece of the routine data preparation ^{from the} original proposed work and allowed more attention to be diverted to the results rather than the modelling.

Both ABAQUS from HKS and TUSTRA from Veritec, were trialled for the analysis phase but the optimum configuration with which to perform the work depends not only on the capabilities of the software but also on the hardware environment. In this case, SESAM was available on a single user DEC microVAX II, configured to give 150 MByte of scratch space to cope with the large storage requirements of FE analysis, while ABAQUS was only locally available on a local DEC VAX 11/750. Unfortunately, the multi-user environment on the latter restricted both the time and space available for single runs and was thus unsuitable for the larger analyses. ABAQUS was also available on the UMRCC Cyber 205 but this facility was soon rejected due to problems in file transfer.

Of the various options, FEMGEN in conjunction with ABAQUS was chosen for the initial work, carried out on the VAX 11/750, while PRETUBE in conjunction with TUSTRA was chosen for the full 3-D joint analyses, performed on the MicroVAX.

All postprocessing was done using FEMVIEW, either in its original form on the VAX 11/750 or as POSTFEM, a rebadged version included within SESAM on the MicroVAX.

1.1.3 Grind Repair of Tubular Welded Joints

The FE work for this section used the TUJAP suite of SESAM mounted on a Microvax II.

A research version of PRETUBE containing an automatic meshing facility for grooves was released by VSS. As this was not a commercial version a number of serious bugs were found which delayed this section of work. The solution to these problems finally adopted was to model the tube using the standard version of PRETUBE, switch to the research version to define the groove and then return the model to the standard version. Even with this technique it proved impossible to mesh some geometries. The Superelement assembly program, PRESEL, was used to assemble the full model.

All analyses were carried out using the TUSTRA processor with the postprocessing being carried out using POSTFEM.

The full model consists of 20-noded isoparametric hexahedrons around the welds with eight-noded sub-parametric curved quadrilateral shells. Typical CPU time for these analyses varied ^{but} was of the order of 20 hours.

SECTION A: STRESS CONCENTRATION IN BUTT WELDS

2.0 INTRODUCTION

2.1 Background

It is not uncommon for butt welded joints in tubular steel members of complex structures to contain a number of forms of misalignment. Such misalignments often occur at butt welds where there is also a coincident change in material thickness. An experimental Joint Industry Project carried out at The Welding Institute (TWI) (ref 1) assessed the importance of two of these, namely Axial Offset and Angular Misalignment.

A series of Finite Element (FE) stress analyses was undertaken in support of The Welding Institute project (as shown in Annexe 2.1) and to extend the database of stress concentration factors for misaligned butt welded joints. The programme of analyses consists principally of a series of 2-D analyses (essentially modelling a flat plate) and a small number of full tubular 3-D models.

2.2 Definitions

Although the term misalignment is often used loosely to describe both axial offset and angular misalignment, in order to avoid confusion, the convention used throughout this thesis is that the term **Offset** denotes an Axial Offset and the term **Misalignment** denotes an Angular Misalignment. The sign convention and definitions used for these is shown in figs 2.1a, 2.1b and 2.1c. It should be noted that the offset is defined as the relative displacement of the inner edge of the tubular section and not, as in much of the literature, as the relative displacement of the centrelines. This is due to the fact that the former value can be measured directly.

The term **Global Misalignment** is used to describe a rotation of the complete model within the reference axes.

The term **Global Offset** is used to describe the magnitude of the offset

in the centre lines of the two parts of the specimen where they are gripped in the jaws of TWI test rig (fig 2.1d).

2.3 Aims

There were three principal aims to this work. Firstly, it was hoped to provide a reasonable level of theoretical corroboration for the experimental work being carried out at TWI. Secondly, the work would also provide further support or otherwise for the published empirical equations and thirdly, it would provide a data base of results for a wider range of geometries than could be analysed in the experimental programme.

2.4 TWI Experiments

The initial experiments (ref 2) carried out at TWI used curved coupons, 875 mm long, cut from a full tubular butt joint, as specimens which were subjected to axial loading. The initial tubular sections had outer diameters of 1000 mm with t_1 and t_2 (fig 2.1a) 25 and 38 mm respectively. The tubular butt joint was welded on the inside and had a transition ratio of 4:1 on the thicker side. Results were obtained from strain gauges positioned as shown in fig 2.2c. The SCF was found by extrapolating through the strain gauges at 22 and 73mm from the weld toe ($0.2/Rt$ and $0.65/Rt$ respectively).

Later work involved subjecting a full scale butt welded tubular joint to 4 point bending, the resulting strain levels being found from strain gauges positioned as shown in fig 2.2d. This model had similar dimensions to the tubular sections used to produce the coupons for the 2-D phase of the work except that the total length of the joint was increased from 875 to 6000 mm.

The experimental stress analysis results from TWI were compared with the results of the GMTC FE analyses where appropriate as shown in figs 3.1 - 3.5 and 3.15.

2.5 FE Analysis

The general structure of the work carried out differed little from the

original proposal, except in two areas.

As originally planned the main areas of work were a range of 2-D geometries (essentially flat plates) and boundary conditions followed by a limited number of 3-D geometries (see Annexe 2.1).

In addition to this, considerable effort was expended in an attempt to accurately replicate five of the detailed 2-D geometries analysed experimentally by TWI (as shown in Annexe 2.2) and the boundary conditions used in this additional study were then used for a re-analysis of the 2-D models analysed previously.

A detailed Finite Element comparison with TWI full scale tubular test specimen was also carried out. The geometric factors constraining the mesh, when combined with the limitations of the available software and hardware, made it impossible to model exactly the full tubular joint. In order to reduce the model to a solvable size, it was necessary to assume that both tubular sections were perfectly round to allow full use of replicated superelements. Even with this assumption more than 24 CPU hrs were required to carry out this analysis.

All FE analysis has been carried out using Veritas Sesam System's TUJAP package from the SESAM suite (section 1.1).

The reported results are derived from more than 500 2-D analyses requiring approximately 700 CPU hrs for the processing alone. In addition considerable time was also required for pre and post processing as well as trials of a variety of loading and boundary conditions. A further 120 CPU hrs was required for the processing of the 3-D models. Here, specifically for the experimental comparison, a considerable amount of computing time (over 200 CPU hrs) was spent attempting analyses that proved to be beyond the capabilities of the system.

2.6 Previous Work

The initial work (2-D analyses) were basically flat plate analyses. Although there has been some work carried out on the full 3-D analysis of

curved surfaces with offsets and misalignments (eg ref 3) it is less well understood than the simpler case of the flat plate.

Maddox (ref 2) provides a clear resume of the simple case of welded flat plates subject to axial loading. In this case the increase in stress found at the weld is due to the presence of bending stresses resulting from the moment caused by the line of action of the applied force not passing through the centreline of the specimens at the weld.

Thus:

$$K = \frac{\sigma_{\text{axial}} + \sigma_{\text{bending}}}{\sigma_{\text{axial}}} \quad [2.1]$$

Where σ_{axial} is the stress due to the applied load and σ_{bending} is the bending stress caused by the offset or misalignment.

2.6.1 Offset

For two plates of equal thickness ($t_1 = t_2$) with the weld situated at the centre and including an offset as shown on fig 2.3:

$$\sigma(\text{max bending}) = \frac{M y}{I} = \frac{\frac{P e}{2} \cdot \frac{t}{2}}{\frac{b t^3}{12}} \quad [2.2]$$

$$\begin{aligned} \Rightarrow \sigma(\text{max bending}) &= \frac{3 P e}{b t^2} \\ &= \frac{3 e \sigma_{\text{axial}}}{t} \end{aligned} \quad [2.3]$$

thus:

$$K = 1 + \frac{3 e}{t} \quad [2.4]$$

Similar equations can be derived showing the effect of the two plates having different lengths (ref 4).

Burdekin (ref 5) has derived an expression to take account of a change in material thickness at the weld ($t_1 \neq t_2$) of the form:

$$\frac{\sigma_{\text{bending}}}{\sigma_{\text{axial}}} = \frac{3 \left\{ \left[\frac{t_2}{t_1} \right] - 1 \right\}}{\left\{ 1 + \left[\frac{t_2}{t_1} \right]^3 \right\}} \quad [2.5]$$

Further work by Fawcett (ref 15 in ref 2) has evolved an equation for K_{offset} :

$$K_{\text{offset}} = 1 + \frac{6e}{t_1} \left[\frac{t_1^n}{t_1^n + t_2^n} \right] \quad [2.6]$$

Where the term n allows for a variety of boundary conditions.

2.6.2 Misalignment

For two plates of equal thickness ($t_1 = t_2$) with the weld situated at the centre and including a misalignment as shown on fig 2.4:

Bending Moment = Ph

$$\sigma_{\text{(max bending)}} = \frac{M y}{I} = \frac{Ph \frac{t}{2}}{\frac{bt^3}{12}} \quad [2.6]$$

$$= \sigma_{\text{axial}} \frac{6h}{t} \quad [2.7]$$

Giving:

$$K_{\text{misalignment}} = 1 + \frac{6 h}{t} \quad [2.8]$$

For small α , $\tan \alpha = \alpha$ and eqn [2.8] becomes:

$$K_{\text{misalignment}} = 1 + \frac{3 \alpha L}{2 t} \quad [2.9]$$

Similar terms exist for fixed end conditions (ref 6). Equation [2.9] takes no account of straightening of the specimen under load. Kuriyama (ref 7) has proposed a further factor to allow for this effect.

2.6.3 Offset and Misalignment

Maddox (ref 2) proposes simple superposition of the offset and misalignment equations to give:

$$K_{\text{total}} = 1 + (K_{\text{offset}} - 1) + (K_{\text{misalignment}} - 1) \quad [2.10]$$

2.6.4 Areas Requiring Investigation

Three areas of work still require further study. Firstly, the equations above do not describe the effect of the thickness transition ratio. Secondly, there is no term to allow for the effect of the thickness change in a joint subject to misalignment. Finally, the accuracy of these equations when used to predict the behaviour of a full tubular joint is not documented.

2.6.5 Format of Results

To allow for direct comparison with TWI results SCFs have been used to define the effect of an offset or misalignment. For an axial load, these may be used to derive the ratio bending stress/total stress by;

$$\frac{\sigma_{\text{bending}}}{\sigma_{\text{total}}} = \frac{K - 1}{K} \quad [2.11]$$

Programme of FE Stress Analyses (For Offset and Misaligned Butt
Welds)

2-D Analysis

Three sets of boundary conditions

Three values of L/t_1

Tension loadcase

1. Thickness transition length (aligned joints)
ratio = 1, 2, 4 and 8:1
2. Thickness ratio = 1.25, 1.5, 2.0, 2.5, 3 and 4:1
3. Offset, e/t_1 , in the range - 0.5 to + 0.6
4. Misalignment, selected values
5. Combined offset and misalignment

2-D Comparisons

See Annexe 2.2

Run for a variety of global misalignments/offsets.

Overall length = 875mm and 500mm

$t_1 = 25$ mm

$t_2 = 37.5$ mm

transition ratio = 4:1

displacement and force loading applied.

Annexe 2.1

3-D Models

Axial Tension Load

Encastre at thick end

MODEL 1 od = 1000 mm
 t₁ = 25 mm
 t₂ = 37.5 mm
 transition ratio = 4:1

MODEL 2 od = 1000 mm
 t₁ = 25 mm
 t₂ = 37.5 mm
 transition ratio = 2:1

MODEL 3 od = 1000 mm
 t₁ = 25 mm
 t₂ = 50 mm
 transition ratio = 4:1

MODEL 4 od = 1000 mm
 t₁ = 25 mm
 t₂ = 37.5 mm
 transition ratio = 4:1
 offset = 5 mm

MODEL 5 od = 1000 mm
 t₁ = 25 mm
 t₂ = 37.5 mm
 transition ratio = 4:1
 misalignment = 2 degs

MODEL 6 od = 1000 mm
 t₁ = 25 mm
 t₂ = 37.5 mm
 transition ratio = 4:1
 offset = 5 mm
 misalignment = 2 degs

MODEL 7

od = 1000 mm

t₁ = 25 mm

t₂ = 37.5 mm

transition ratio = 4:1

misalignment = 0.6 degs

MODEL 8

od = 1000 mm

t₁ = 25 mm

t₂ = 37.5 mm

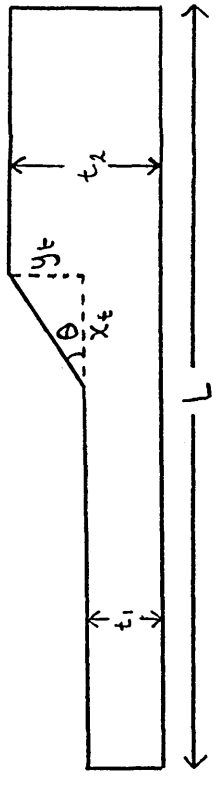
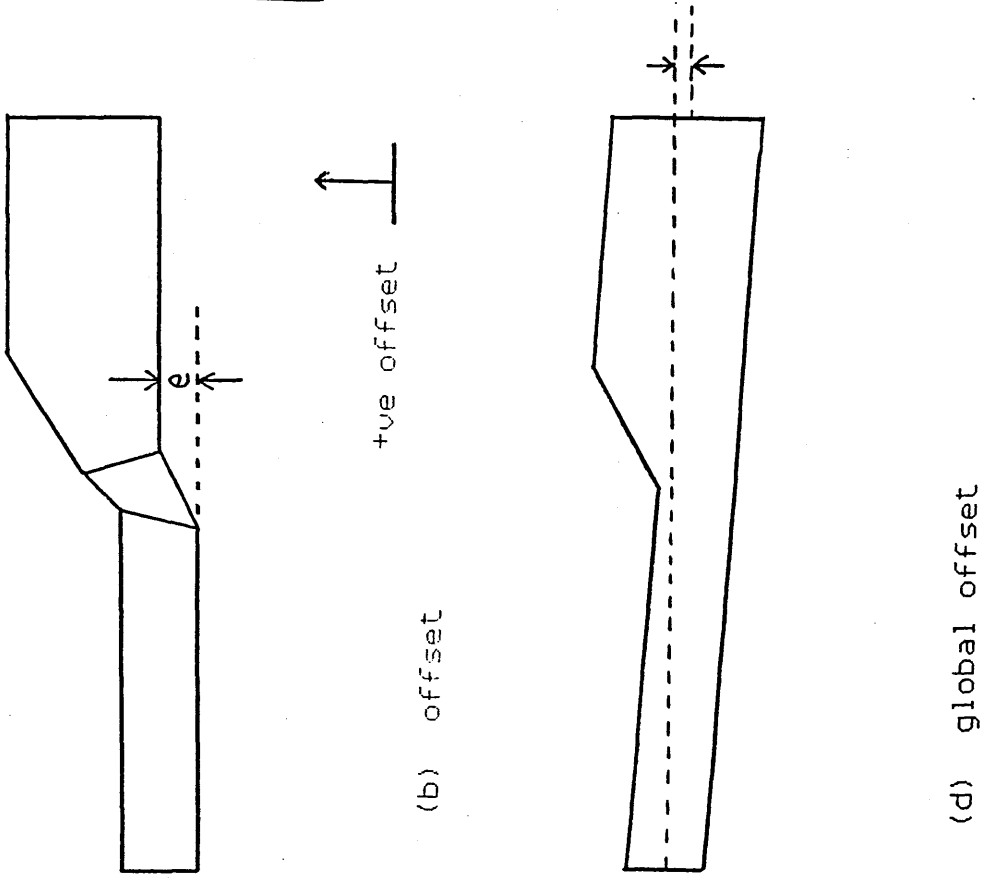
transition ratio = 4:1

offset = 5 mm

misalignment = 0.6 degs

Detailed Experimental Geometries for Comparisons

Welding Institute Specimen Identifier	Characteristics
W1-15	Misalignment = + 0.45 degrees Offset = + 4.3 mm $e/t_1 = + 0.17$
W4-25	Misalignment = + 0.50 degrees Offset = + 3.6 mm $e/t_1 = + 0.14$
W5-36	Misalignment = + 0.85 degrees Offset = - 2.8 mm $e/t_1 = - 0.11$
W9-47	Misalignment = + 1.85 degrees Offset = - 2.2 mm $e/t_1 = - 0.09$
W3-10	Misalignment = + 2.20 degrees Offset = - 3.8 mm $e/t_1 = - 0.15$



(a), t_1 , t_2 & transition ratio

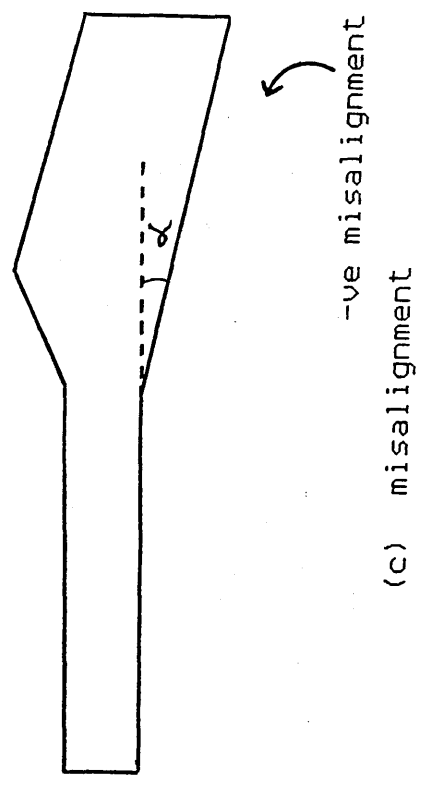
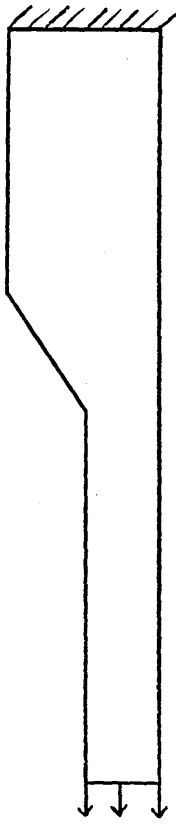
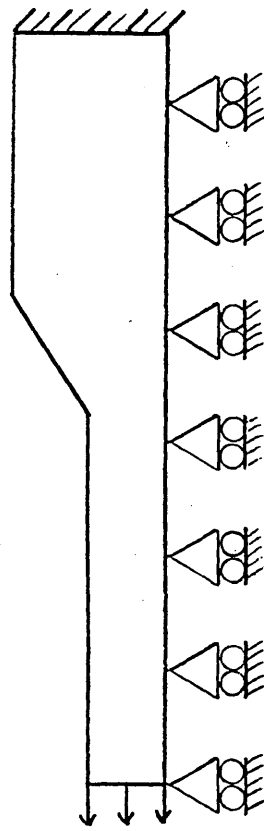


fig 2.1 Definition of t_1 , t_2 , transition ratio, offset and misalignment

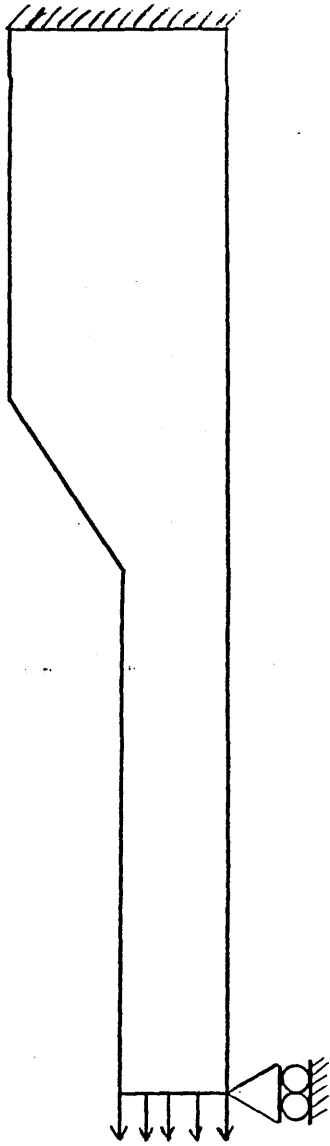


(i) BC1



(ii) BC2

fig 2.2a 2-D models boundary conditions: initial studies (BC1 & BC2)



run with force and displacement loading

fig 2.2b 2-D experimental comparisons and later study (BC3)

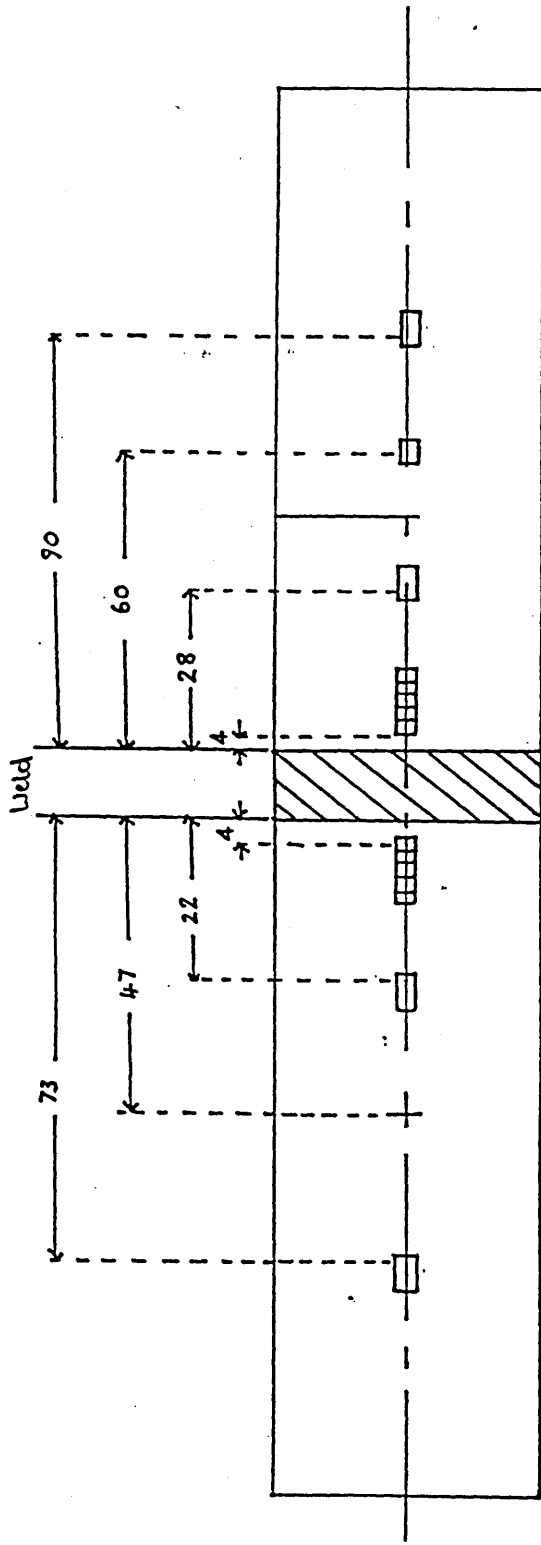


fig 2.2c 2-D --TWI experimental strain gauge positions

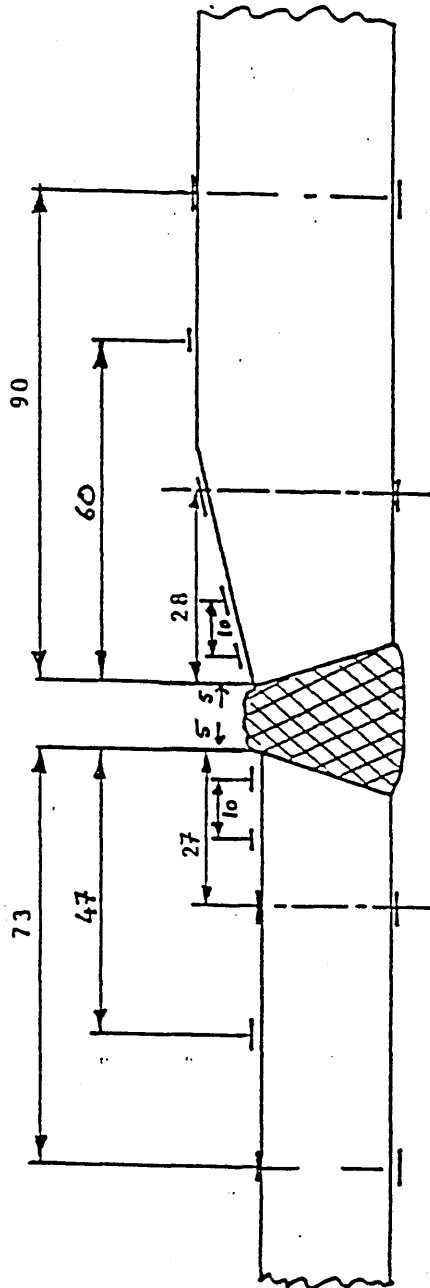


fig 2.2d 3-D - TWI experimental strain gauge positions

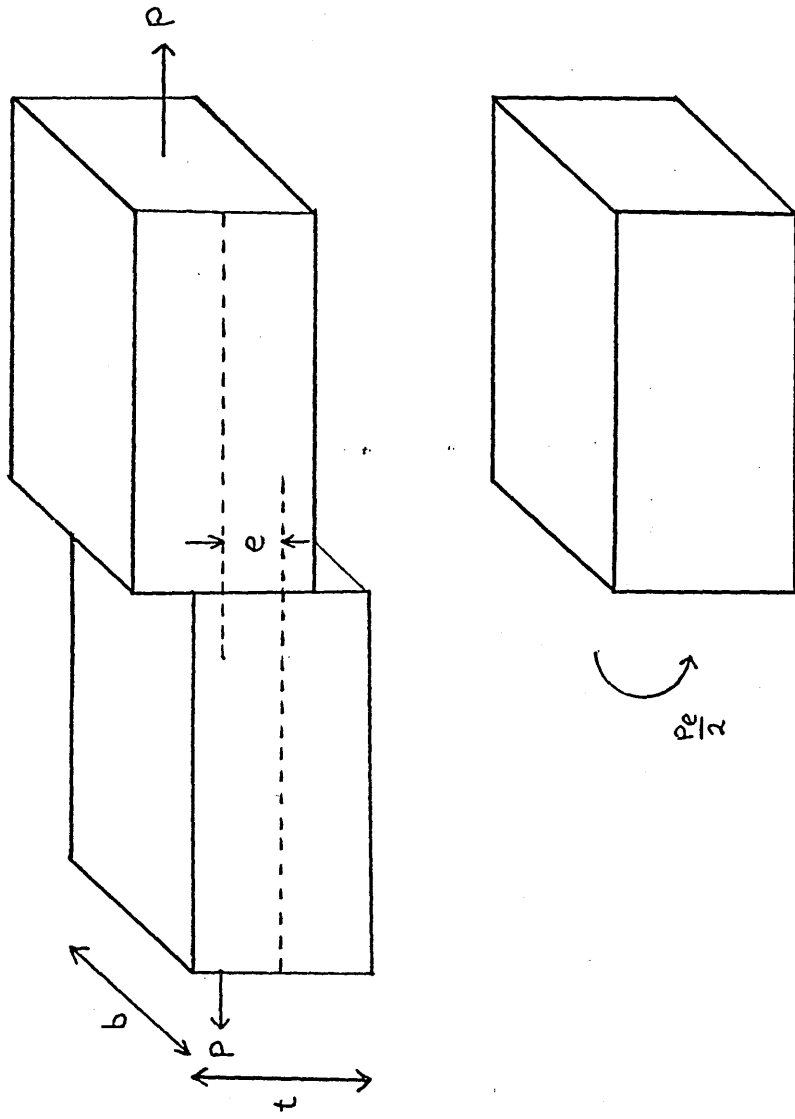


fig 2.3 Offset welded joint in a flat plate

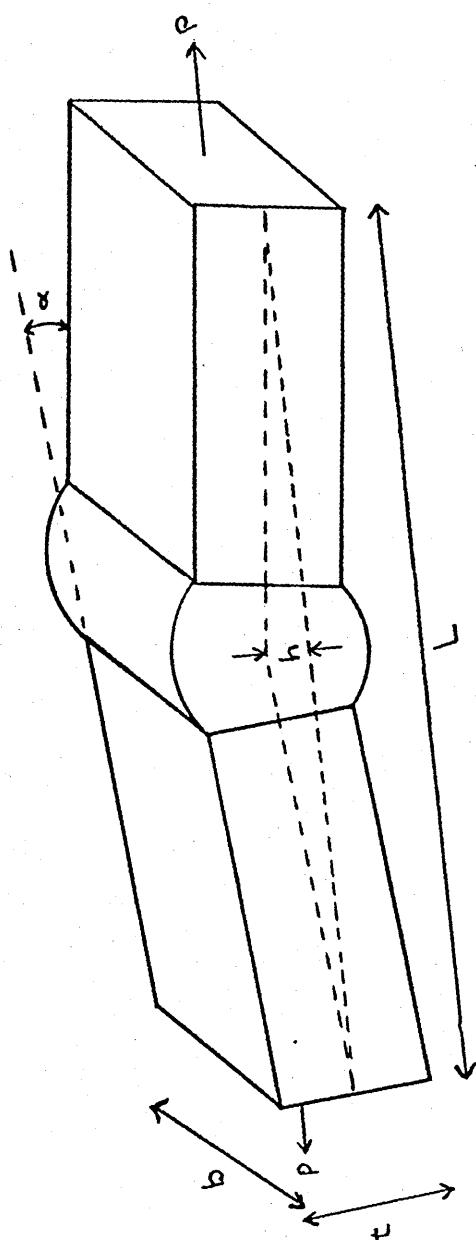


fig 2.4 Misaligned welded joint in a flat plate

3.0 RESULTS

3.1 2-D Results

3.1.1 Introduction

A wide range of 2-D models was analysed. These models consisted of eight noded quadrilateral shell elements representing a cross section of the joint. Thus, these are essentially flat plate results and must be treated with caution when extended to allow predictions regarding the behaviour of tubular joints.

The models were analysed for three sets of boundary conditions, as explained below, and the results are represented here in figs 3.1 - 3.14. No attempt was made to model the weld profile (see fig 1.1b) and no imperfections were modelled in the weld itself.

3.1.2 Comparison with TWI Experiments

Considerable difficulty was experienced initially in replicating the true boundary conditions of TWI experiments as it was not possible to determine accurately the amount of bending permitted in the test rig. The comparisons were made on the basis of the normalised maximum principal stresses along the top surface of the model, thus allowing a check to be made on the extrapolation through the experimental strain gauge positions.

Early work on 2-D models used the two extreme cases, completely free to bend and no bending permitted (figs 2.2a(i) & 2.2a(ii), BC1 & BC2). While these allowed the general trends of variation with different parameters to be assessed they did not provide an accurate comparison with the experimental results. A third set of boundary conditions, derived from an examination of the detailed experimental results, (fig 2.2d, BC3), was introduced to achieve a high level of agreement. The empirical results showed that in some cases the sign of the stress along the surface of a specimen changed, implying that there existed a point of inflexion in the test coupon. These models were analysed with two load cases, a displacement load and a force load. Even then a number of problems were encountered. Figs 3.1 - 3.5 show the principal stresses at the surface nodes near the weld and the results obtained at the

strain gauge positions in the experimental work. It was found that, when using the actual coupon length, $L = 875$ mm, boundary condition BC3 gave a reasonable level of agreement for models with small misalignments and positive offsets (figs 3.2 & 3.4). However, for larger misalignments and negative offsets (figs 3.1, 3.3 & 3.5) a less good correlation was found.

The Stress Concentration Factor (SCF) had been determined, in the experimental case, by extrapolating through the strain gauge positions at 22 and 73 mm from the weld toe and in the FE case by extrapolating along the linear section of the results. It was further noticed that as the agreement between the FE analysis and experiment deteriorated the FE force loading results fell away faster than the results for the displacement loading, although the extrapolated values were still reasonably close to each other.

Later information from The Welding Institute suggested that, although the coupons used in the experiment have a total length of around 875 mm, once the proportion of the length held in the grips of the rig is discounted, the effective length of each specimen is probably of the order of 500 mm. The specimens were therefore re-modelled with a length of 500 mm and the analyses repeated (figs 3.1 - 3.5). This change resulted in a significant improvement in the agreement between the experimental and FE results in the cases where agreement had originally been poor (ie cases with large misalignments and negative offsets figs 3.1, 3.3 & 3.5). These results tend to imply that, especially for models with a negative offset and large misalignment, the overall length of the specimen is important. Unfortunately, with the experimental geometries used for these analyses, it was not possible to observe a pattern which would allow one single factor (e.g. offset or misalignment) to be identified as the parameter most influenced by the length of the model, as the models with the "most negative" offset also have the largest misalignments (see Annexe 3.1).

Both the published empirical equations for SCFs (see section 3.1.4 below and refs 2 & 8) and the results expected from a simple examination of the moments at the weld predict that the overall length of the specimen is not a significant factor in predicting the effect of an offset but is significant in the case of a misalignment. This prediction was initially confirmed by carrying out a series of analyses for different offsets and overall lengths to ascertain whether length was a relevant factor or not. This was found, at first glance,

to have no appreciable effect on the value of the results obtained (fig 3.6a). However, for large negative offsets, the difference between SCF results for $L/t = 20$ and $L/t = 30$, while being only 0.08 is 100%. To finally ensure that only the effect of the misalignment is influenced by the length, one of the samples, W3-10, was remodelled for both experimental lengths (875 mm & 500 mm) with the opposite sign for the offset. The equations predict that, as the misalignment is the same in both cases the change in value of the SCF (K) for different lengths should be the same in both cases. Fig 3.6b show this to be correct as the difference in SCF's is the same in both cases.

There was no detailed information available regarding the global misalignment of the model within the experimental test rig and the analyses were carried out with a variety of global rotations up to and including the magnitude of the misalignment. This was found to have little effect on the results obtained.

While it is not possible to identify the parameter, or group of parameters, which are responsible for the remaining variation in the accuracy of the results a number of possibilities do exist. Firstly, the assumption that the effective length is 500mm may not be totally accurate since the effective constraint applied in the experiments is unknown and, as has been shown, the results are not insensitive to length. Secondly, the global misalignment of the specimen in the experiments may be considerably more than two degrees (the largest global misalignment analysed using Finite Elements) and may, therefore, have a more significant effect than the early results tended to suggest. In addition other experimental factors, such as the accuracy of the end grinding, location in the jaws etc. may have all acted to distort the specimen in an experiment, yet none of these factors have been introduced into the FE model. It is also likely that the Global Offset has some effect on the amount of bending in the model as will the detailed geometry of the weld profile.

3.1.3 FE Stress Analyses

The results obtained from the boundary conditions BC1 and BC2 do not lend themselves to the form of extrapolation used in the comparisons with the experimental results, as can be seen in fig 3.7. For both these sets of boundary conditions the increase in stress at the weld toe is very highly localised and there is no gradual, linear, increase to allow extrapolation to the

weld toe as happens with the third set of boundary conditions BC3. This inability to extrapolate was further complicated by the presence of a slight drop in stress immediately preceding the sharp rise at the weld toe. This dip frequently corresponds to the location of a strain gauge in the experiments. This dip is also noticed in the models which have boundary conditions BC3, but here its effect is less critical in this case as there is a clearly discernible linear section which can be extrapolated to the weld toe position.

Due to this problem in extrapolating, in analysing the results the postprocessor POSTFEM was used to calculate the stresses at the weld toe node. POSTFEM achieves this by extrapolating through the different Gauss Points to the node and averaging these results. This produces a result that is dramatically higher than that achieved with the extrapolation used in the experimental comparisons if the stress concentration is increasing and significantly lower if the stress concentration is decreasing. Despite these problems the results obtained enable the sensitivity of the results to varying parameters to be assessed. These results are shown in figs 3.8 - 3.11, in all cases these results are given for all three boundary conditions and the extrapolated values are given for BC3.

A later series of FE models was generated as shown in Annexe 3.2. The effects of the misalignment and overall length were related. As the overall length tends to zero the increase in SCF due to the misalignment will also tend to zero since the moment due to the displacement from the centreline caused by the misalignment decreases linearly with length. This effect can be clearly seen in fig 3.6c.

Further study may be required to assess the effect of a thickness ratio especially with a negative misalignment as there is a clear deviation from the pattern for these results.

Following a study of the results obtained from the 2-D analysis it has been noted that:

- i. The ratio L/t is not critical for values between 25 and 100 for cases of thickness change with no offset or misalignment (results from section 3.1 further show that, as predicted by the parametric equations, the length is not significant in most cases where an offset only exists).

ii. Varying the thickness ratio has some effect on the SCF but it is small compared to that of the transition ratio (figs 3.8 & 3.9), although this situation is reversed where the extrapolated values from BC3 are used since the transition ratio is essentially a local weld toe parameter. The effect of both the thickness and transition ratios can be clearly seen in fig 3.9e.

iii. For negative offsets the maximum stress occurs at the top right hand corner of a weld i.e. on the thick side of the weld, as shown in fig 2.1b, while for positive offsets it occurs at the top left hand corner (thin side). In this latter case, as the maximum stress occurs at a location remote from the transition toe, the effect of the transition ratio is considerably less than for negative offsets (fig 3.10).

iv. At negative misalignments the angle reduced at the weld by the misalignment is $\theta - \alpha$ the angle at the transition toe. Thus the effects of two angles interact strongly and the transition ratio is again a relatively important factor. For positive misalignments the sharper angle produced by the misalignment is on the opposite side to the transition toe and hence the effect of varying the transition ratio is negligible (fig 3.11).

3.1.4 Comparison with Parametric Equations

The Progress report published by The Welding Institute in Sept 1987 (ref 2) contains a section comparing the experimental SCF results with parametric formulae published by Maddox (ref 8). For cases of combined offset and misalignment the theoretical effects of the offset and misalignment are estimated separately and combined using a third formula to find the combined effect. Care is required here as the offset used in these equations is defined in terms of the centrelines of the coupons and not the bottom surface as in this work. To allow this comparison to be carried out two sets of models in the current programme were studied using boundary conditions defined as BC3 (fig 2.2d). The first set of models contained various offsets but no misalignments and the second set contained misalignments but no offsets. These were run for both force and displacement load cases. All FE results quoted in this section were obtained by extrapolating to the top left of the weld as defined in fig 2.2d, i.e. the weld toe at the thin side of the joint on the inside surface of the

tubular member.

Specifically it is suggested (ref 2) that for an Offset:

$$K_{\text{offset}} = 1 + \frac{6e}{t_1} \left[\frac{t_1^n}{t_1^n + t_2^n} \right] \quad [3.1]$$

Where e is the distance between the centrelines of the two sections and $n = 3$ or 1.5. It was stated in ref 8 that $n = 1.5$ is the more appropriate figure, however the FE results obtained here suggest that a value of $n = \text{approx } 1.0$ may be even more appropriate (see fig 3.12), although for the range of experimental offsets analysed the difference in K between $n = 1.5$ and $n = 1.0$ is less than 3%.

The formula (ref 8) used to calculate the effect of a misalignment was:

$$K_{\text{misalignment}} = 1 + \frac{3}{4} \alpha \frac{L}{t} \left[\frac{\tanh(\beta/2)}{\beta/2} \right] \quad [3.2]$$

$$\text{Where } \beta = \frac{L \sqrt{3\sigma}}{t E}$$

and Eqns [3.1] & [3.2] are combined using:

$$K_{\text{total}} = 1 + (K - 1)_{\text{offset}} + (K - 1)_{\text{misalignment}} \quad [3.3]$$

Eqn [3.2] is a considerable simplification of the true situation as this equation takes no account of the different thicknesses of the two parts of the model. Fig 3.13 shows a comparison of the FE results with the results obtained from eqns [3.1] & [3.2] as stated above with the tanh correction being used.

The difference in SCF, within the range of misalignments found in the specimens (typically 0 - 2 degs) between the FE and theoretical results varies from 0 - 25%. On the basis of these results it is proposed, as a consequence of the current study, that the assumptions made in order to allow eqn [3.2] to be used are valid only within the range of results being studied here but are not acceptable for a wider range of misalignments.

It was found, in the current study, (Annexe 3.3 shows results for $n = 1.0, 1.5$ & 3.0) that the values obtained by combining the results of the two geometries agree reasonably well with the results obtained from a model with combined offset and misalignment, within the range of geometries used in the experimental study. However, even at the limit of these values (eg W3-10) the difference between FE and theoretical results can be as much as 25% (fig 3.14). Also from fig 3.14 it can be seen that, with the results currently available, there is no clear pattern connecting the accuracy of the comparison between the results obtained by FE analysis and Eqn [3.1] to the magnitude of the offset. Conversely there does appear to be a significant degeneration in the agreement as the magnitude of the misalignment, Eqn [3.2] increases. It should be noted that the use of combined offset and misalignment is not an example of combining two load cases on the one model but a combination of two models with the one load case. Hence simple superposition as suggested previously (ref 2) is not necessarily valid.

Thus the FE work tends to suggest that the equations give a reasonably accurate description of the situation being modelled but are limited in their use to geometries similar to those in the experimental programme.

3.2 3-D Results

3.2.1 Introduction

A limited range of 3-D models was analysed. As the number of elements required to allow for the addition of the third dimension is considerable, a much coarser mesh was used compared to the 2-D models. As in the 2-D models, the weld profile was not modelled and the full joint was considered to consist of a homogeneous material.

3.2.2 Comparison with TWI Experiments

As mentioned in section 2.4 above, the work involved in accurately modelling the full scale test specimen of the Welding Institute experiment was by no means trivial. A number of complicating factors had to be addressed. Firstly, solid elements, rather than shells, were required to allow the detailed area of the weld to be accurately modelled. As the maximum depth of these elements is dictated by the thickness of the material an inordinately large

number of elements were required if the aspect ratio was to be kept within reasonable limits. Even when restricting the model to a single element through the thickness this produced an impractically complex mesh. As the maximum length of one side of the solid element is dictated by the material thickness the maximum element size is tiny compared to the total length of the model (e.g. if the aspect ratio of elements is restricted to 2:1 then over 7500 elements (200000 degrees of freedom) are required to define the mesh). The resulting analysis was, however, considerably beyond the capabilities of the available computing system. In order to reduce the size of the analysis the welded joint was remodelled using solid elements for the centre third of the tube and shell elements for the two end thirds, the shell solid interface being modelled using transition elements. As the thickness of a shell element does not affect its aspect ratio this allowed the degree of refinement of the mesh to be dramatically reduced at the ends, further reducing the size of the analysis.

The loading was modelled as an applied force at the ends of the tube with the actuator saddles being fixed against displacement in the direction of the loading. This is a reversal of the experimental situation but is easier to model. No detailed information was available regarding the degree of flattening occurring at the ends of the tubes and as a reasonable compromise the force was assumed to be applied over a 120° arc on the thin side and a 60° arc on the thick side, the applied force being highest at the top centreline of the tube.

A comparison of the FE and experimental results was made for total loads of 400 and 2800kN (figs 3.15a & 3.15b) since the strain gauge results appear to be slightly nonlinear.

The FE results were found to give consistently higher strains than the experiment. The results found on the thick side of the joint have significantly higher level of agreement than on the thin side. In the light of the comments made above regarding the amount of distortion occurring in the model it is felt to be likely that this difference between the results is, to some extent, due to the experiment and the model being allowed to distort differently. This would have a greater effect on the thin side where a markedly greater amount of distortion would be expected.

3.2.3 FE Stress Analyses

The analysis of a full 3-D model eliminates the problems, encountered in the 2-D analyses, in trying to establish a realistic set of boundary conditions to control the degree of bending allowed in the model. It is likely, however, that the 2-D boundary conditions, especially BC3, which allows least bending, will bear closest comparison with the results obtained from a full 3-D analysis.

Due to the finite size of the computing facilities available for this project a fairly coarse mesh had to be used for the 3-D analysis. A recent upgrading (Apr 1988) of these facilities allowed the mesh to be refined considerably and Model 1 was reanalysed with eight times the original number of elements. As can be seen from figures 3.16a & 3.16b this had no appreciable effect on the results.

3.3 2-D / 3-D Comparisons

It is outside the scope of the present work to provide conclusions regarding offsets and misalignments in full 3-D Tubular Joints as the size of the data base is small. However, this work does allow the general trends predicted by the 2-D analysis to be cross checked. Each 3-D model contains a wide range of offsets, misalignments and local bending conditions, of which only the two cross-sections in the plane of the offset and misalignment are liable to equate at all with the 2-D cases as the rest of the model is subject to more complex bending conditions.

A number of comparisons have been investigated between the 2-D and 3-D results (see Annexe 3.4) and no pattern has as yet emerged linking the 2-D and 3-D results. Figures 3.16 - 3.19 show the stress distribution along the inside surface of the 3-D models and the extrapolation through the points used in the Welding Institute's full experiment.

Despite this apparent lack of agreement the coarser analysis used in the block fill contour plots of stress (figs 3.20 - 3.23) do show similar patterns to the 2-D results. Particularly striking is the effect noted in fig 3.21 where the maximum stress can be clearly seen to cross from one side of the weld to another as the sign of the offset changes, paralleling the effect seen earlier in figs 3.10a, 3.10b & 3.10c.

Experimental Comparisons of SCF's (K)

See figs 3.2 - 3.5

$L/t_1 = 20$

SPECIMEN	OFFSET (mm)	MISALIGNMENT (degs)	SCF' s	
			SESAM	EXP
W1-15	0.17	0.45	1.85	1.74
W4-25	0.14	0.50	1.76	1.62
W5-36	-0.11	0.85	1.05	0.93
W9-47	-0.09	1.85	0.95	0.94
W3-10	-0.15	2.20	0.67	0.71

Annexe 3.1

Length and Thickness Ratio Effect on 2-D Models

A series of FE models was generated. The dimensions used in this sub-study are:

Offset	0.0
Misalignment	$\pm 2.0^\circ$
Transition ratio	4:1
Thickness ratio	1:1.25, 1.50, 2.00
L/t ₁	1:10, 25, 40, 55, 70, 85

The results of this sub-study are presented in fig 3.6c. The SCFs due to the Offset alone (from earlier results in section 3.1.3 were predicted to be:

Thickness Ratio 1:1.25, SCF = 1.35
Thickness Ratio 1:1.50, SCF = 1.59
Thickness Ratio 1:2.00, SCF = 1.78

Extrapolating from fig 3.6c gives the following results:

Thickness Ratio 1:1.25, SCF = 1.33
Thickness Ratio 1:1.50, SCF = 1.56
Thickness Ratio 1:2.00, SCF = 1.63

The equations derived from fig 3.6c relating to the effect of length for the six cases analysed are :

Misalignment = 2.00° , Thickness Ratio 1:1.25, SCF = $1+0.026(L/t)$
Misalignment = 2.00° , Thickness Ratio 1:1.50, SCF = $1+0.026(L/t)$
Misalignment = 2.00° , Thickness Ratio 1:2.00, SCF = $1+0.030(L/t)$
Misalignment = -2.00° , Thickness Ratio 1:1.25, SCF = $1-0.028(L/t)$
Misalignment = -2.00° , Thickness Ratio 1:1.50, SCF = $1-0.024(L/t)$
Misalignment = -2.00° , Thickness Ratio 1:2.00, SCF = $1-0.013(L/t)$

Annexe 3.2

These can be compared with the published formula (eqn [3.2]) which takes no account of the thickness ratio and predicts (neglecting the tanh correction) that:

$$\text{Misalignment} = 2.00^\circ, \text{ SCF} = 1+0.026(L/t)$$

$$\text{Misalignment} = -2.00^\circ, \text{ SCF} = 1-0.026(L/t)$$

Thus the initial study implies that the agreement of the FE analyses with the published formula for a positive misalignment is reasonably accurate but less so for the case of a negative misalignment.

Theoretical Comparisons of SCF's (K)

The calculated values were found using Eqns 3.1, 3.2 & 3.3. For Eqn 3.1, $n = 1.0, 1.5$ and 3.0 were used. Eqn 3.2 uses the tanh correction.

The misalignment values have no offset in terms of the definition shown in fig 2.1b which corresponds to an offset of 0.25 as defined in ref 2.

The FE offset and misalignment results were found by interpolation from figs 3.12 & 3.13. The FE combined results were found by extrapolation from figs 3.1 - 3.5. The force loading results for $L/t = 35$ were used.

$n = 1.0$

SPECIMEN	OFFSET		MISALIGNMENT		COMBINATION	
	only SESAM	Eqn 1	only SESAM	Eqns	SESAM	Eqns
W1-15	2.02	2.00	1.46	1.42	1.90	1.82
W4-25	1.94	1.94	1.44	1.40	1.80	1.74
W5-36	1.28	1.34	1.34	1.26	1.04	1.00
W9-47	1.34	1.38	1.02	0.86	0.78	0.64
W3-10	1.14	1.24	0.92	0.72	0.48	0.36

Annexe 3.3

n = 1.5

SPECIMEN	OFFSET only		MISALIGNMENT only		COMBINATION	
	SESAM	Eqn 1	SESAM	Eqns	SESAM	Eqns
W1-15	2.02	1.89	1.46	1.34	1.90	1.71
W4-25	1.94	1.83	1.44	1.32	1.80	1.63
W5-36	1.28	1.29	1.34	1.16	1.04	0.95
W9-47	1.34	1.34	1.02	0.78	0.78	0.60
W3-10	1.14	1.21	0.92	0.64	0.48	0.33

n = 3.0

SPECIMEN	OFFSET only		MISALIGNMENT only		COMBINATION	
	SESAM	Eqn 1	SESAM	Eqns	SESAM	Eqns
W1-15	2.02	1.58	1.46	1.16	1.90	1.40
W4-25	1.94	1.54	1.44	1.14	1.80	1.34
W5-36	1.28	1.19	1.34	1.00	1.04	0.85
W9-47	1.34	1.22	1.02	0.60	0.78	0.48
W3-10	1.14	1.14	0.92	0.46	0.48	0.26

2-D & 3-D Comparisons of SCF's (K)

L/t₁ = 25
 t₁/t₂ = 1.5
 trans ratio = 4:1

Extrapolated 3-D results use 0.2 √Rt and 0.65 √Rt
 3-D models have axial loading
 Eqns results calculated using n = 1.0, 1.5 & 3.0

K for force loading (n = 1.0)

OFFSET (mm)	MISAL'T (degs)	3-D SCF's			BC	2-D SCF's		
		POSTFEM	EXT'P'D			POSTFEM	EXT'P'D	EQNS
0.0	0.0	1.34	1.40	1	1.75			
				2	2.05			
				3	2.82	1.59	1.60	
-5.0	0.0	0.95	0.91	1	0.007			
				2	0.002			
				3	0.007	0.45	1.12	
5.0	0.0	1.80	1.77	1	1.88			
				2	4.62			
				3	6.44	2.10	2.08	
0.0	-2.0	1.45	1.41	1	6.88			
				2	2.26			
				3	4.18	2.20	2.41	
0.0	2.0	1.39	1.30	1	-0.05			
				2	1.86			
				3	1.76	1.05	0.79	

Annexe 3.4

K for force loading (n = 1.5)

OFFSET (mm)	MISAL'T (degs)	3-D SCF's		BC	2-D SCF's		EQNS
		POSTFEM	EXT'P'D		POSTFEM	EXT'P'D	
0.0	0.0	1.34	1.40	1	1.75		
				2	2.05		
				3	2.82	1.59	1.60
-5.0	0.0	0.95	0.91	1	0.007		
				2	0.002		
				3	0.007	0.45	1.10
5.0	0.0	1.80	1.77	1	1.88		
				2	4.62		
				3	6.44	2.10	1.95
0.0	-2.0	1.45	1.41	1	6.88		
				2	2.26		
				3	4.18	2.20	2.41
0.0	2.0	1.39	1.30	1	-0.05		
				2	1.86		
				3	1.76	1.05	0.79

K for force loading (n = 3.0)

OFFSET (mm)	MISAL'T (degs)	3-D SCF's		BC	2-D SCF's		EQNS
		POSTFEM	EXT'P'D		POSTFEM	EXT'P'D	
0.0	0.0	1.34	1.40	1	1.75		
				2	2.05		
				3	2.82	1.59	1.60
-5.0	0.0	0.95	0.91	1	0.007		
				2	0.002		
				3	0.007	0.45	1.07
5.0	0.0	1.80	1.77	1	1.88		
				2	4.62		
				3	6.44	2.10	1.62
0.0	-2.0	1.45	1.41	1	6.88		
				2	2.26		
				3	4.18	2.20	2.41
0.0	2.0	1.39	1.30	1	-0.05		
				2	1.86		
				3	1.76	1.05	0.79

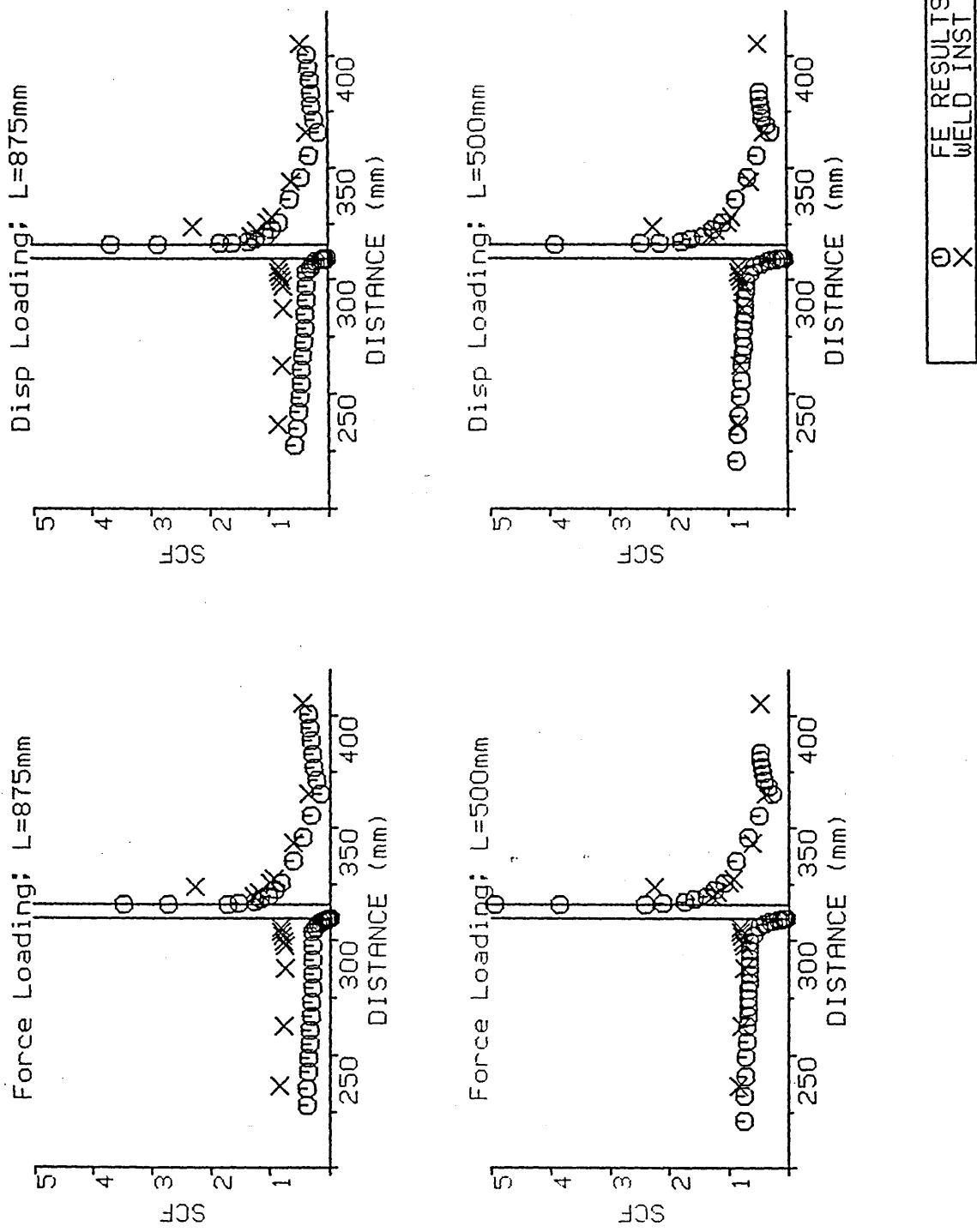


fig 3.1 Comparison of FE results with w3-10

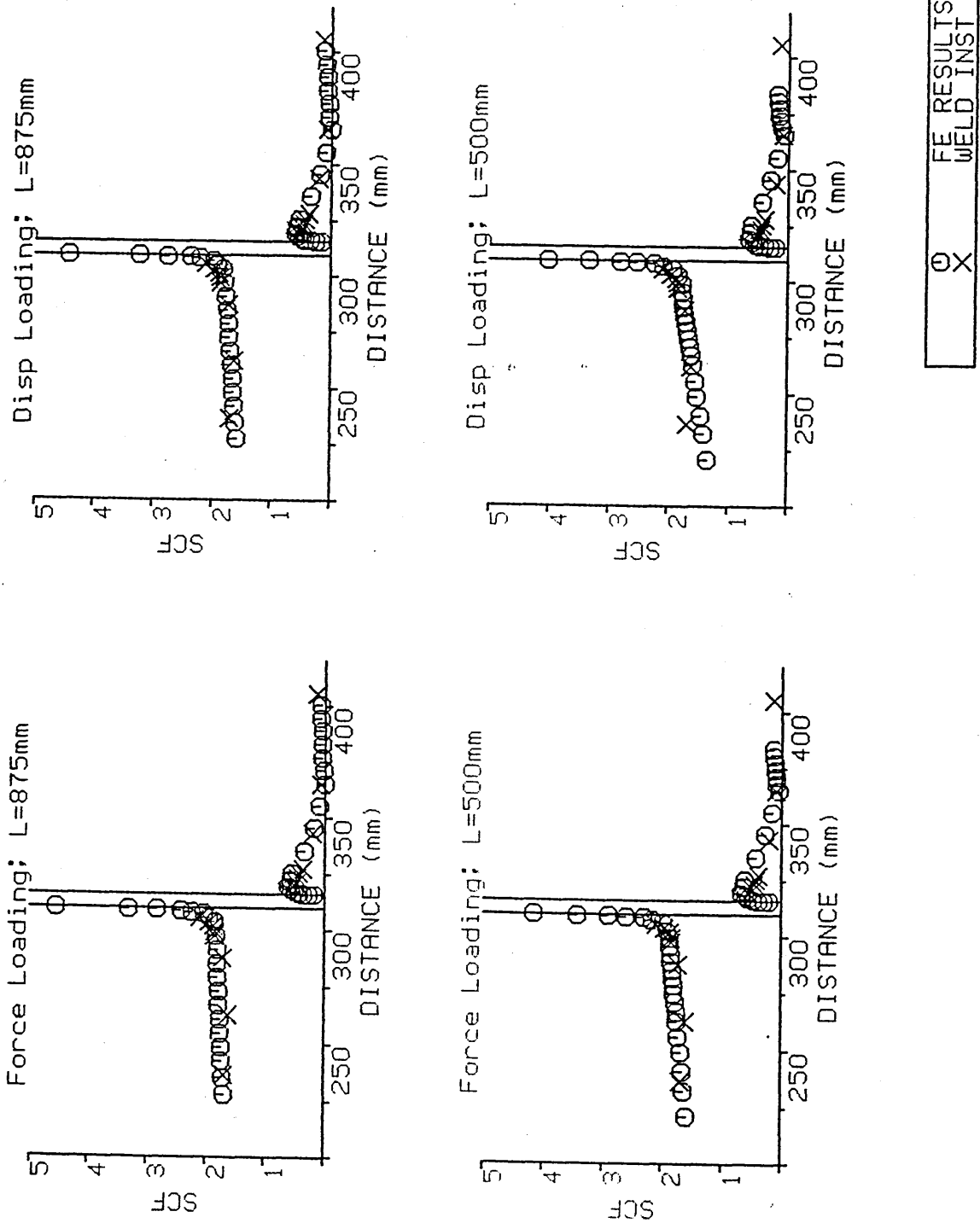


fig 3.2 Comparison of FE results with W1-15

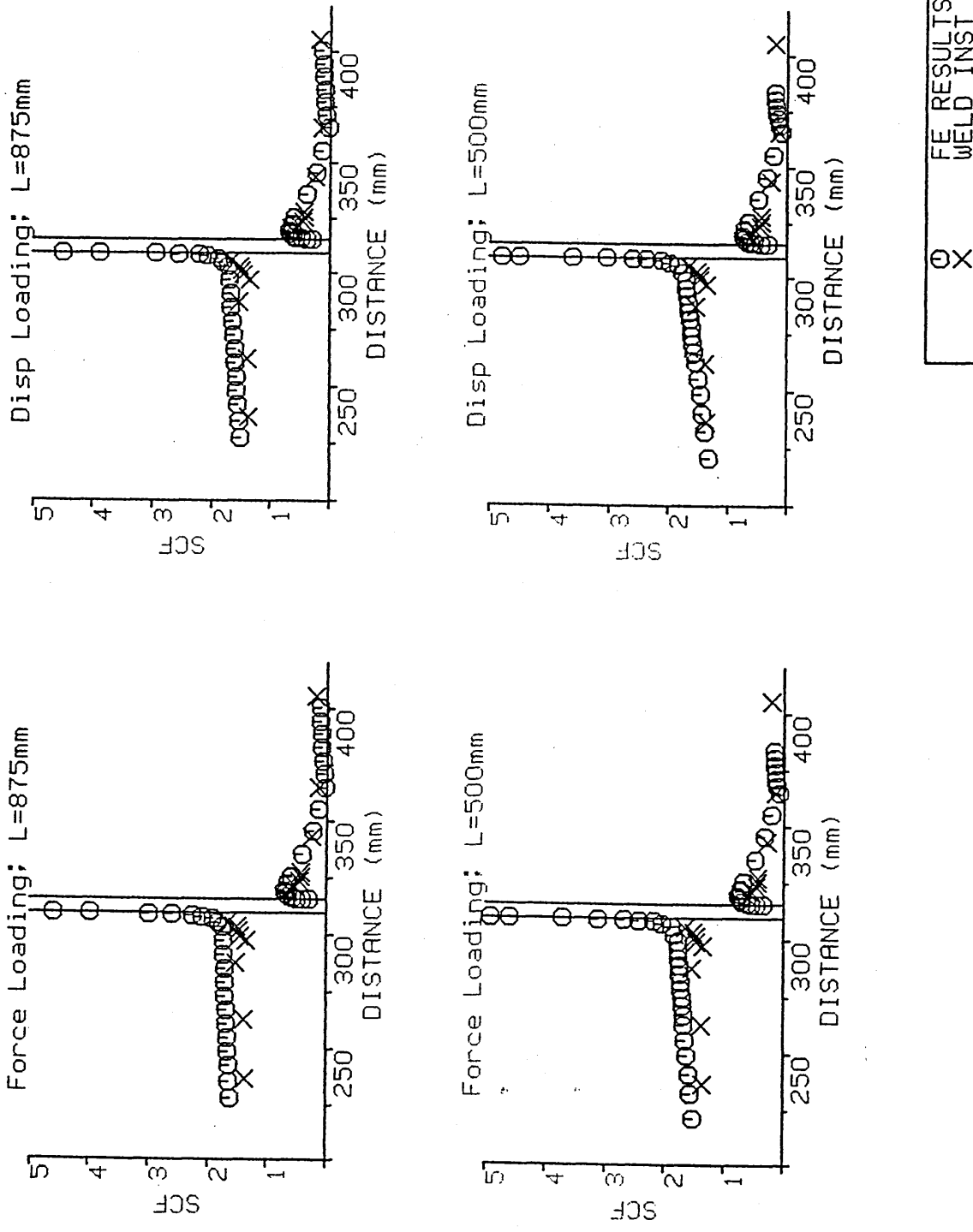


fig 3.3 Comparison of FE results with W4-25

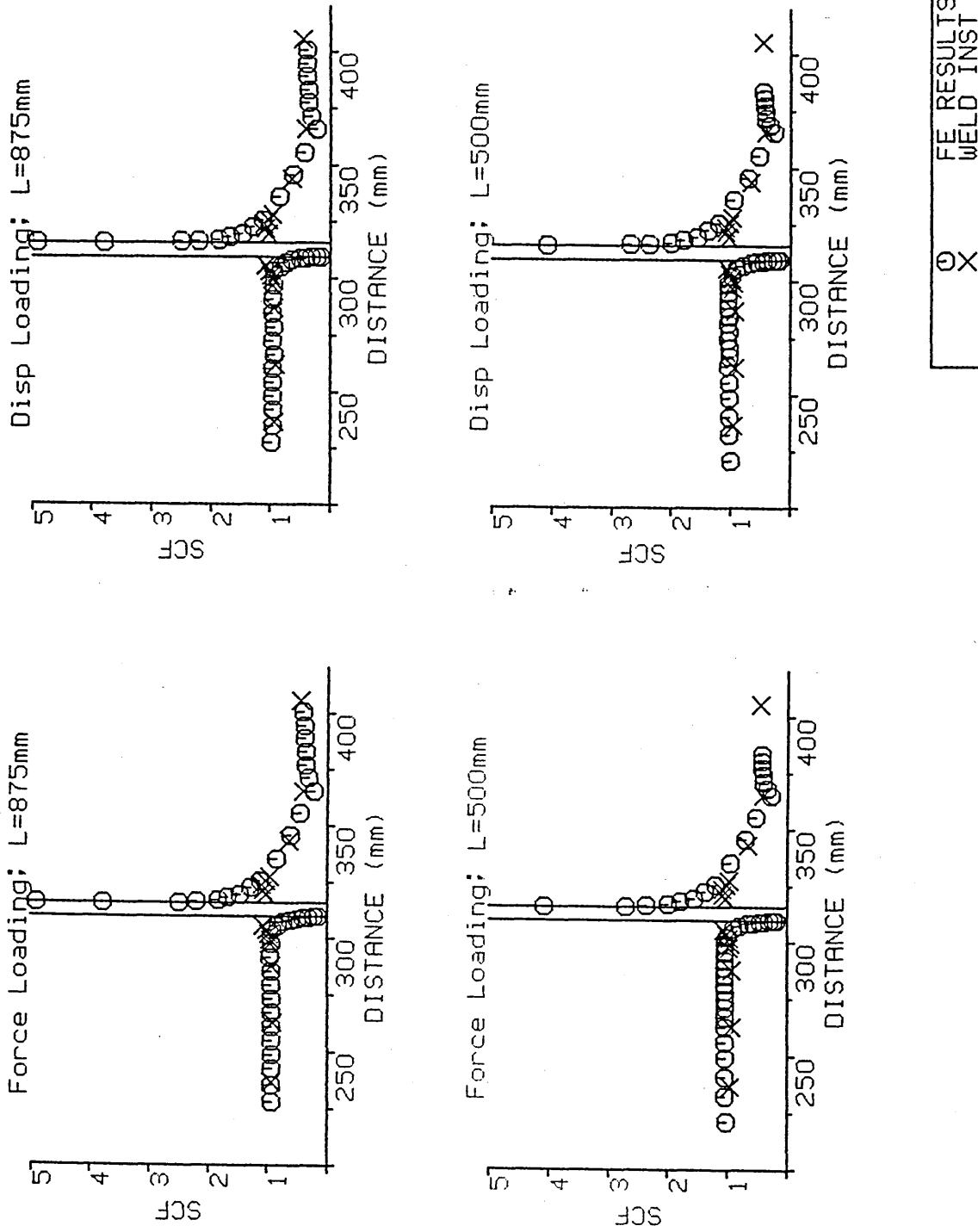


fig 3.4 Comparison of FE results with W5-36

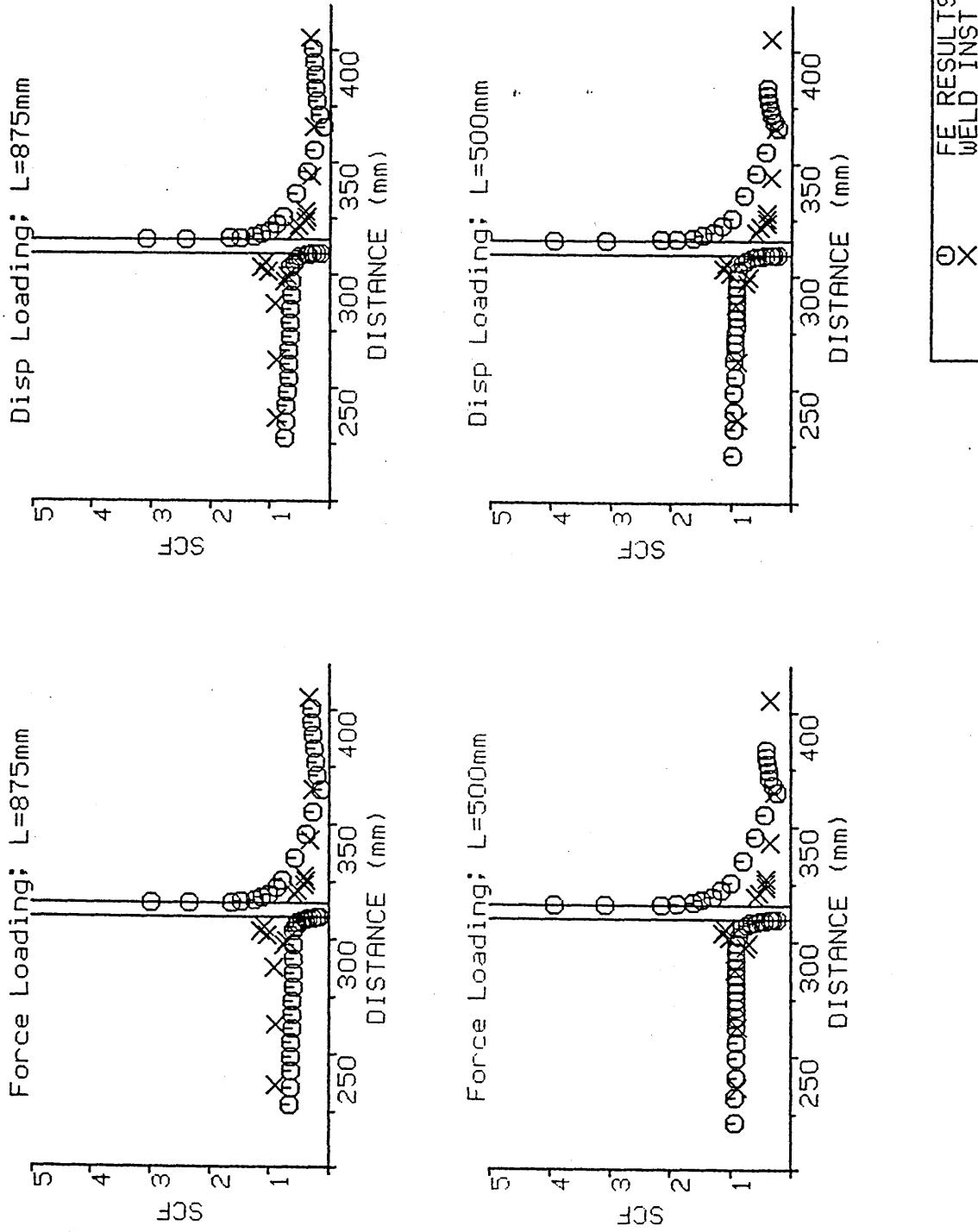


fig 3.5 Comparison of FE results with W9-47

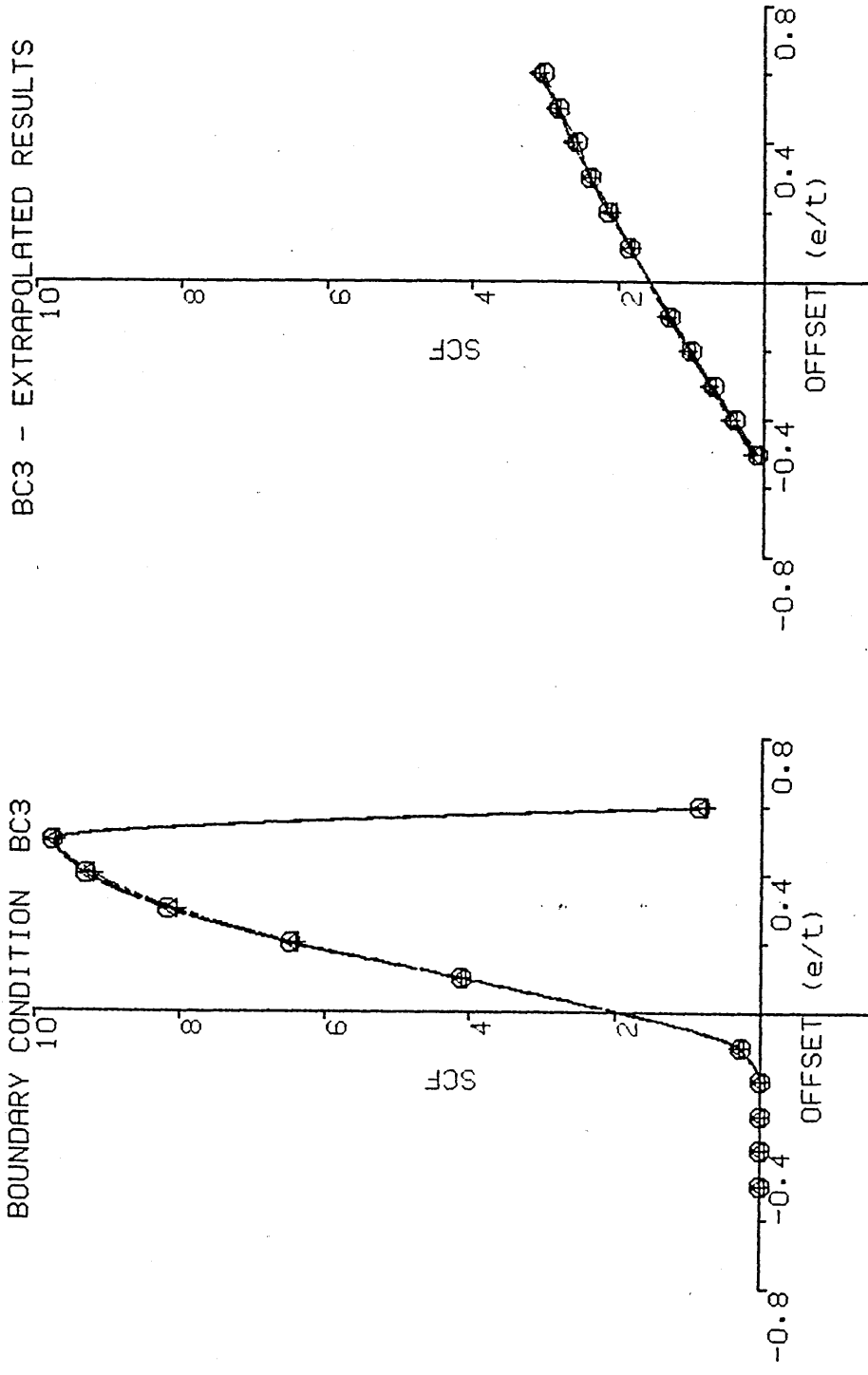


Fig 3.6a Effect of varying length on offset results

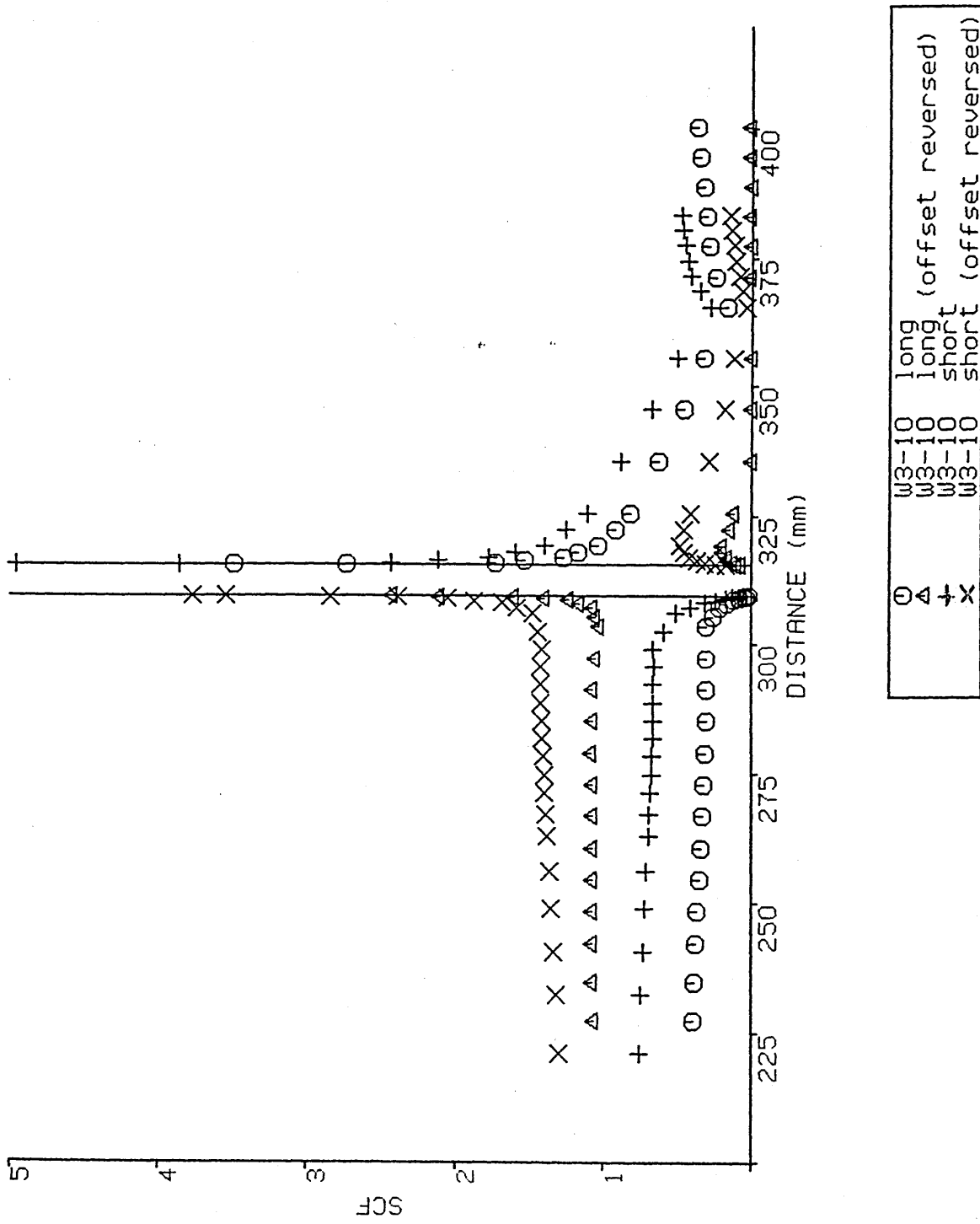
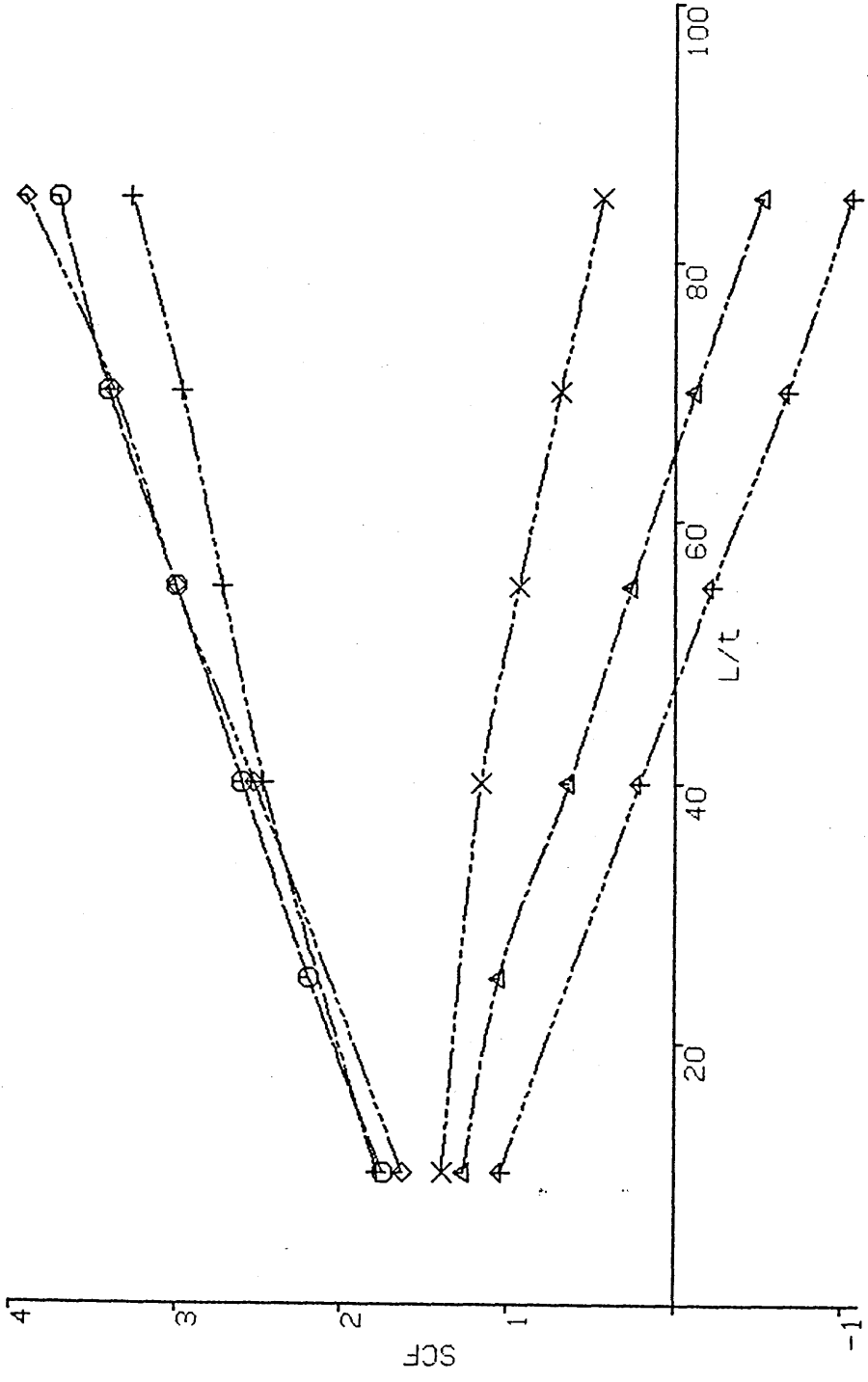


fig 3.6b Effect of length on combined offset and misalignment results



○	△	+	×	◇	△
THICK RATIO = 1:1.5	THICK RATIO = 1:2.0	THICK RATIO = 1:2.0	THICK RATIO = 1:1.25	THICK RATIO = 1:1.25	THICK RATIO = 2.0
misalignment = -2.0			misalignment = 2.0		

fig 3.6c Effect of length and thickness ratio on combined offset and misalignment results

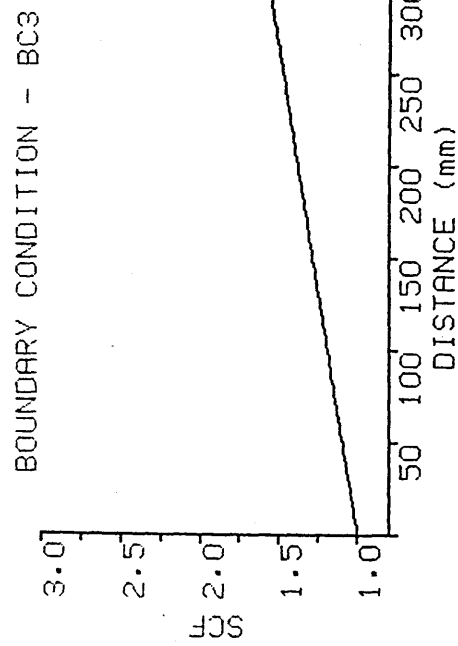
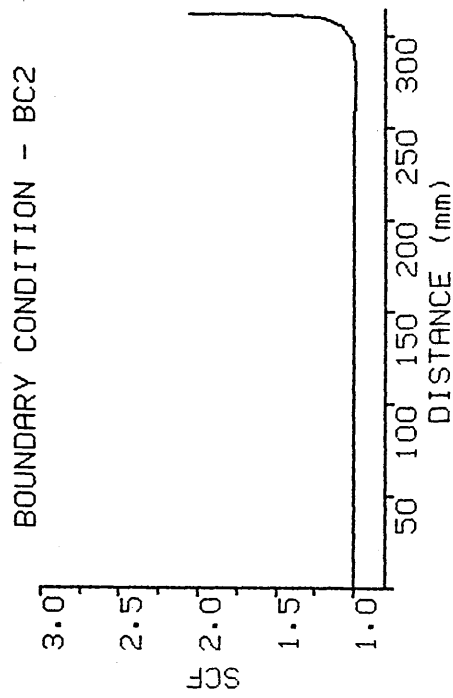
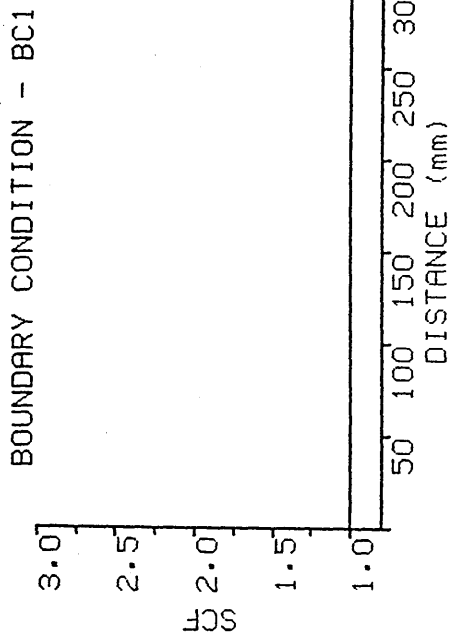
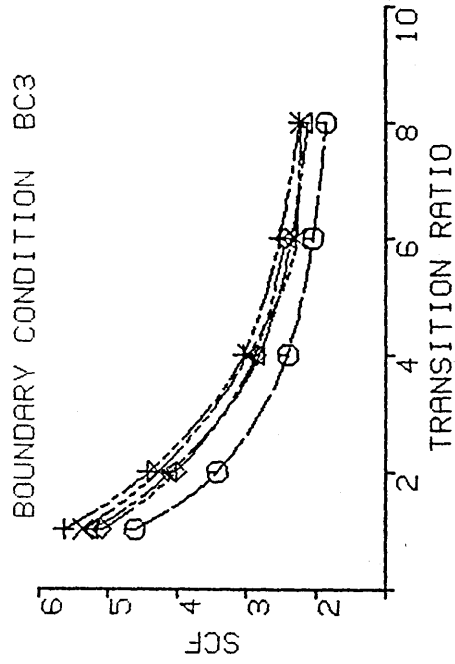
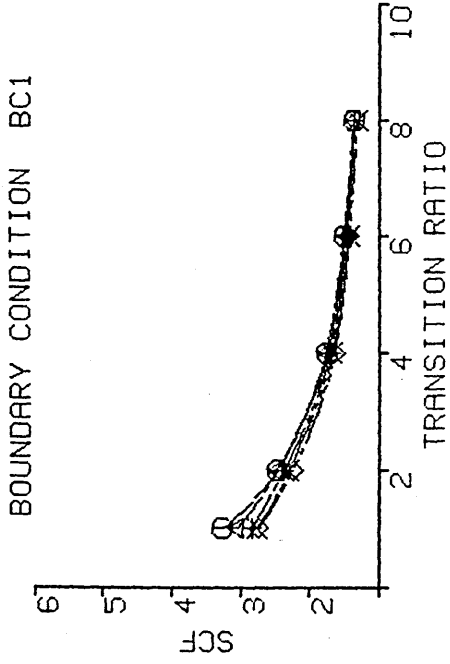
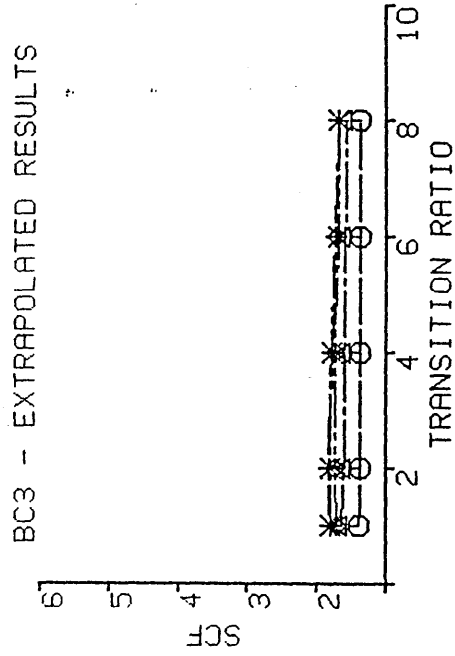
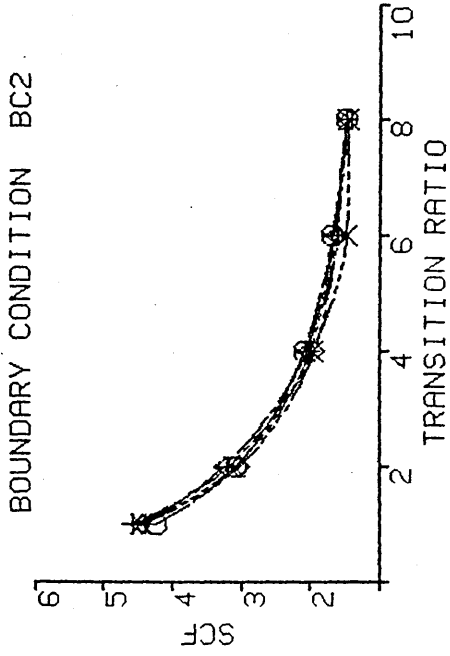


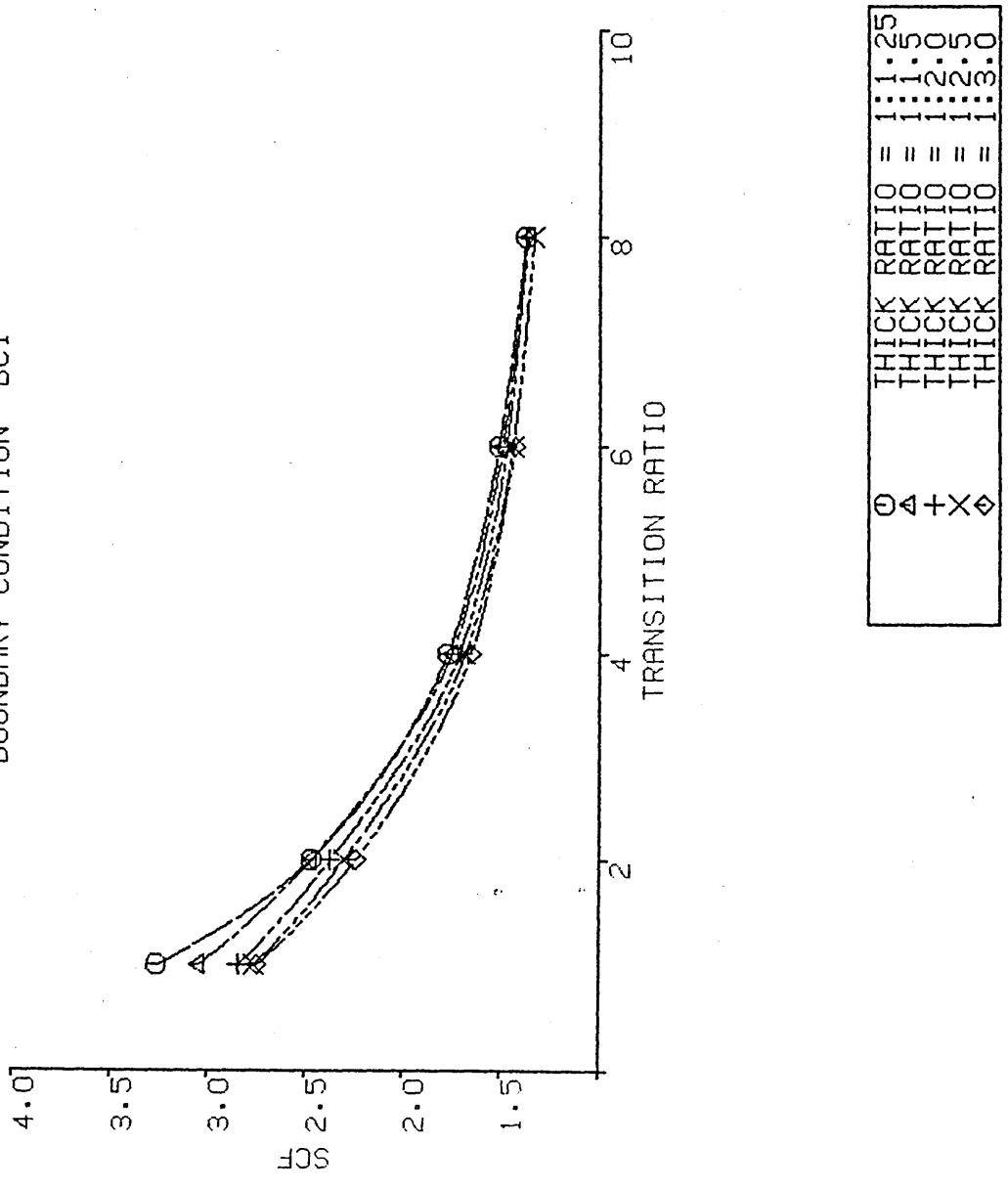
fig.3.7 Stress along top surface of 2-D model



○	THICK RATIO = 1:1:2.5
△	THICK RATIO = 1:1:5
+	THICK RATIO = 1:2:0
X	THICK RATIO = 1:2:5
◇	THICK RATIO = 1:3:0

fig 3.8 Effect on SCF of varying transition ratio

BOUNDARY CONDITION BC1



O	THICK RATIO = 1:1
+	THICK RATIO = 1:2
X	THICK RATIO = 1:3
◇	THICK RATIO = 1:5

fig 3.8a Effect on SCF of varying transition ratio (BC1)

BOUNDARY CONDITION BC2

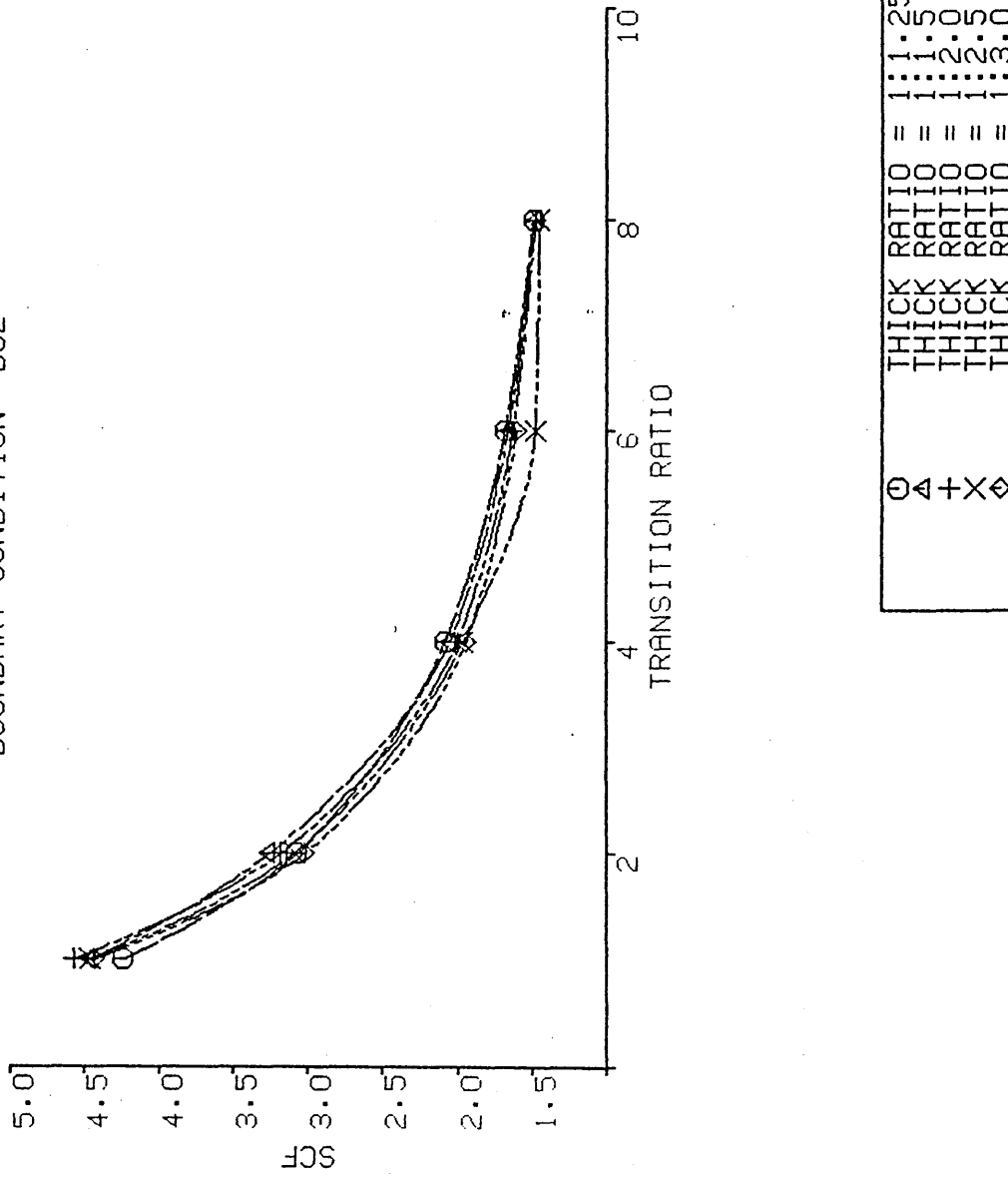


fig 3.8b Effect on SCF of varying transition ratio (BC2)

BOUNDARY CONDITION BC3

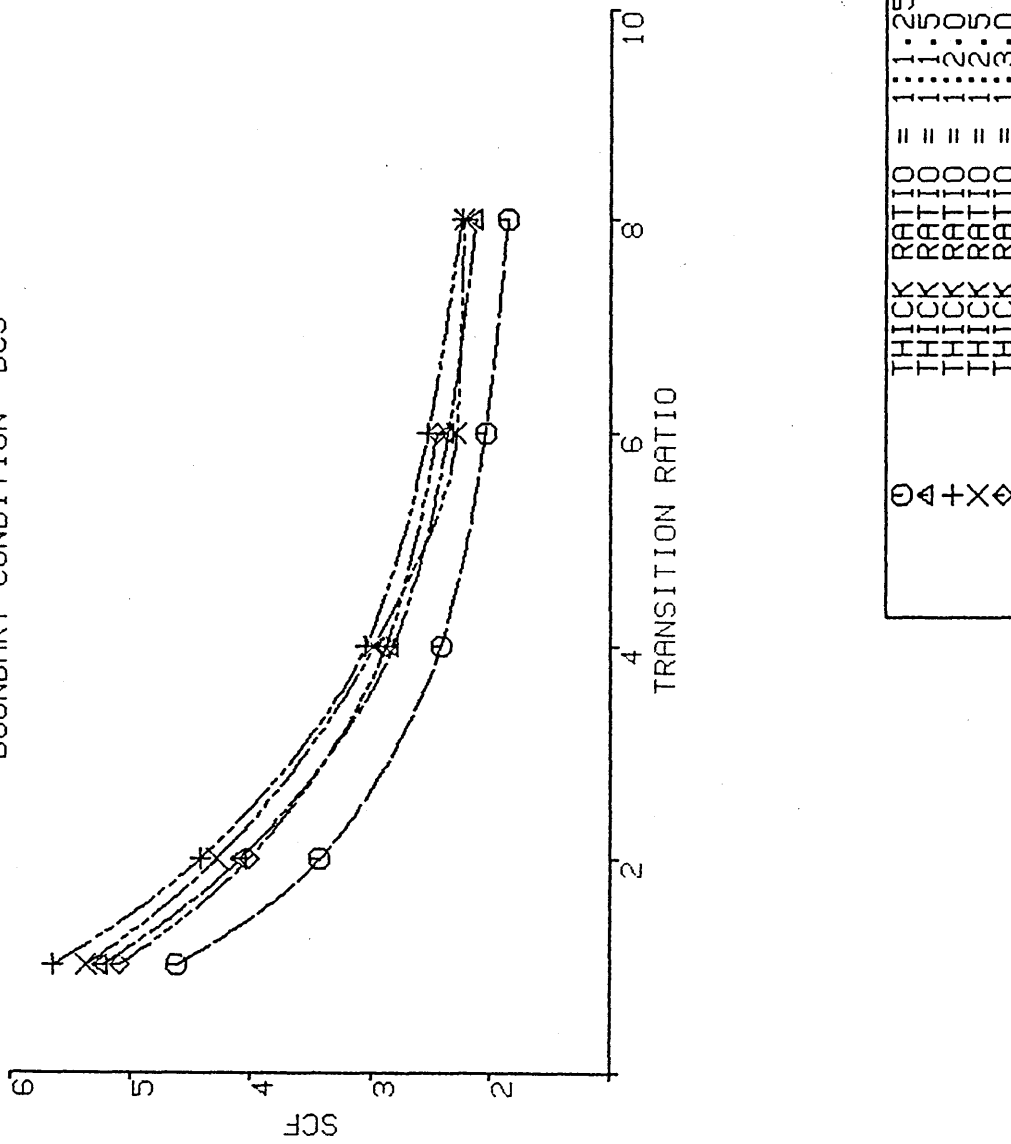


fig 3.8c Effect on SCF of varying transition ratio (BC3, SESAM results)

BC3 - EXTRAPOLATED RESULTS

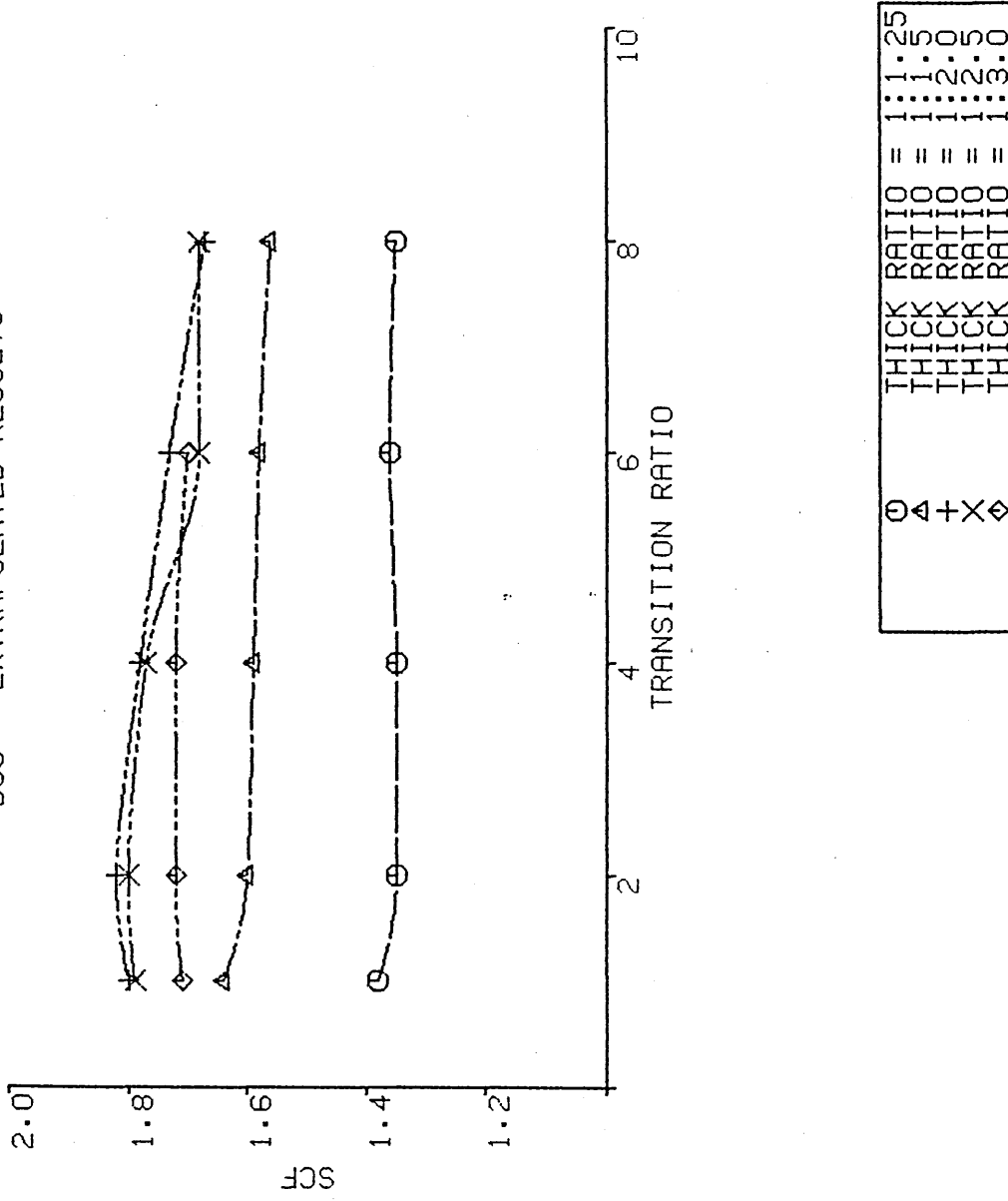


fig 3.8d Effect on SCF of varying transition ratio (BC3, extrapolated results)

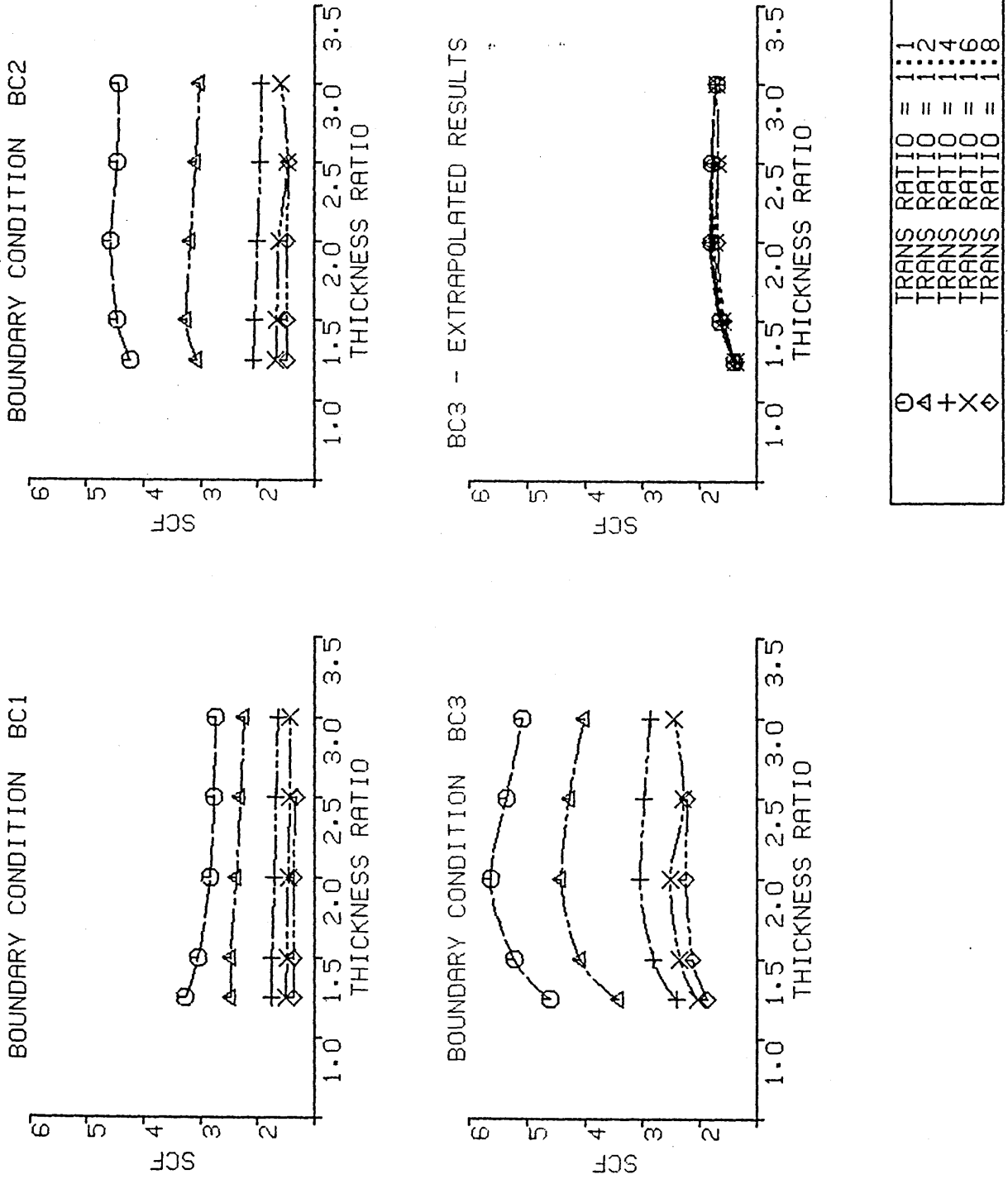


fig 3.9 Effect on SCF of varying thickness ratio

BOUNDARY CONDITION BC1

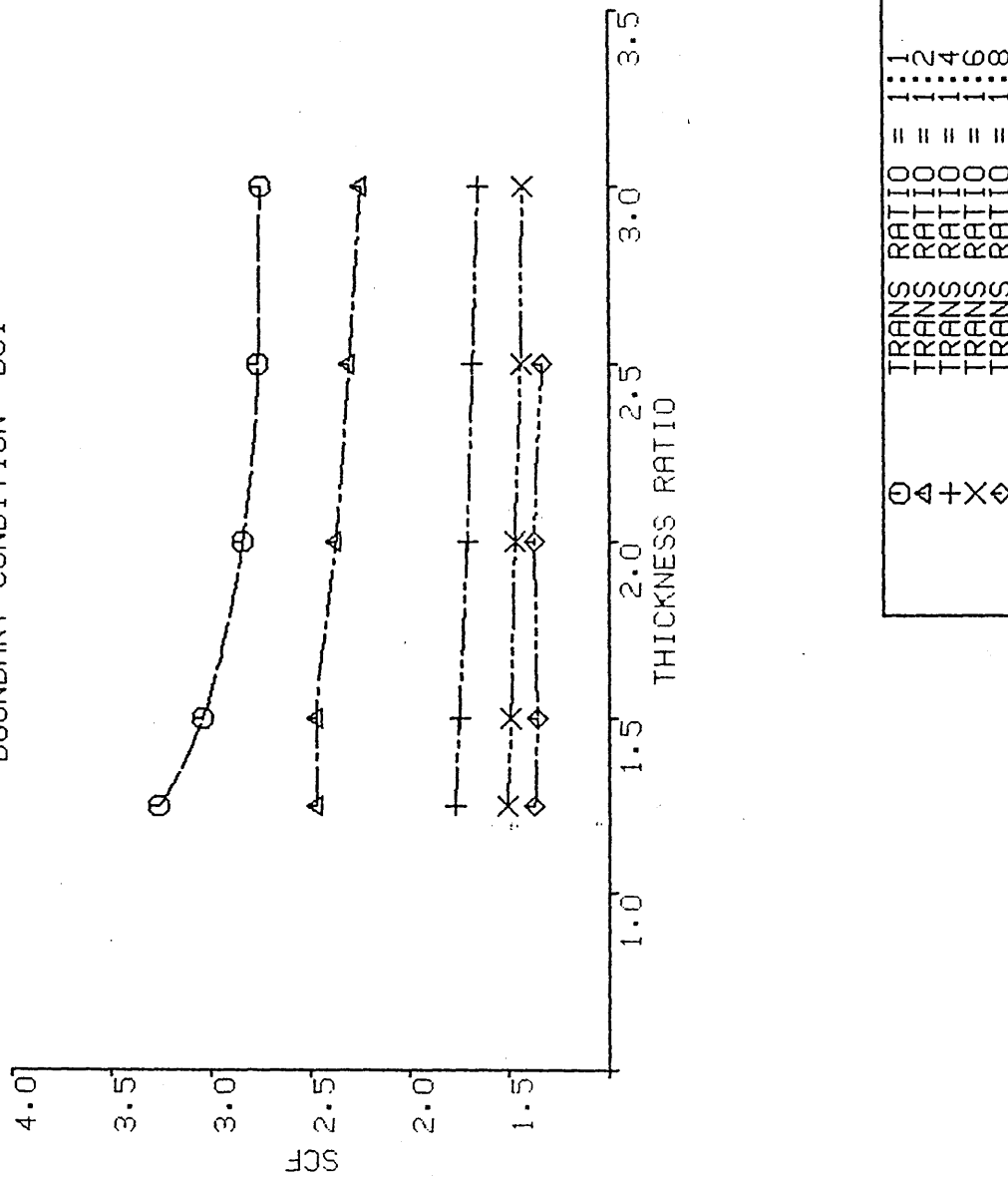


fig 3.9a Effect on SCF of varying thickness ratio (BC1)

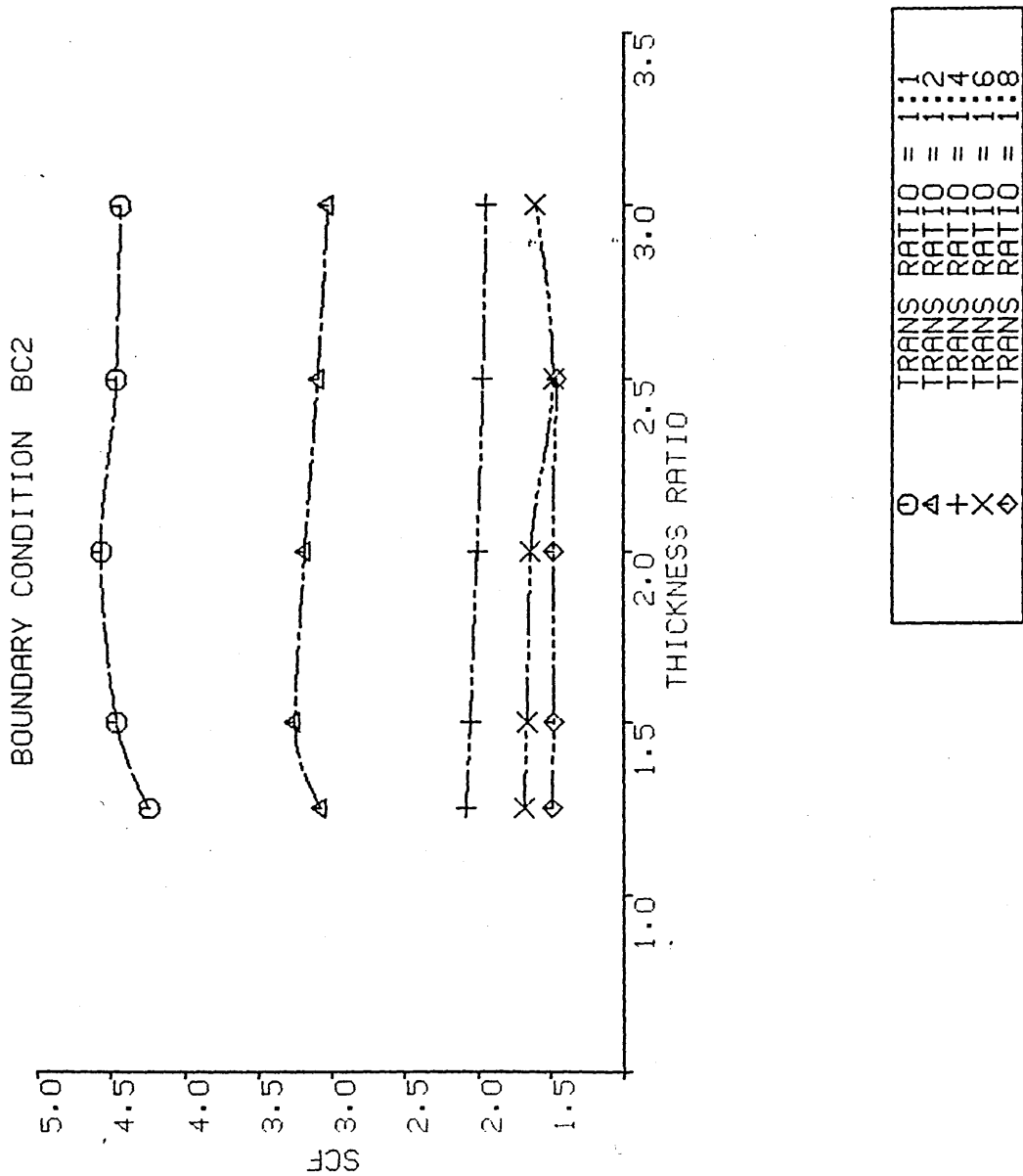


fig 3.9b Effect on SCF of varying thickness ratio (BC2)

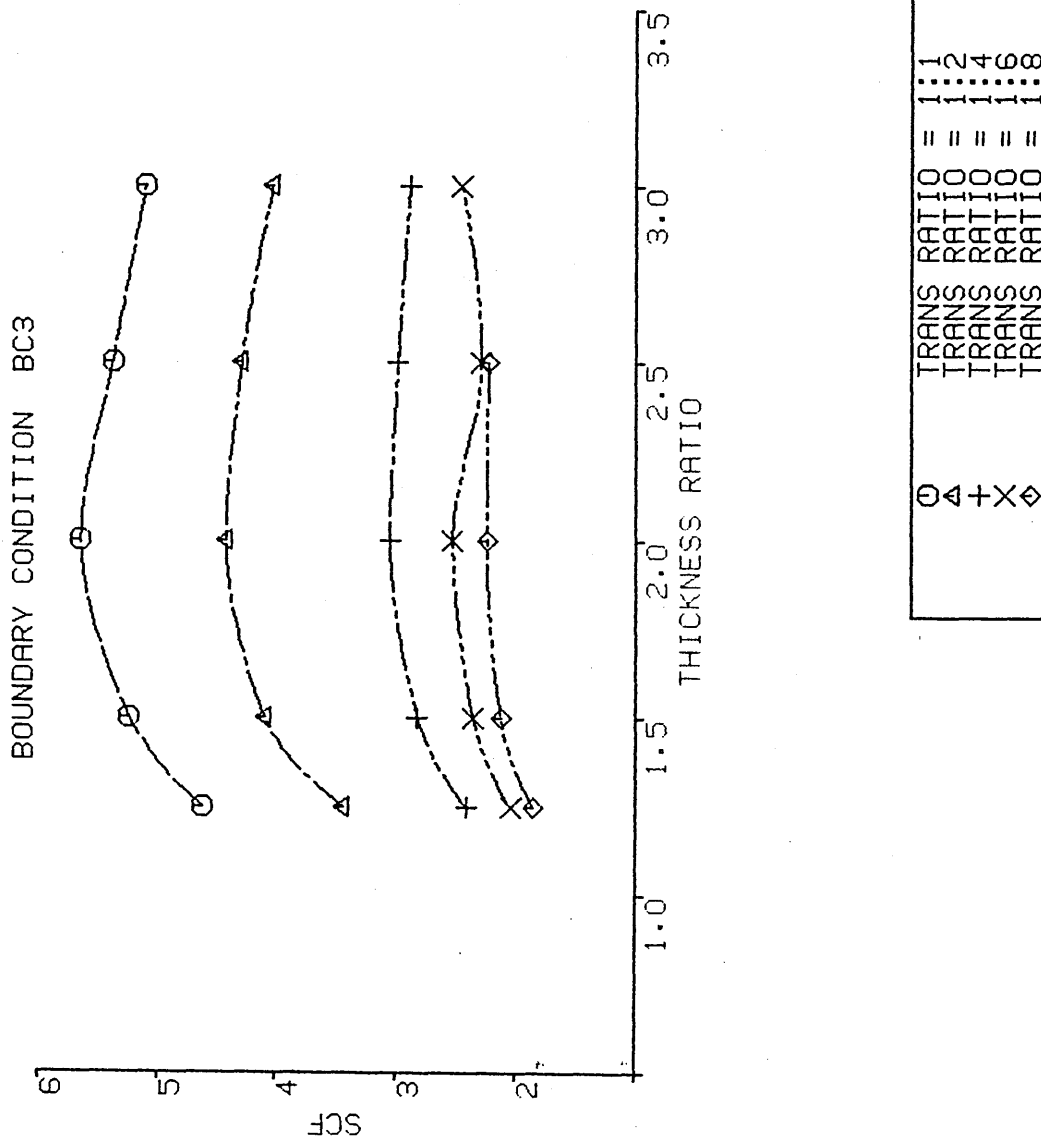


fig 3.9c Effect on SCF of varying thickness ratio (BC3, SESAM results)

BC3 - EXTRAPOLATED RESULTS

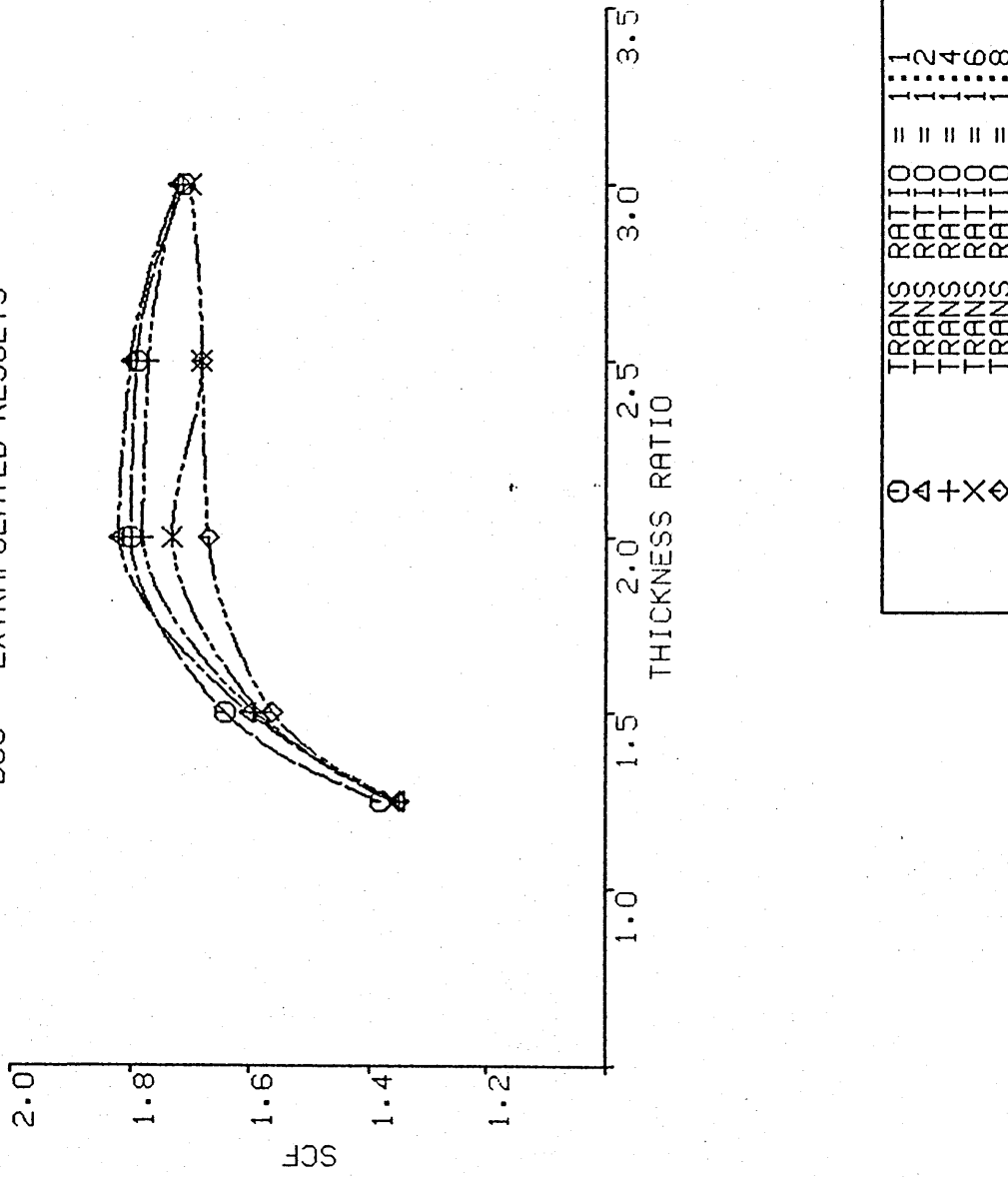


fig 3.9d . Effect on SCF of varying thickness ratio (BC3, extrapolated results)

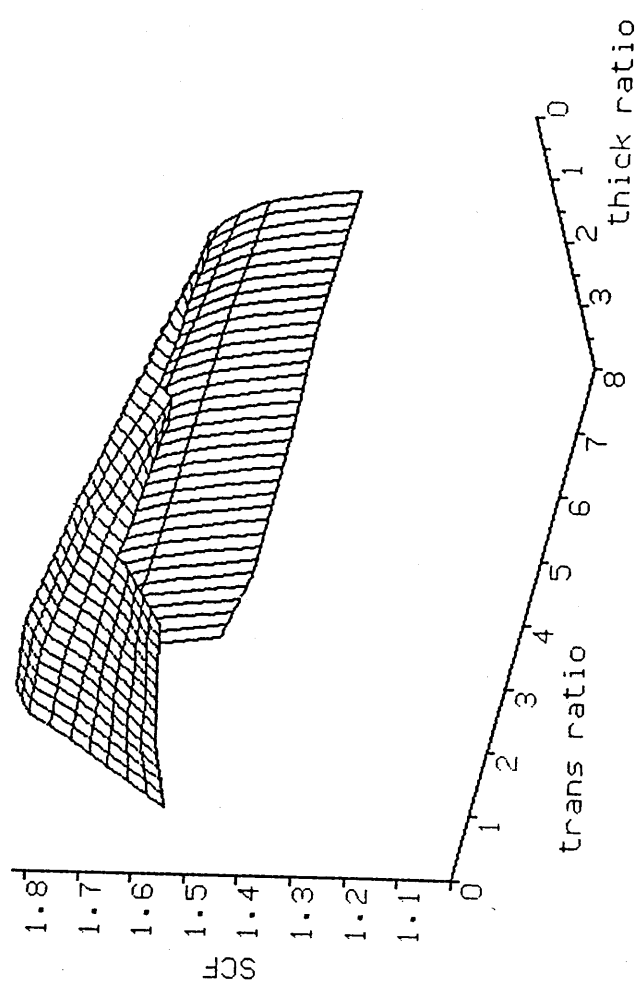
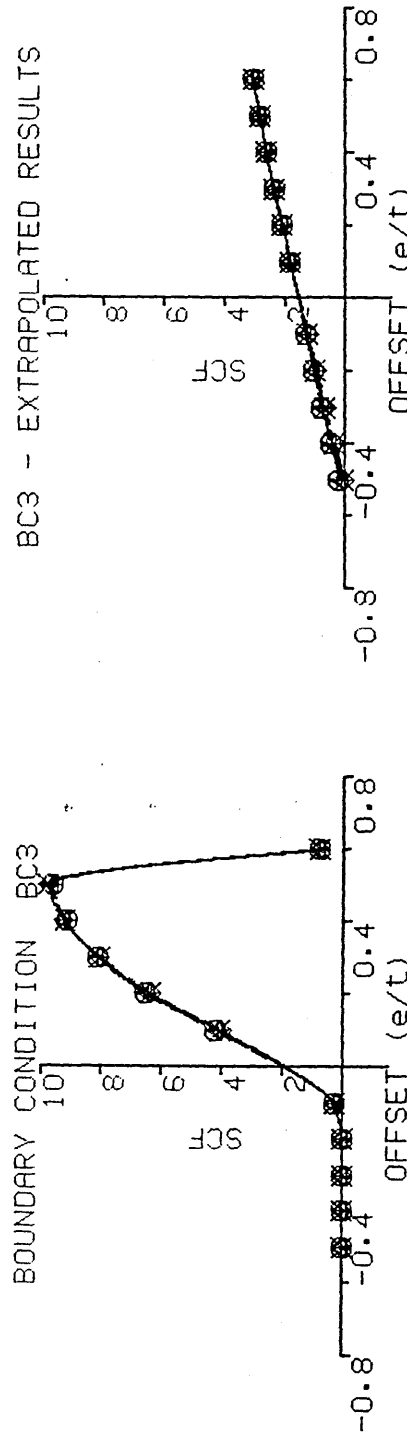
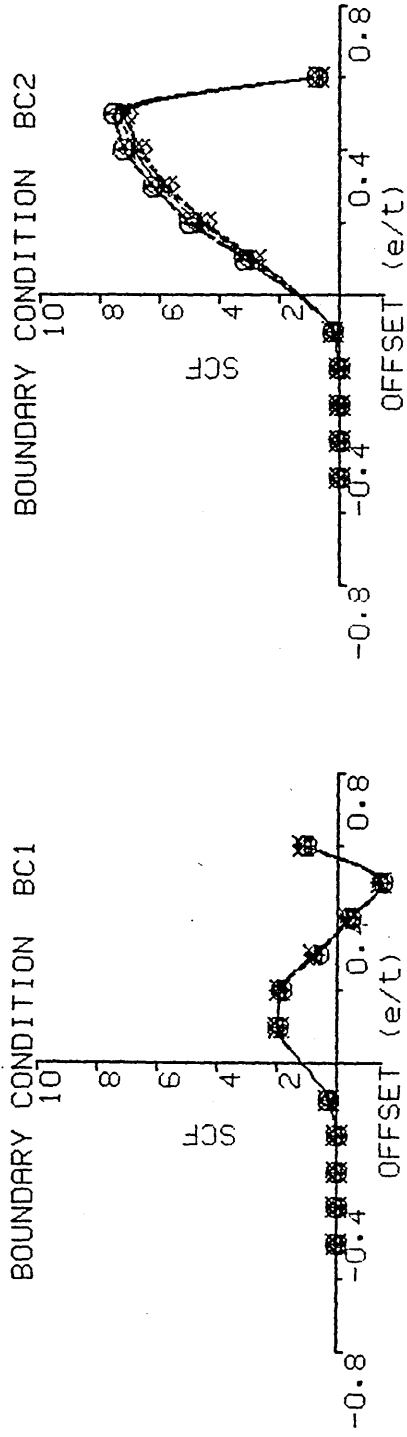


fig 3.9e Effect on SCF of transition and thickness ratio (BC3, extrapolated results)



○	4	+	◇
TRANS RATIO =	1:2	TOP	WELD
TRANS RATIO =	1:4	TOP	WELD
TRANS RATIO =	1:6	TOP	WELD
TRANS RATIO =	1:8	TOP	WELD

fig 3.10 Effect on SCF of varying offset

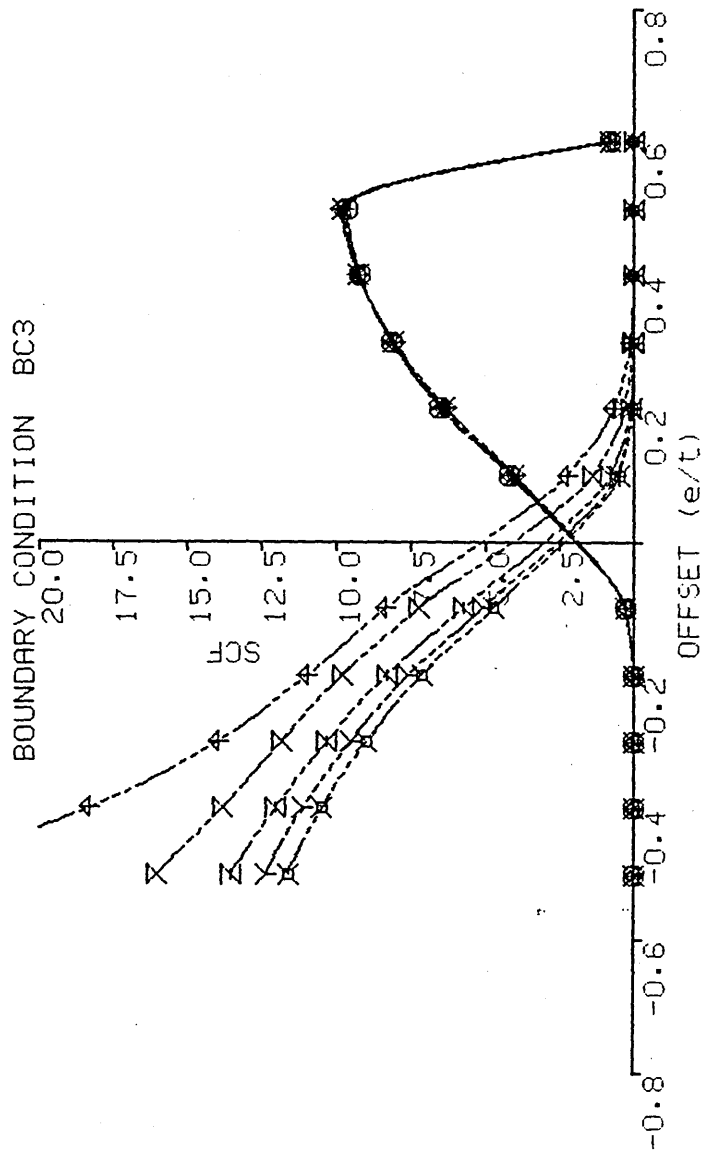


fig 3.10c Effect on SCF of varying offset (BC3, SESAM results)

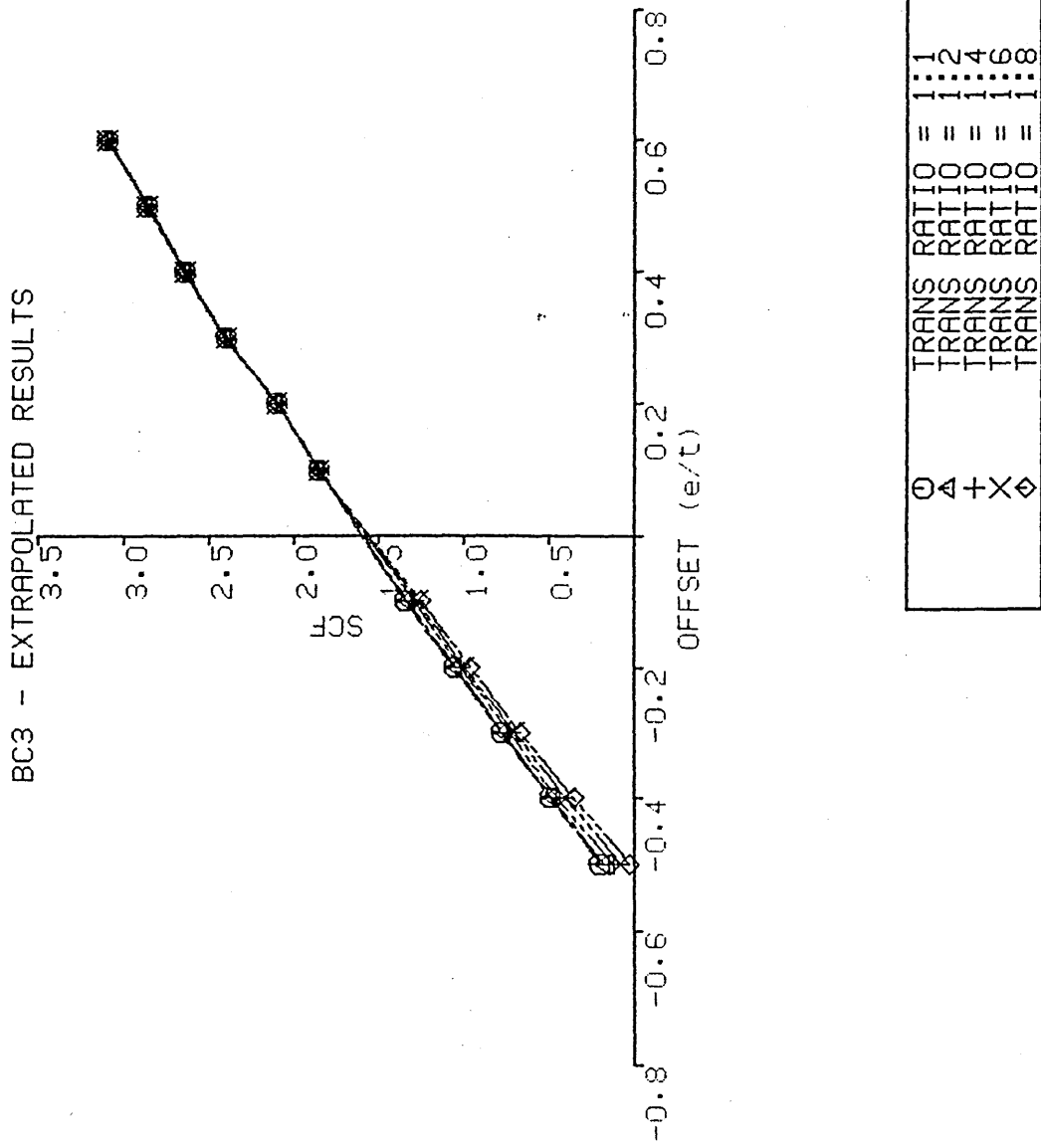
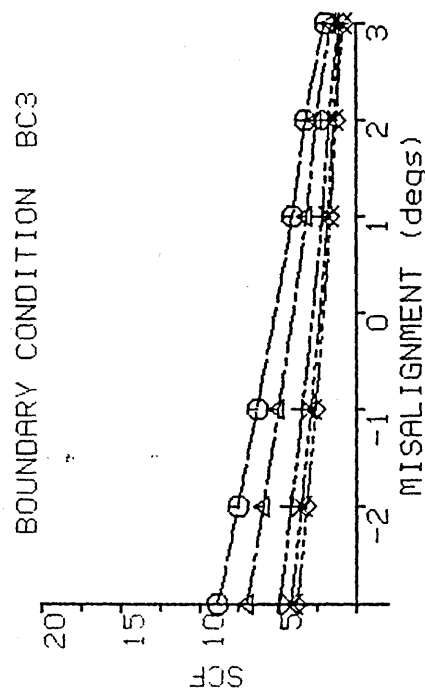
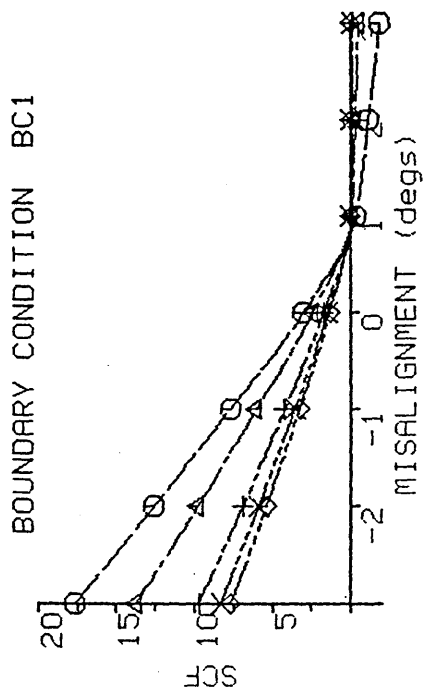
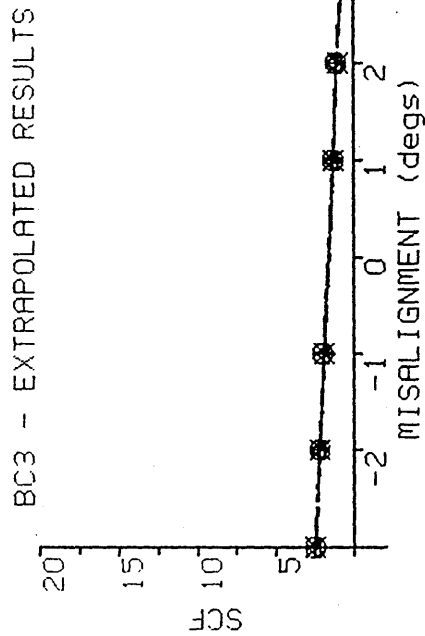
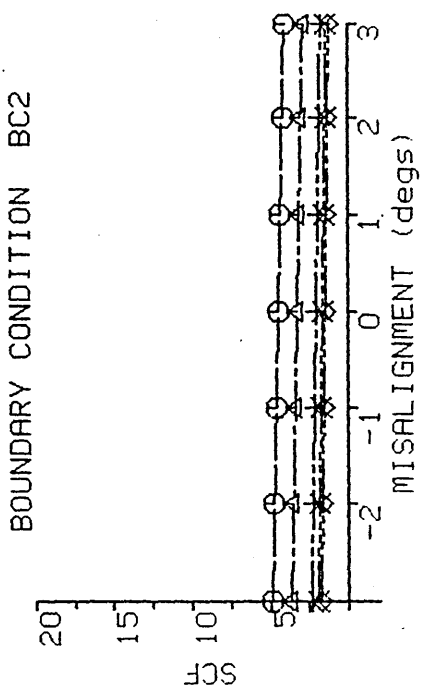


fig 3.10d Effect on SCF of varying offset (BC3, extrapolated results)



○	△	×	◇
TRANS RATIO = 1:1			
TRANS RATIO = 1:2			
TRANS RATIO = 1:4			
TRANS RATIO = 1:6			
TRANS RATIO = 1:8			

fig 3.11 Effect on SCF of varying misalignment.

BOUNDARY CONDITION BC1

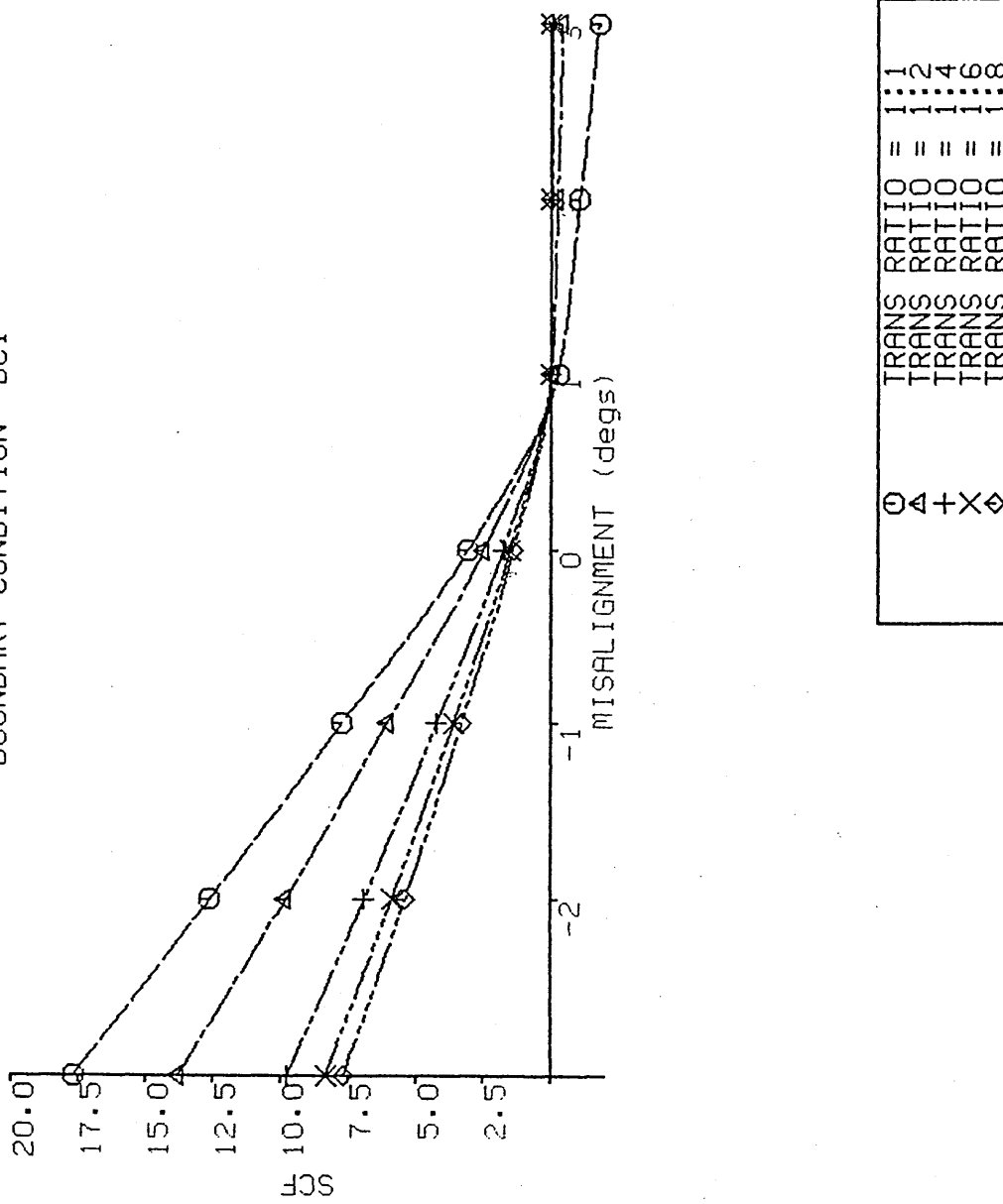


fig 3.11a Effect on SCF of varying misalignment (BC1)

BOUNDARY CONDITION BC2

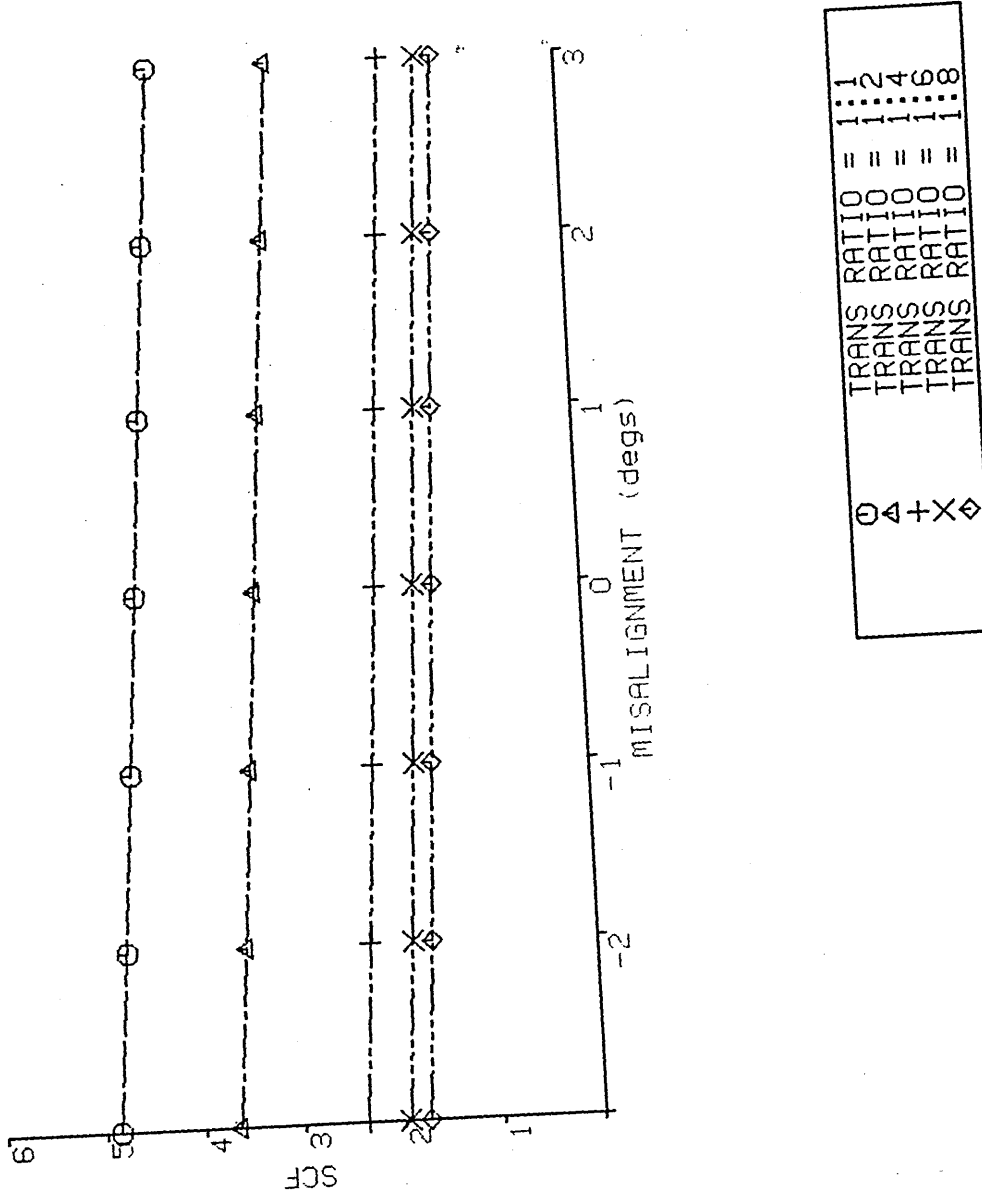
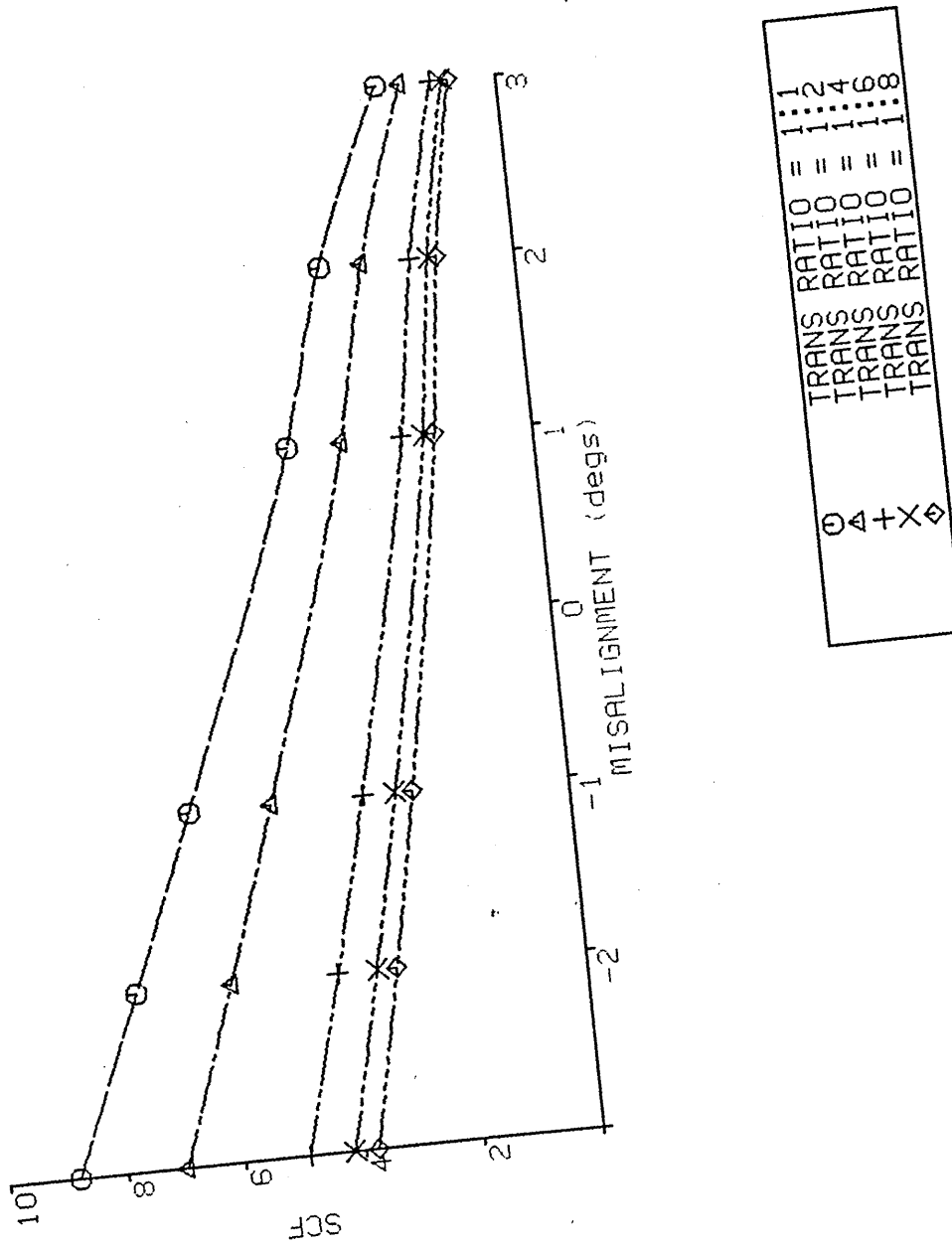


fig 3.11b Effect on SCF of varying misalignment (BC3)

BOUNDARY CONDITION BC3



Effect on SCF of varying misalignment (BC3, SESAM results)

fig 3.11c

BC3 - EXTRAPOLATED RESULTS

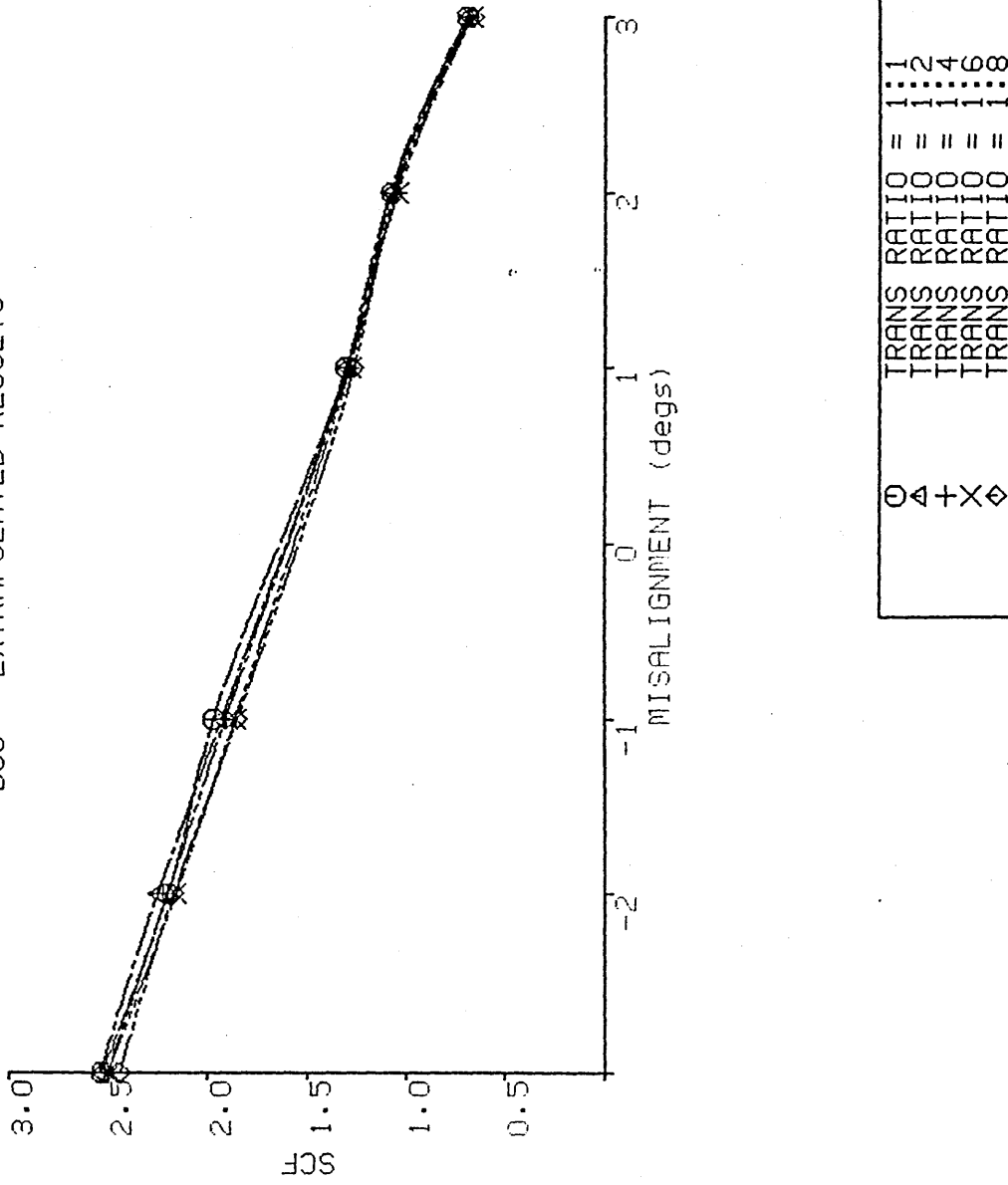


fig 3.11d Effect on SCF of varying misalignment (BC3, extrapolated results)

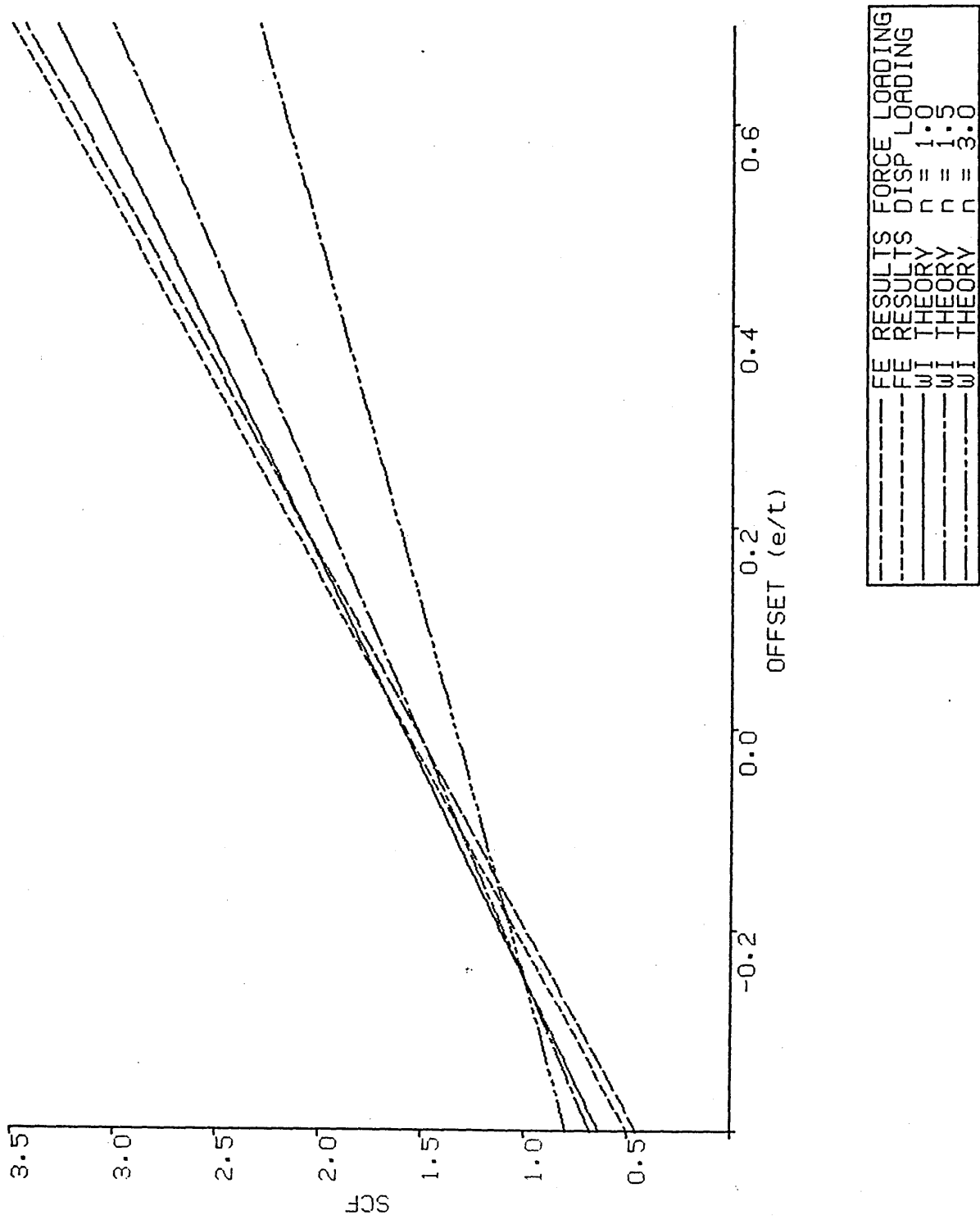


fig 3.12 Comparison of FE and theoretical results for offsets

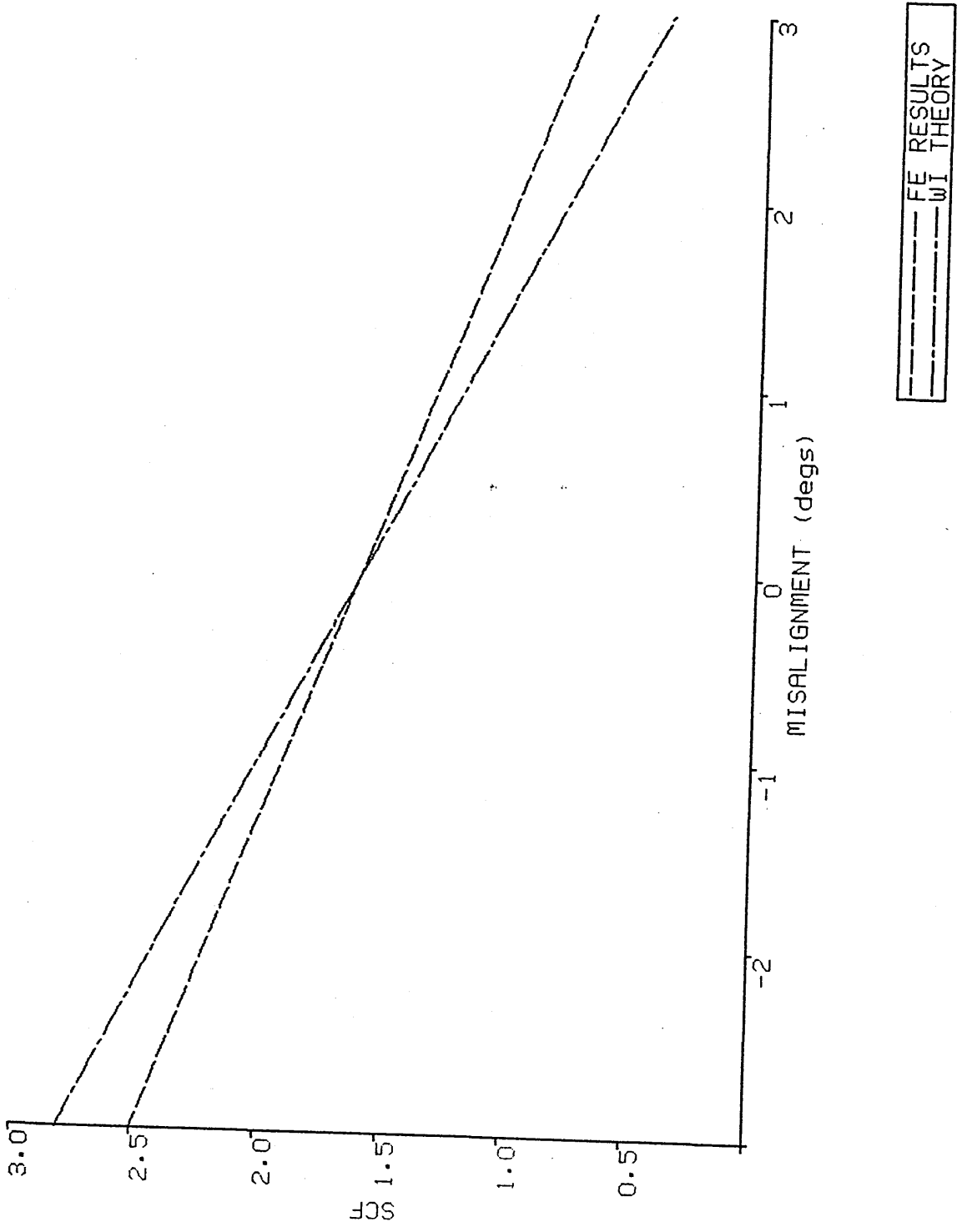


fig 3.13. Comparison of FE and theoretical results for misalignments

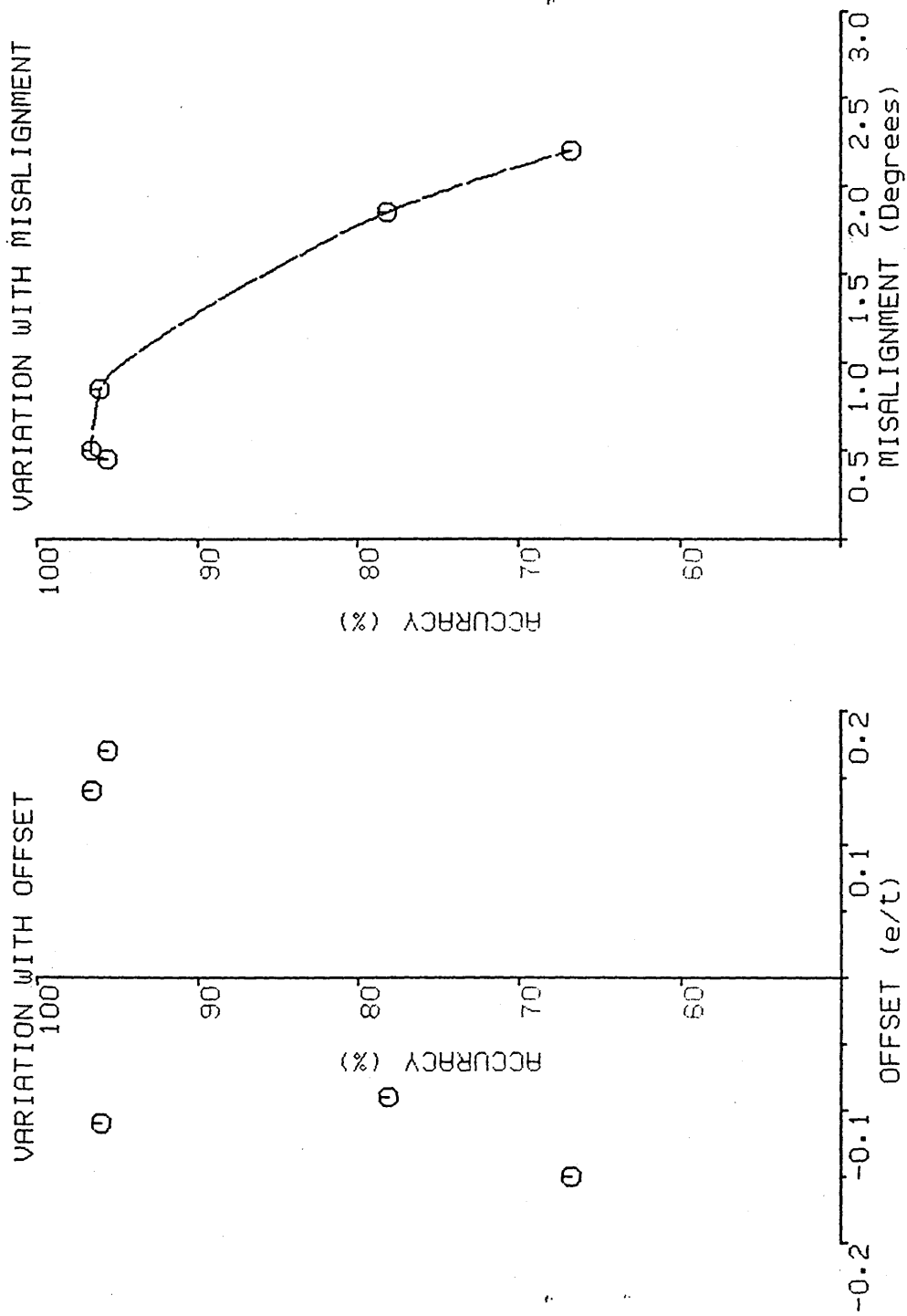


fig 3.14 Accuracy of Eqns for varying offset and misalignment

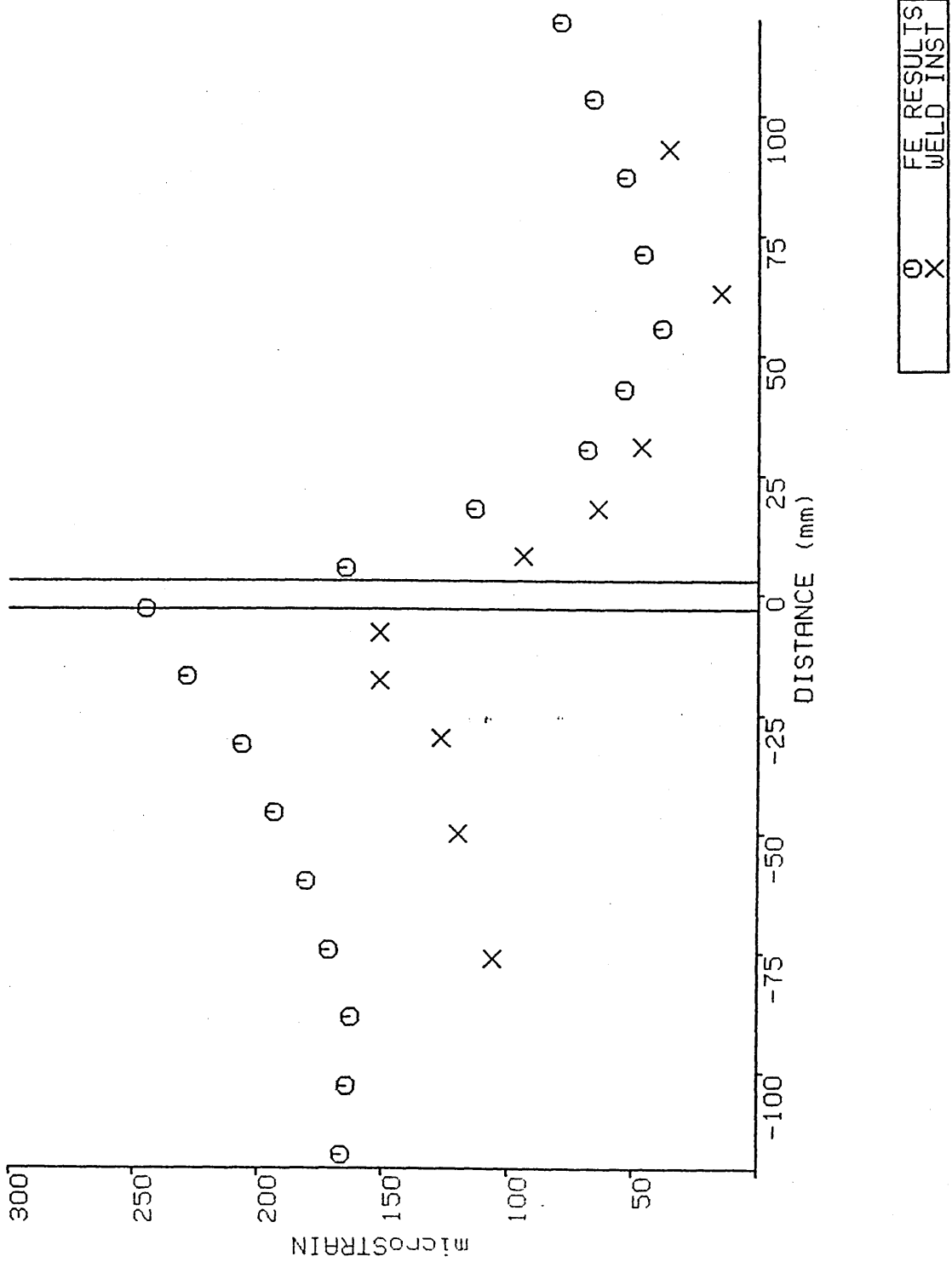


fig 3.15a Comparison of FE results with 4 pt bending test specimen: Applied force = 400kN

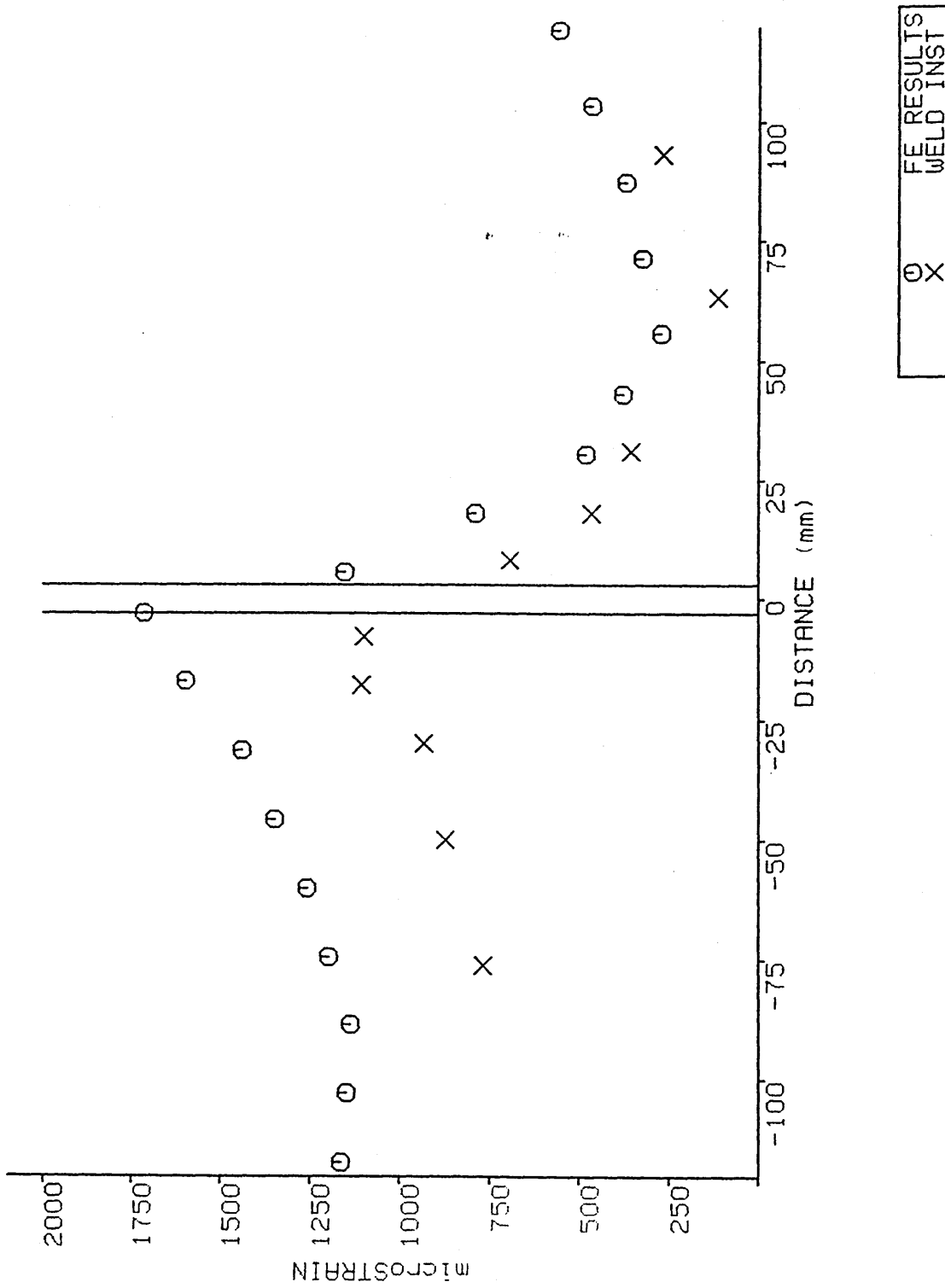


fig 3.15b Comparison of FE results with 4 pt bending test specimen: Applied force = 2800kN

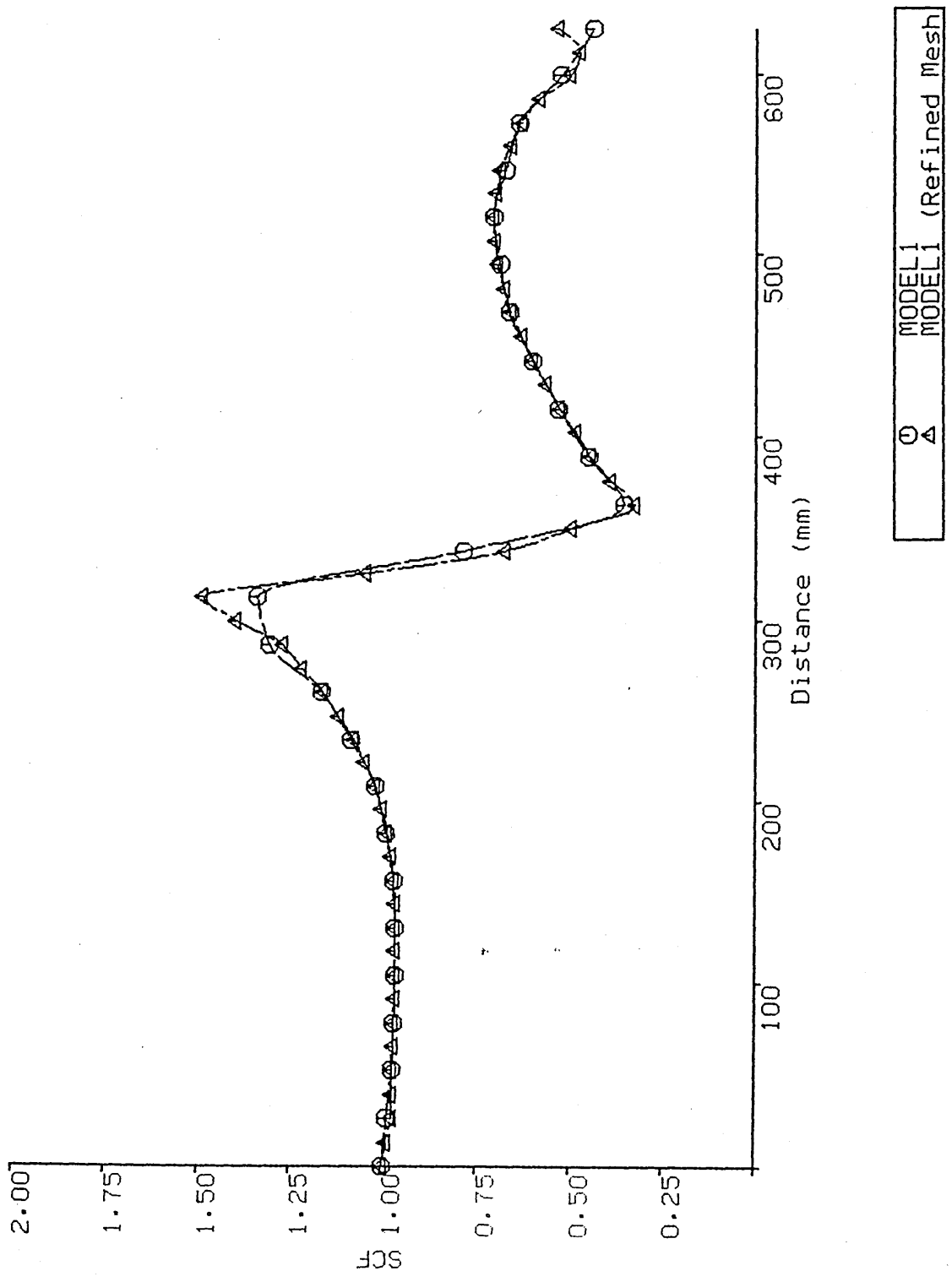


fig 3.16a SCF along inner surface of 3-D model; no offset or misalignment (effect of refinin

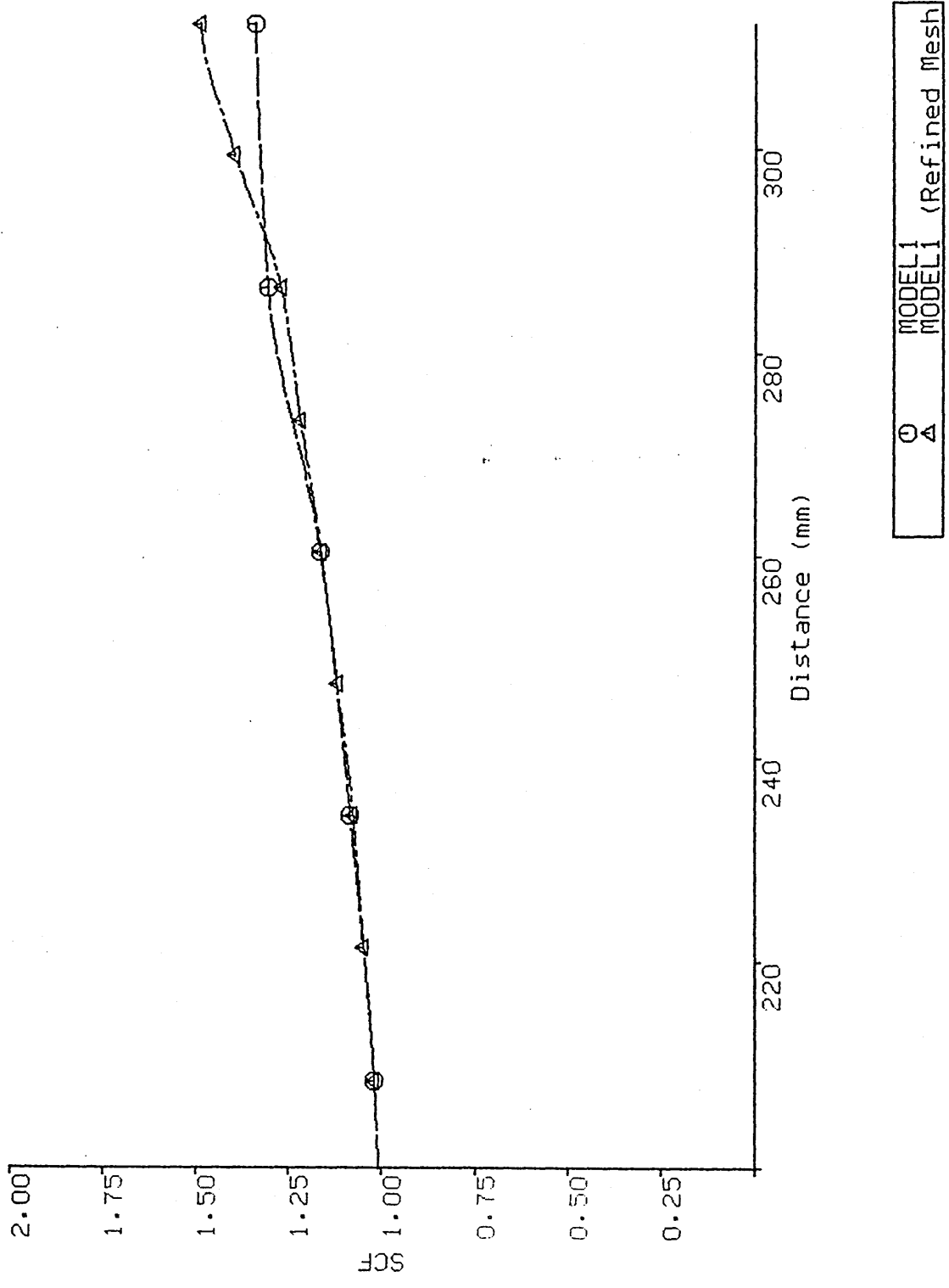


fig 3.16b .SCF along inner surface of 3-D model near to weld (effect of refining mesh)

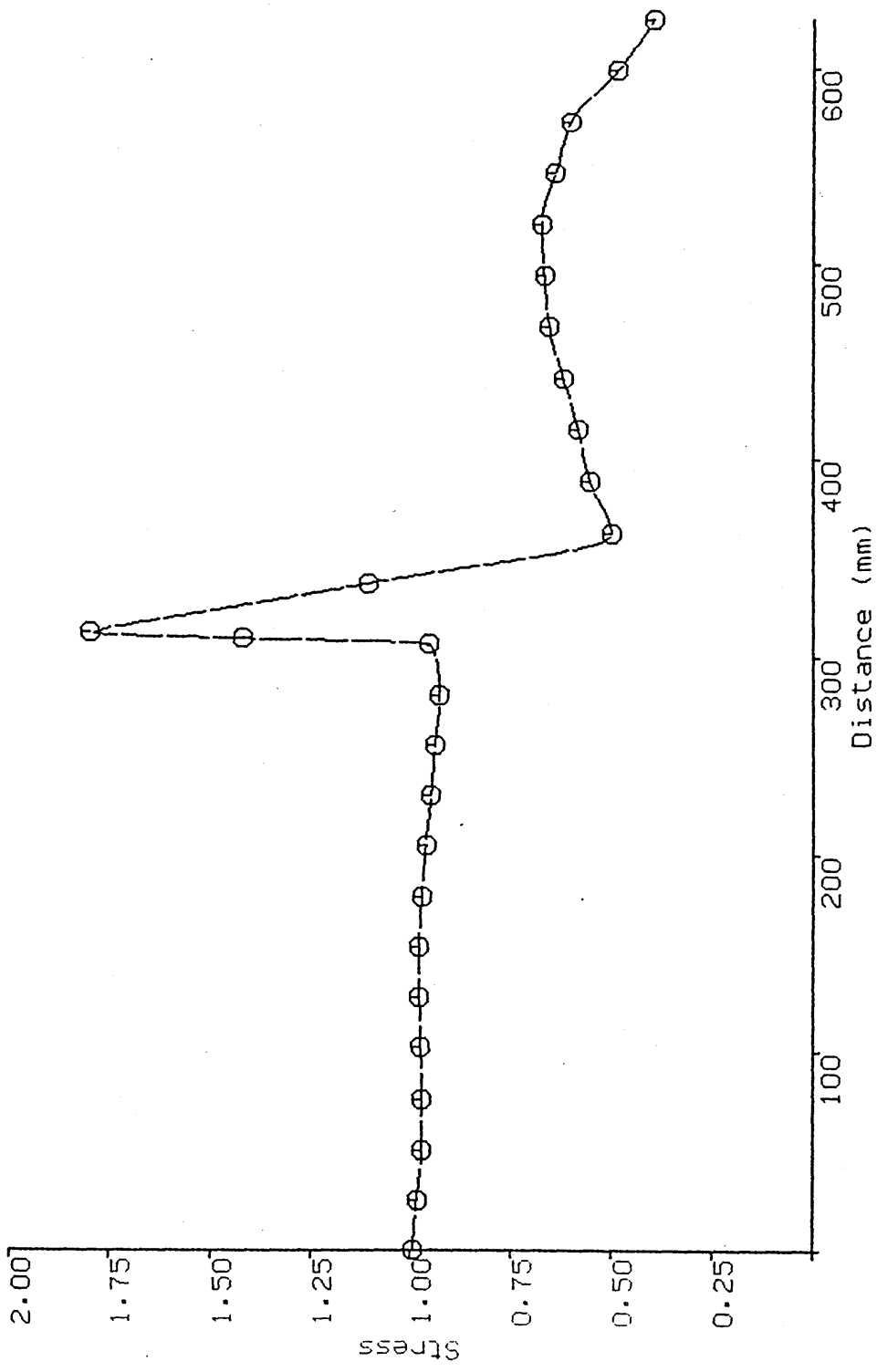


fig 3.17a SCF along inner surface of 3-D model with -0.2 offset

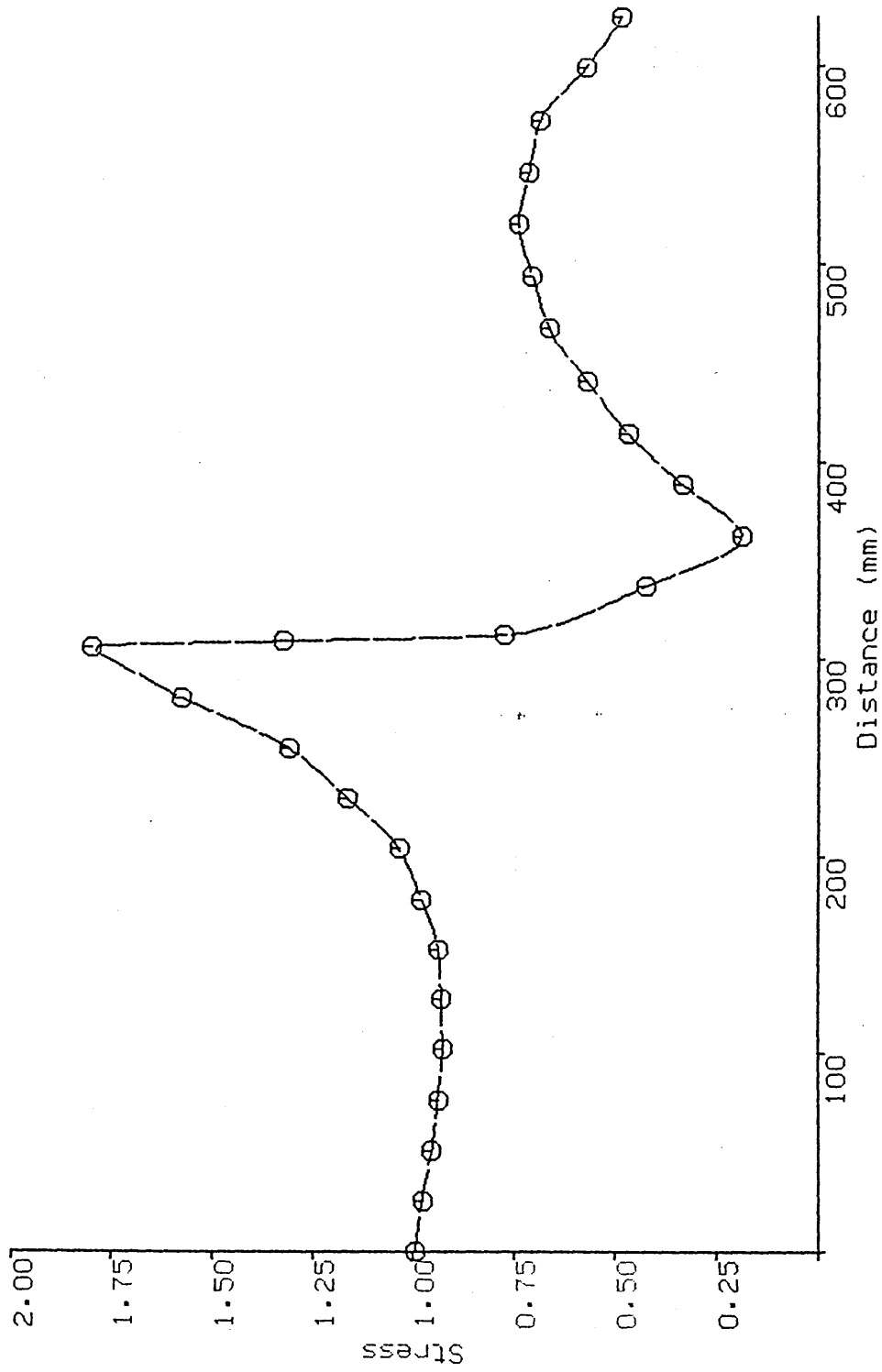


fig 3.17b SCF along inner surface of 3-D model with +0.2 offset

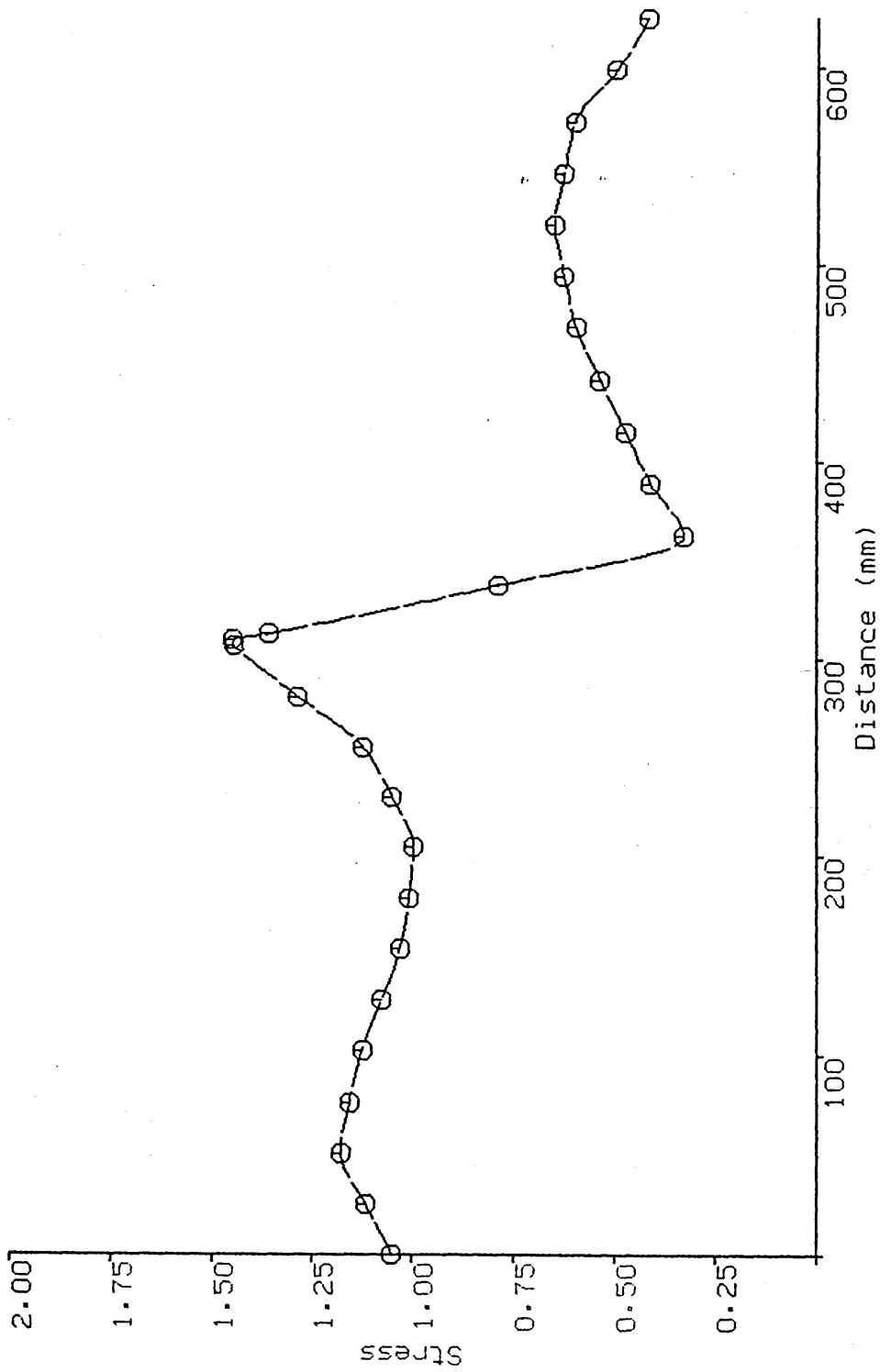


fig 3.18a SCF along inner surface of 3-D model with -2.0 deg misalignment

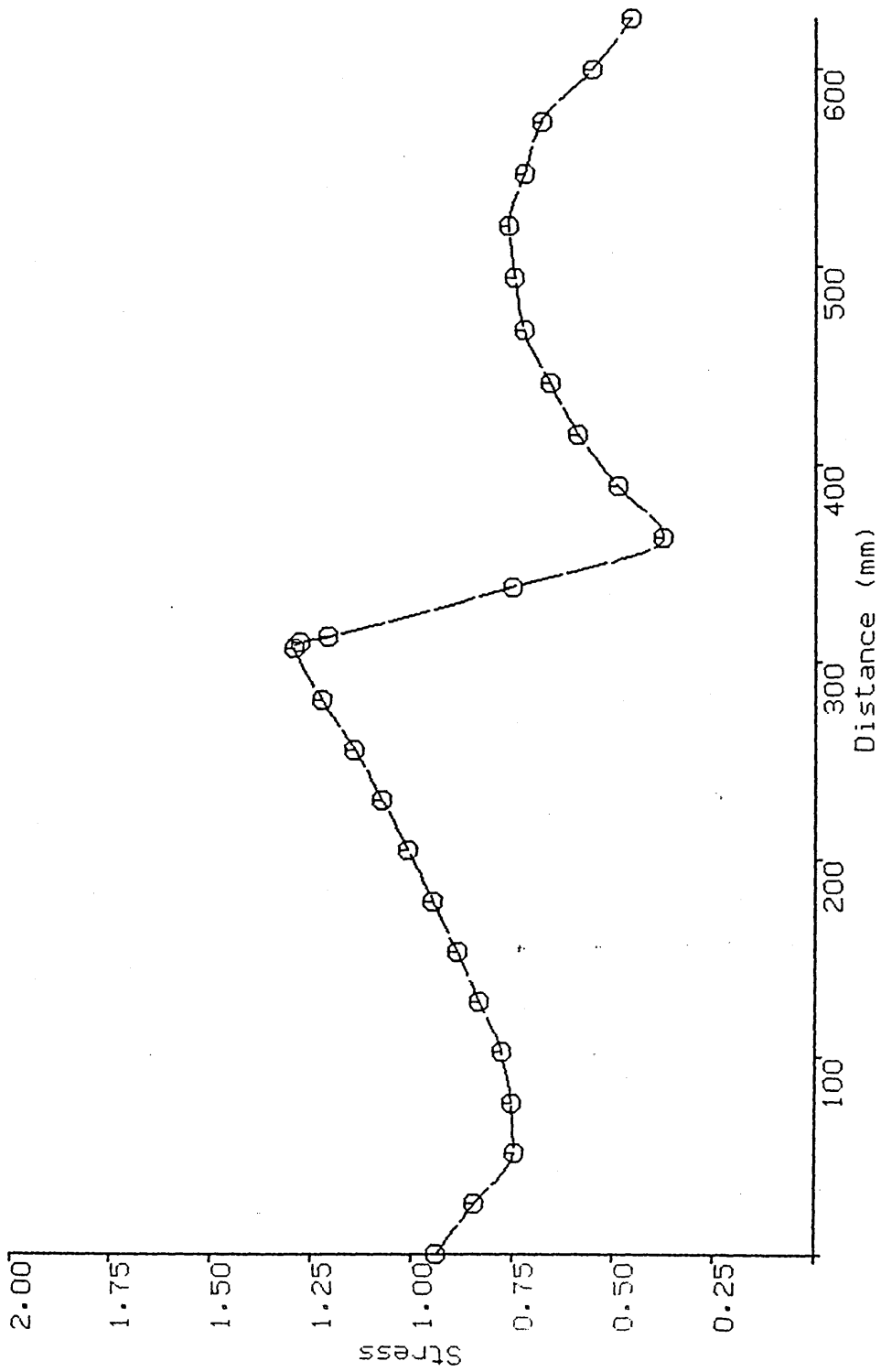


fig 3.18b SCF along inner surface of 3-D model with 2.0 deg misalignment

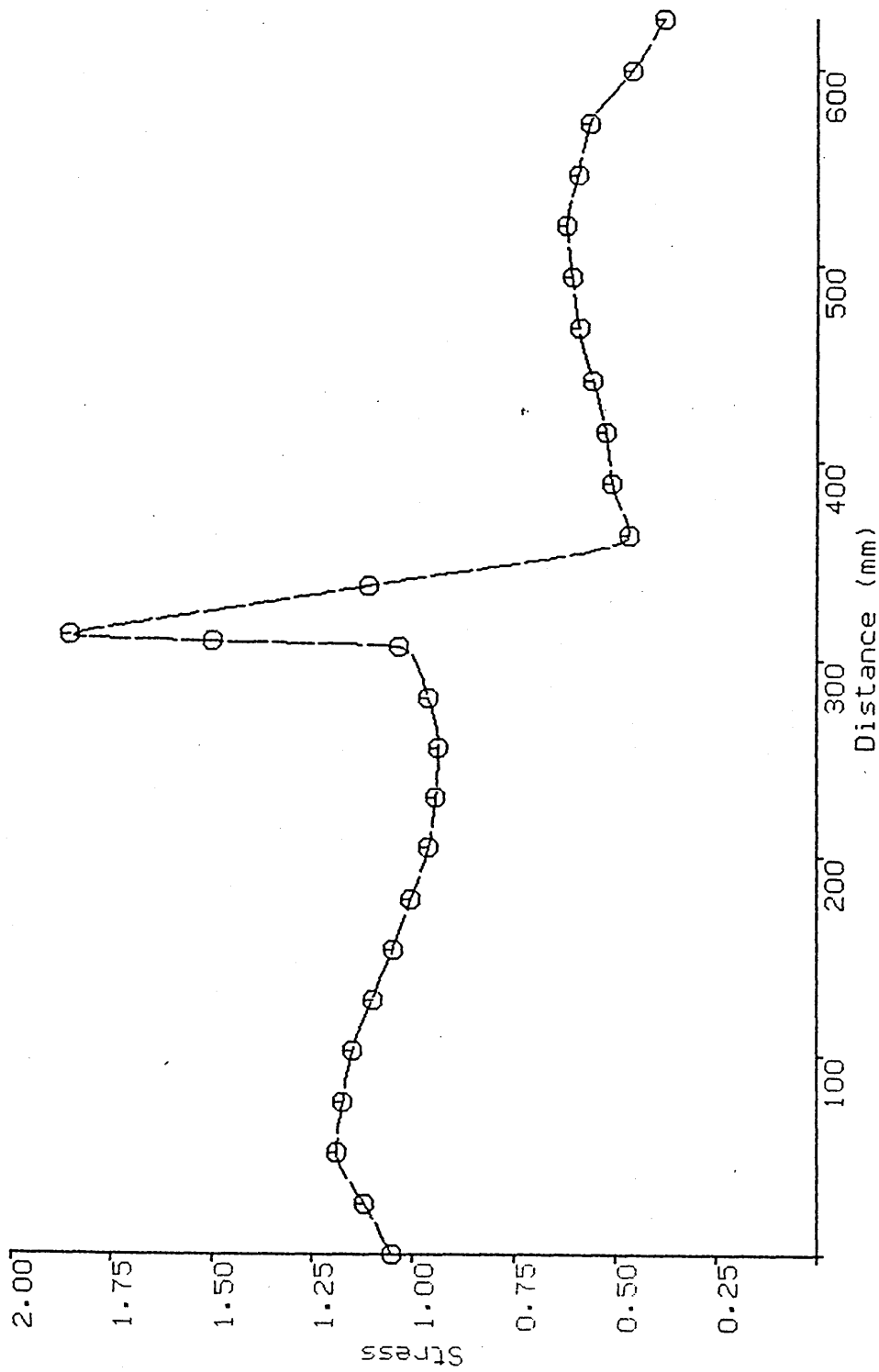


fig 3.19a SCF along inner surface of 3-D model with offset (-0.2) & misalignment (-2.0 deg)

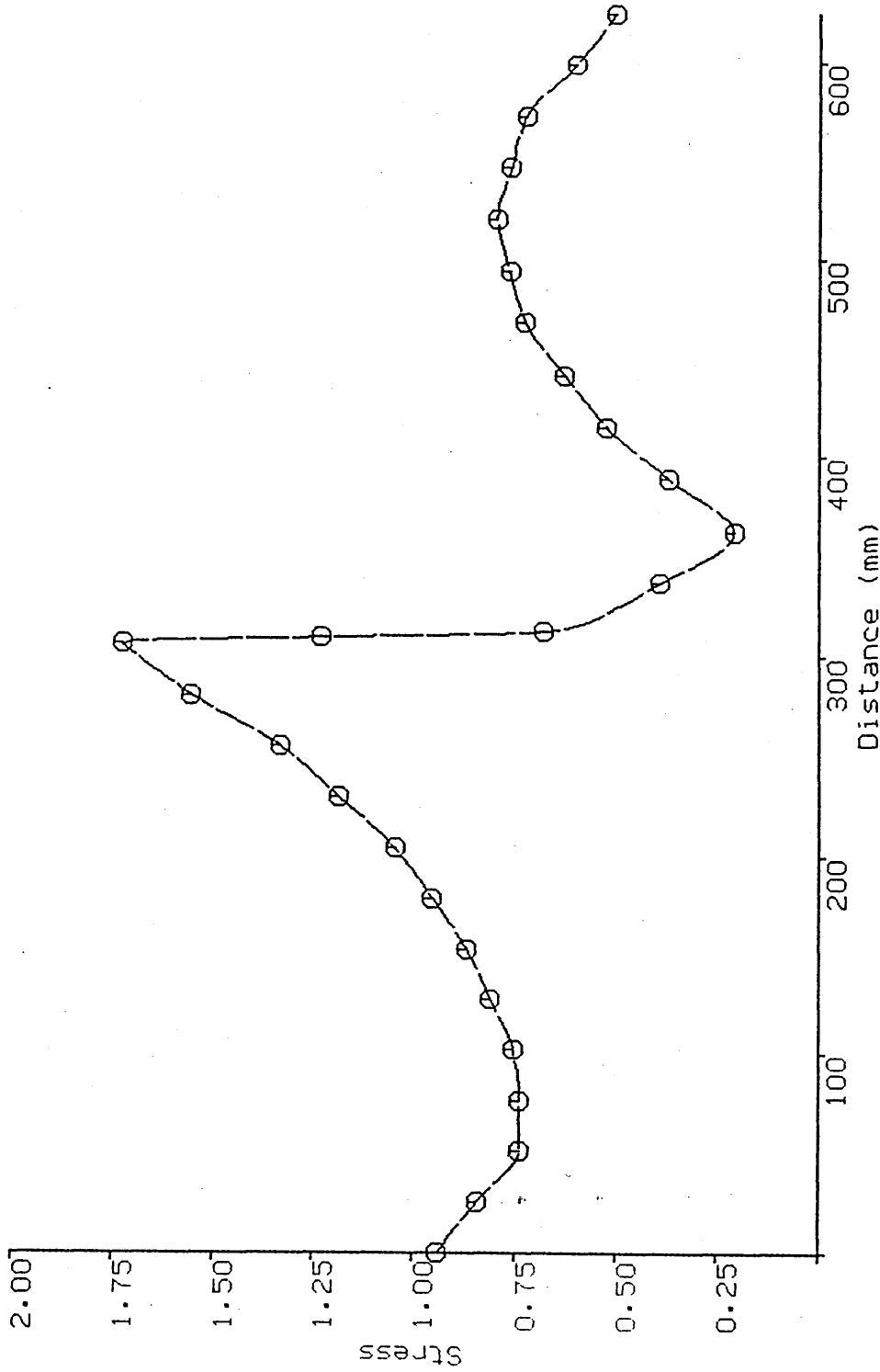
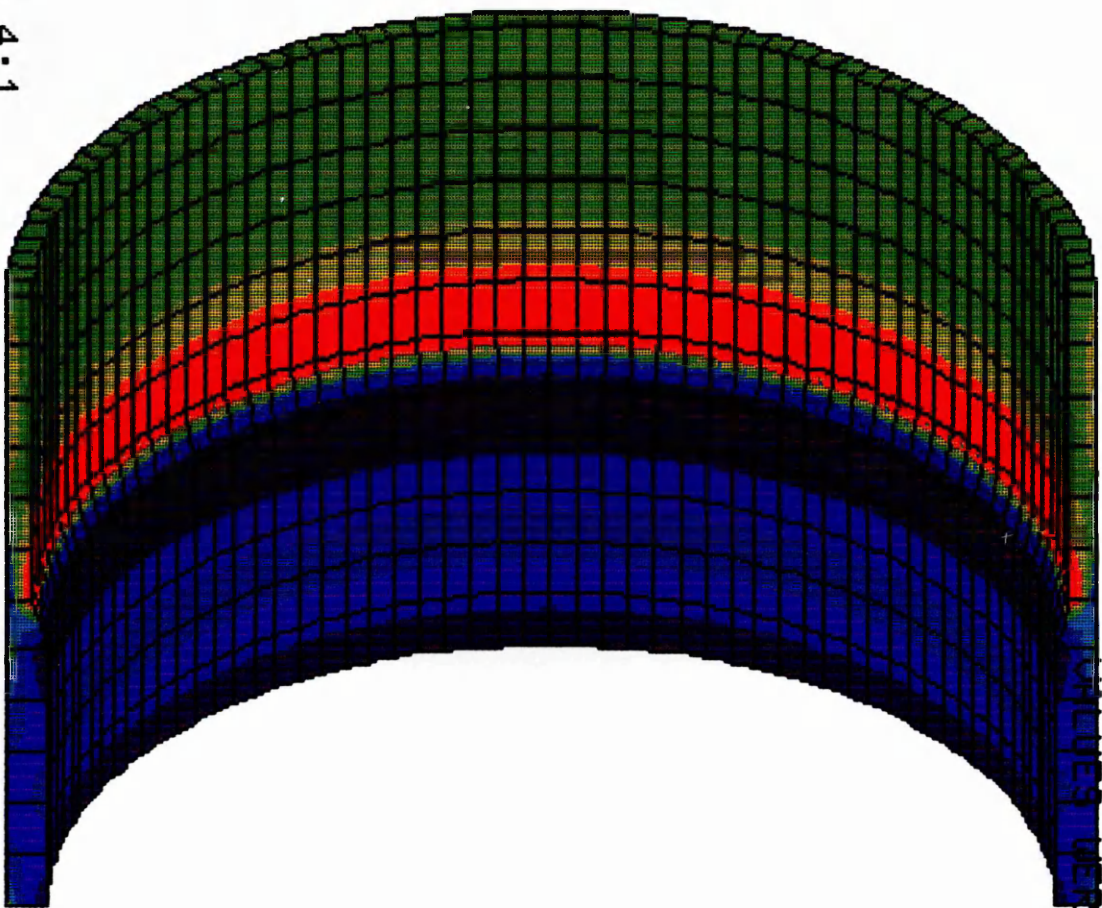


fig 3.19b SCF along inner surface of 3-D model with offset (0.2) & misalignment (2.0 deg)

SESAM
POSTFEM
FINISH

ASSEMBLY
NODEWISE P-STRESSP1
LS1
AVERAGED NODAL VALUES
VALUES WERE CALCULATED

CURRENT MENU
DATA
EYE
HELP
FINISH
INDEX
OPTIONS
PRESENT
RESULTS
VIEW



t1 = 25mm
t2 = 37.5mm
od = 1000mm
trans ratio = 4:1
Max Principal Stress

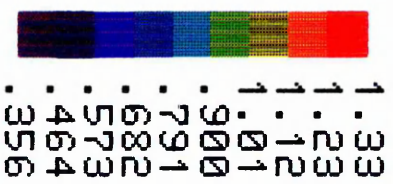


fig 3.20

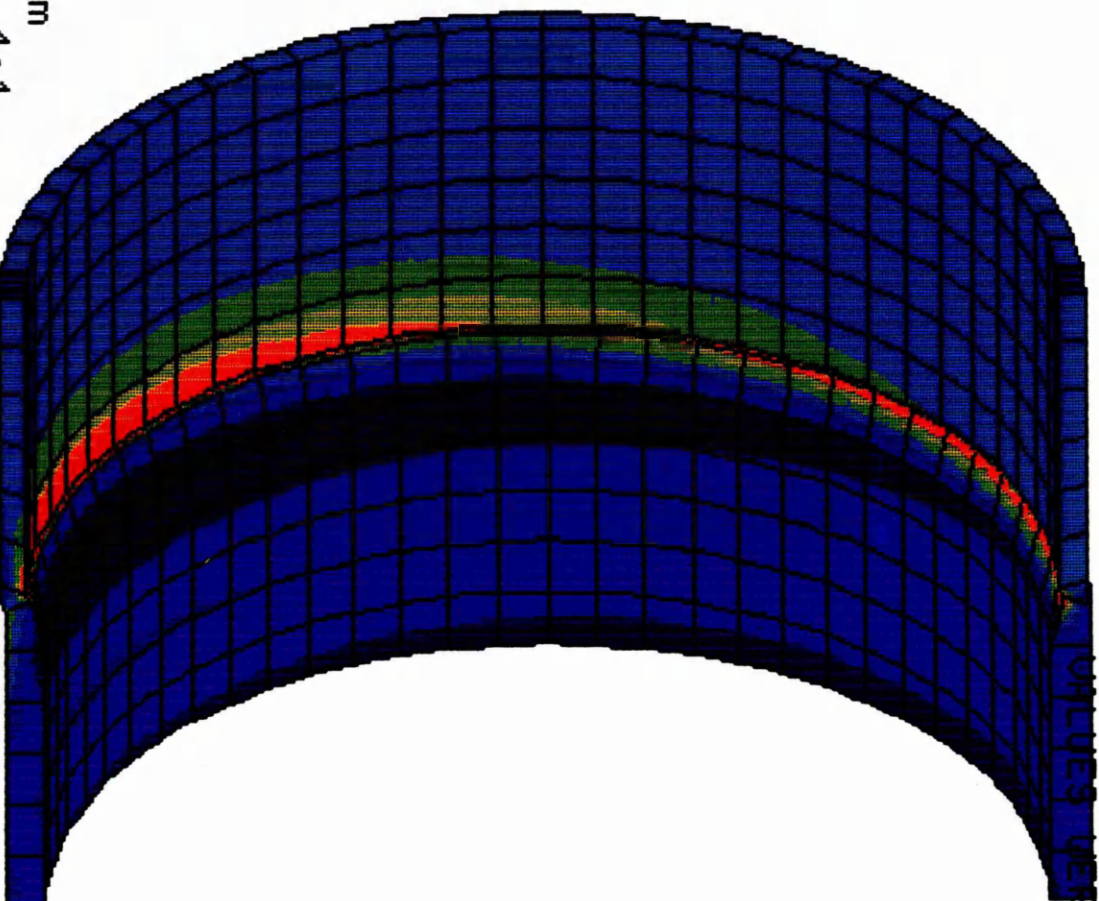
SESAM

POSTFEM

FINISH

ASSEMBLY P-STRESSP1
NODEWISE LS1
AVERAGED NODAL VALUES
VALUES WERE CALCULATED

CURTAINING
DATA
EYE
FINISH
HELP
INDEX
OPTIONS
PRESENT
RESULTS
VIEW



t1 = 25mm
t2 = 37.5mm
od = 1000mm
offset = 5.0mm
trans ratio = 4:1
Max Principal Stress

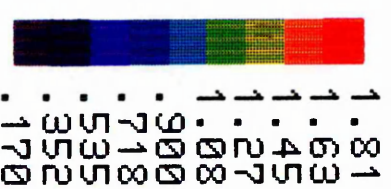
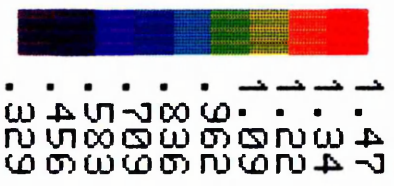
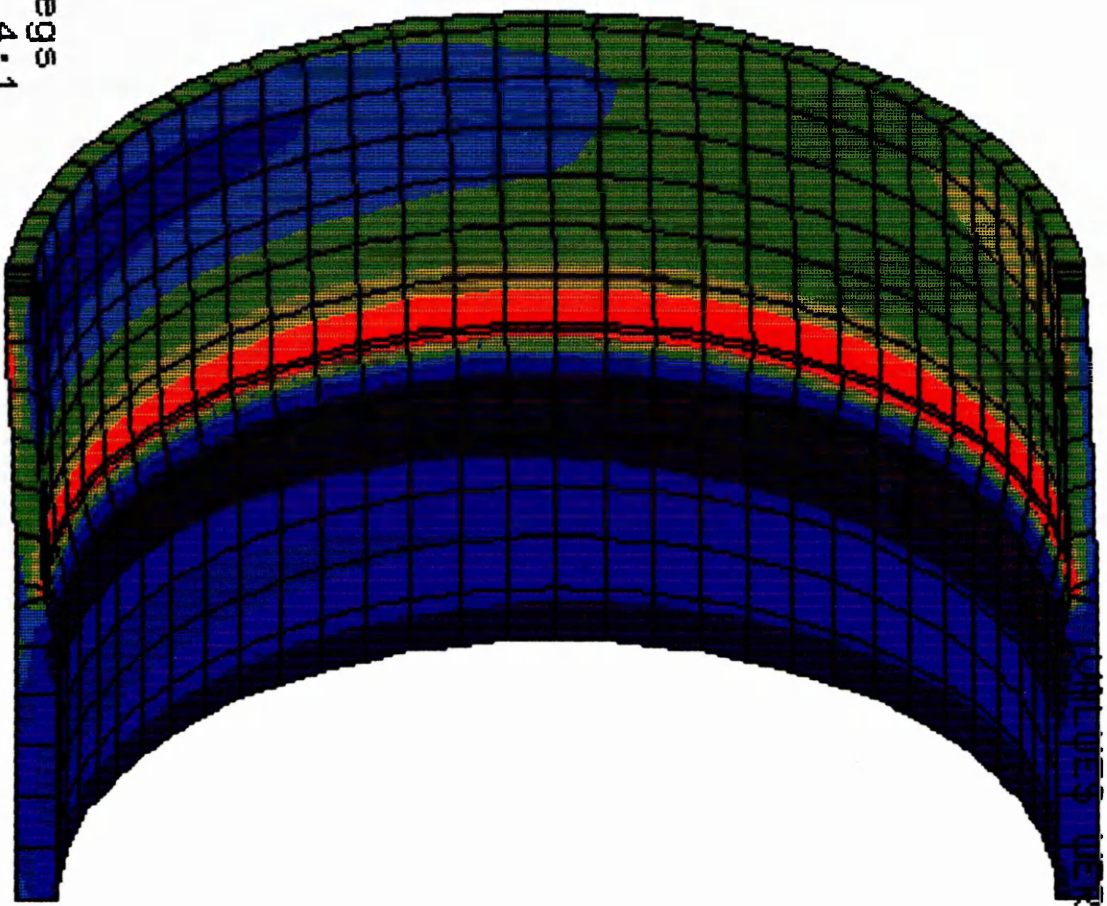


fig 3.21

SESAM
POSTFEM
FINISH

ASSEMBLY
NODEWISE P-STRESSP1
LS1
AVERAGED NODAL VALUES
ELEMENTS WERE CALCULATED



t1 = 25mm
t2 = 37.5mm
od = 1000mm
misal = 2.0 degs
trans ratio = 4:1
Max Principal Stress

fig 3.22

QUITTING
DATA
EYE
FINISH
HELP
INDEX
OPTIONS
PRESENT
RESULTS
VIEW

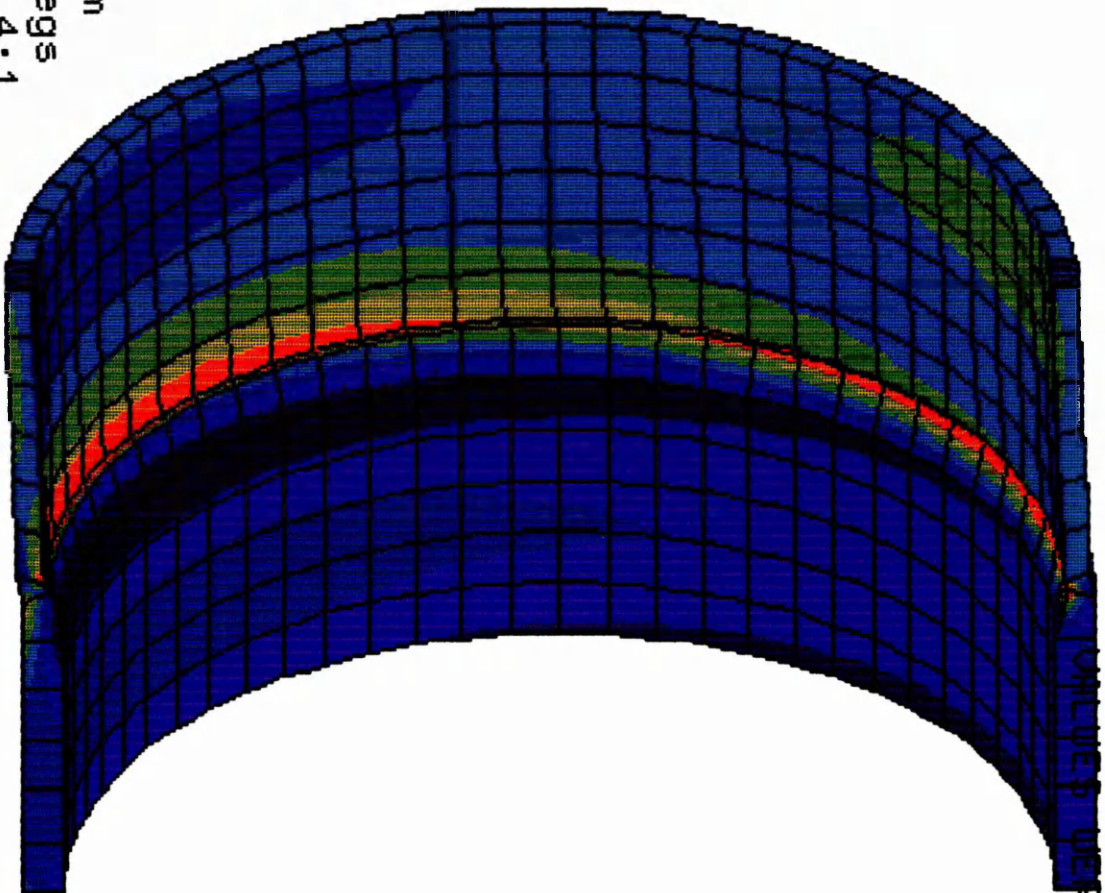
SESAM

POSTFEM



FINISH

ASSEMBLY
NODEWISE P-STRESSP1
LS1
AVERAGED NODAL VALUES
VALUES WERE CALCULATED



t1 = 25mm
t2 = 37.5mm
od = 1000mm
offset = 5.0mm
misal = 2.0 degs
trans ratio = 4:1
Max Principal Stress

fig 3.23



CURTAINING
DATA
EYE
FINISH
HELP
INDEX
OPTIONS
PRESENT
RESULTS
VIEW

4.0 DISCUSSION AND CONCLUSIONS TO SECTION A

4.1 Discussion

A number of assumptions had to be made regarding the behaviour of the coupons and loading frame in the TWI 2-D experimental programme. Ultimately, it proved possible to derive a set of boundary condition which equated to the observed results. It would, however, have been valid to merely model the full applied loads and resultant displacements. To do this would have required that, in addition to extensive strain gauging, full measurements be taken of all displacements and deformations of the model. Unfortunately, the bulk of this phase of the experimental programme was completed prior to the decision to attempt to replicate it using FE techniques.

The values of offsets and misalignments used by TWI cover the full range likely to occur in offshore structures (ref 9). While the 2-D equations were found to agree with the FE results within this it should be noted that the results, particularly misalignments, are very sensitive, to movement outwith this range. The possible implications of this trend should not be relevant to offshore structures designed to the specifications of an appropriate code but care must be taken if these results are to be used outwith the offshore industry in an area where the design codes are less rigorous.

While the results obtained do not allow for the quantification of the effect of the transition ratio on the SCF, it is clear that the effect of this parameter tails off exponentially as the transition ratio increases. The results obtained suggest that any transition ratio above 4:1 will have a negligible effect on the SCF. This equates well with the true situation found in offshore structures where transition ratios are typically of the order of 3 or 4:1.

In general, the agreement between the 2-D and 3-D results was not outstanding. It was better for offsets than for misalignments although this is to be expected as the equations used for offset allow for the change in material thickness. There still exists the problem of predicting accurate boundary conditions for a 2-D representation of a slice through a 3-D model. The work carried out using the three boundary conditions (BC1, BC2 & BC3)

served to highlight how sensitive the results are to variations in boundary conditions.

The values of SCFs found throughout this programme were mostly below 3.0. This value is low compared to the values often found at nodes and implies that fatigue cracking at these butt joints should be less of a problem than at nodes. In addition this value can be kept low by designing so as to minimise the effect of parameters such as transition ratio etc.

4.2 Conclusions

Where comparisons of FE and experimental results are to be carried out the experiment must be designed with a view to the quality and quantity of detailed information required by the FE analyst.

The 2-D equations are found to agree with the FE results within the range of offset and misalignment typically found in offshore structures.

The transition ratio should be above 4:1 to ensure that it has a negligible effect on the SCF.

The level of agreement between 2-D and 3-D results is not particularly good. It is, however, better for offsets than for misalignments.

The values of SCFs found in this programme are mostly below 3.0. This value is low compared to the values often found at nodes and implies that fatigue cracking at these butt joints should be less of a problem than at nodes.

SECTION B: FAILURE IN TUBULAR WELDED JOINTS

5.0 Introduction

5.1 The Problem

Large, complex structures such as are found in the offshore oil industry, have a viable working life typically measured in decades. In many cases these structures are now well into their designed working lives. With the extensive use of tubular welded joints in such structures, there is an ongoing need for work to determine the continued reliability of these joints. This involves the accurate assessment of the effect of discontinuities which may realistically exist around welds and the validation of advanced computational fracture mechanics techniques used to analyse these problems.

5.2 Previous Work

Much work (eg ref 10) has been done on experimental studies of cracked joints but analytic mathematical expressions for fracture mechanics parameters are only available for relatively simple geometries (ref 11). For complex structural configurations, these must be determined by computational techniques such as finite element (FE) analysis, on the basis of the actual stress field near the crack tip.

The modelling of simple crack geometries using finite elements will allow the technique to be cross-referenced against accepted 2-D and 3-D solutions for cracks. However, while these solutions provide a validation of the use of finite elements their range of applicability is limited especially when the crack exists in a complex stress field such as is found in tubular joints.

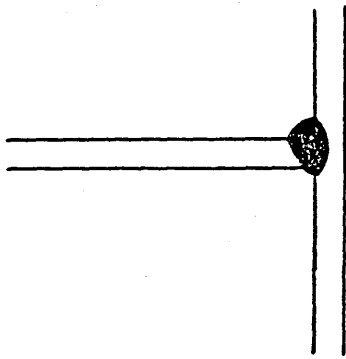
Hancock and Du (ref 12) have modelled a cracked T-joint using linesprings and shell elements and compared their analysis with a full 3-D model using a mesh produced by the author (ref 13). Good agreement is

reported between the two techniques for long deep cracks and, since linesprings contain no information of the local geometry of the weld, it is inferred that for such cracks the weld profile is relatively unimportant. Conversely, poor agreement is reported between the linesprings and the 3-D analysis for short, shallow cracks. This is attributed to the greater influence of the weld profile on short cracks. Finally, while agreement between the linespring result and an experimental result of Dover is noted, this is felt to be fortuitous.

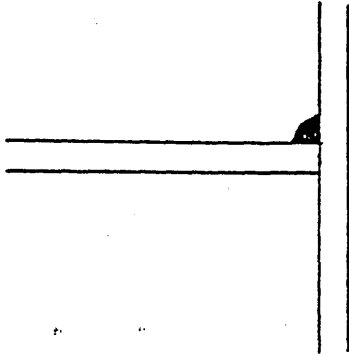
The ability of linesprings to only model mature cracks gives cause for concern: for by then the defect may be beyond economic repair. Welded defects in tubular joints spend their early life spreading circumferentially around the joint rather than moving deeper into it and so the crack tip spends much of its life in a stress field which is influenced by the weld profile and thus is not amenable to linespring analysis. Hence, for practical purposes, a full 3-D analysis may be the only possible solution. In the current work, such analyses have been performed and compared directly with results (ref 10) from a full scale experiment done by Dover and co-workers.



(a) Buttt Weld



(b) T-Buttt Weld



(c) Fillet Weld

fig 5.1 Types of welded joints

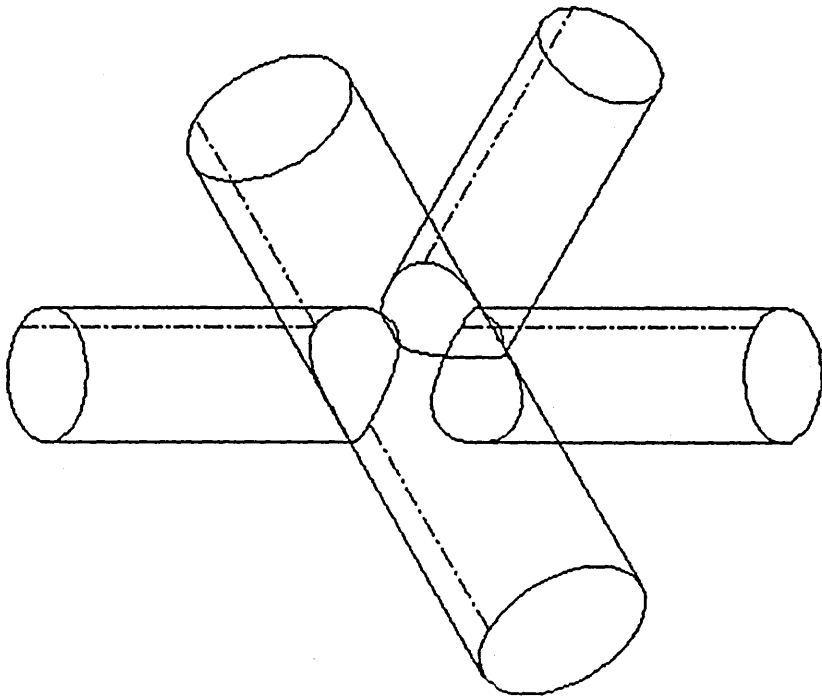


fig 5.2 Example of a complex node

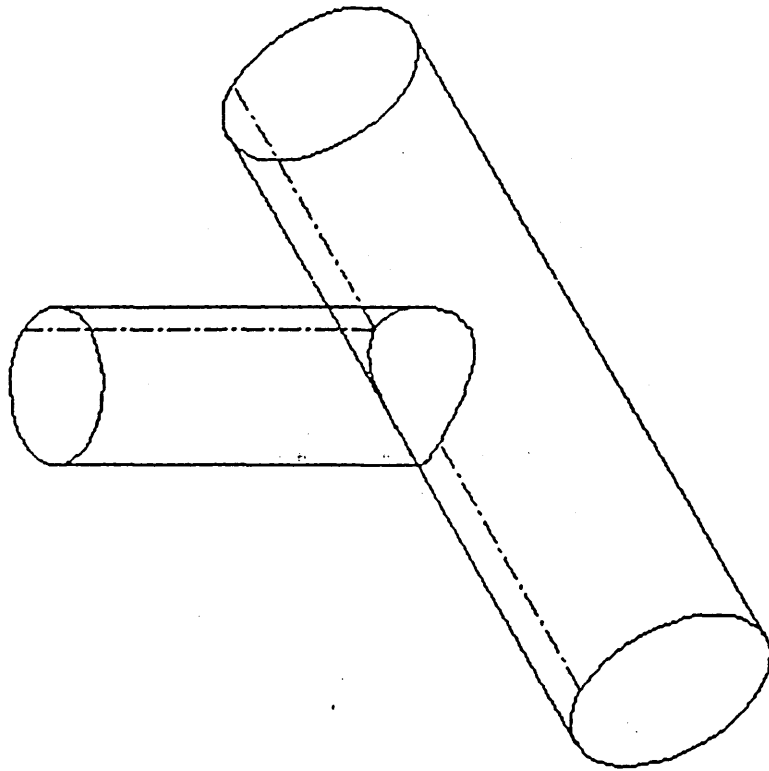


fig 5.3 Example of a simple T-Joint

6.0 COMPUTATIONAL FRACTURE MECHANICS

Fracture mechanics started with the paradox that while any crack in a brittle material should cause immediate failure, since infinite stresses should occur at the infinitesimal crack-tip radius, real structures survive in the presence of numerous and substantial cracks. The reason is that any process, cracking included, requires both a mechanism and an energy supply. High stresses provide the mechanism but the energy required to drive a crack through a body usually comes from the elastic strain energy released as the flanking material relaxes (fig 6.1). The advance of a small crack releases less energy than that of a large crack and it is apparent that there is a critical size of crack corresponding to a *critical strain energy release rate*, or *crack driving force* G_c , below which the crack is stable.

6.1 Crack Driving Force

Any complex 3-D crack displacement field can be decomposed into a summation of three components, known as Modes I, II and III, as shown in fig 6.2 but in many practical problems, the effect of Mode I (opening mode) is predominant. The "crack driving force" or Strain Energy Release Rate (refs 14, 15 & 16) is then expressible as:

$$G = \lim_{\Delta A \rightarrow 0} \frac{1}{\Delta A} \int_a^b \sigma \, du \, dA \quad [6.1]$$

In general, G is not easy to calculate and *linear elastic fracture mechanics* (LEFM) attempts to simplify the problem by ignoring the inelastic behaviour at the crack tip and modelling the material as purely linear elastic.

6.2 Stress Intensity Factor

For a linear elastic material subjected to remote tensile loading and

containing a crack in a semi-infinite body as shown in fig 6.3 there is a singularity associated with each of the three fracture modes (ref 17). Since this singularity exists at the tip of any sharp crack, K_T cannot be used to distinguish different crack geometries. However the stresses at a distance r directly ahead of a crack can be written as a power series in the form:

$$\sigma_{ij} = K/\sqrt{2\pi r} + \text{additional terms} \quad [6.2]$$

where the additional terms vanish asymptotically near the crack tip. The *stress intensity factor* K is different for each configuration and so can be used to distinguish different crack geometries. K indicates, not so much the crack tip σ_{ij} itself but more the degree of infinity reached by σ_{ij} . Notice that in moving towards the crack tip, σ_{ij} approaches ∞ at the rate of $r^{-1/2}$. This so-called " $r^{-1/2}$ singularity" is characteristic of LEFM.

For cracks of finite depth, K has the more general form:

$$K = Y\sigma_{\infty}\sqrt{\pi a} \quad [6.3]$$

where a is the crack depth and Y depends on the geometry of the structure.

In real materials the crack tip stress is limited by local yielding to σ_y . However, in many cases the plastic zone is small enough for linear elastic theory to give reasonable values for σ_{ij} except near the crack tip (as noted by Ritchie, K is most accurate where it is least applicable). With this *small-scale yielding*, the stress field is said to be *K-dominated* and in such stress fields, crack advance occurs at a critical value K_c . Under plane strain conditions $K_c = K_{1c}$, which is a material constant known as the *fracture toughness*.

6.3 Computation of K

The accuracy of the solution for K will depend on the ability of the stress field near the crack tip to model the $r^{-1/2}$ singularity. This can be achieved with eight noded isoparametric elements by moving the midside nodes to the quarter points and collapsing one side to a point. This has the effect of distorting the interpolation functions into a shape which produces the appropriate stress singularity. The resulting triangular shapes are focussed at

the crack tip, as in fig 6.4, and K_I is calculated from the quarter point displacements (fig 6.5) as:

$$\begin{aligned}
 K_I = \frac{E}{4(1-\nu^2)} \sqrt{\left(\frac{\pi}{2L_1}\right)} & [2v_B - v_C - 2v_E - v_F + v_D - 2v_{B'} + v_{C'} - 2v_{E'} + v_{F'} - v_{D'} \\
 & + \frac{1}{2}\eta(-4v_B + v_C + 4v_E - v_F + 4v_{B'} - v_{C'} - 4v_{E'} + v_{F'}) \\
 & + \frac{1}{2}\eta^2(v_F + v_{C'} - 2v_{D'} - v_{F'} - v_{C'} + 2v_{D'})] \quad [6.4]
 \end{aligned}$$

in which v is the nodal displacement and the subscript identifies the node as shown in fig 6.5. Similar expressions are available for K_{II} and K_{III} . This system has the advantage of allowing the three values of K to be calculated separately and their relative importance found for the crack in question. This *direct method* for calculating K has however been largely superseded by alternative techniques.

6.4 Virtual Crack Extension

For K -dominated plane strain fields:

$$K = \sqrt{[(EG)/(1 - \nu^2)]} \quad [6.5]$$

$$\Rightarrow G = K^2/E' \quad [6.6]$$

where:

$$E' = E/(1 - \nu^2) \quad [6.7]$$

and K can be inferred from G , as determined from the difference in the strain energy of the same body with two slightly different crack lengths. This is inconvenient and costly and since the remote elements are largely unaffected by small changes in crack length, a good approximation to G is obtained by displacing the crack tip node slightly and only calculating the change in the energy of elements near the crack tip. In fact the effect which such a *virtual crack extension* would have on the local elements can be predicted by variational methods without the need to actually move the node and hence without the need to perform the analysis twice.

The method was developed by Parks (refs 18 & 19) and starts by noting that, as in fig 6.6, the crack driving force G in a 3-D body is a function of the location s along the crack front. Thus (ref 14):

$$G = G(s) \quad [6.8]$$

Hence if the crack front extends as shown in fig 6.6 the virtual work principle predicts that:

$$\int_{\delta A} G(s) \delta a(s) ds = -\delta \pi \quad [6.9]$$

where $\delta \pi$ is the change of the total potential energy. In the FE analysis, $\delta \pi$ is summed for each element near the crack tip. If the crack front is perturbed $\delta \pi$ will alter allowing a reasonably accurate calculation of G . This is based on the change of stiffness of the elements adjacent to the crack tip.

This technique, also known as the Stiffness Derivative Method for linear elastic materials, can be extended (ref 20) to non-linear analysis by replacing G with J (the J-Integral defined below).

6.5 Linesprings

A plate containing a part-through crack has locally increased compliance normal to the plane of the crack (fig 6.7). Furthermore, the remaining ligament at the crack lies to one side of the loading axis and so the plate experiences a moment along the line of the crack. These effects can be modelled by superposing equivalent linear and rotational compliances onto an uncracked plate as in *linespring* elements which thus allow for example, an elliptical crack in a plate to be modelled by a mesh of thick shells rather than by expensive solid elements.

Linesprings do have drawbacks. Firstly, they are in practice restricted to LEFM rather than the more general EPFM discussed later. Secondly, they assume plane strain and are inaccurate near the surface breaking ends of elliptical cracks where this assumption is invalidated by the proximity of a

free surface. This creates problems if bending is important since bending stresses are greatest at the outer surfaces where linesprings are known to be inaccurate. Further, recent work (ref 12) suggests that the inability of shell elements to accurately replicate weld profiles seriously degrades the results for shallow weld toe cracks where these effects are most pronounced. While linespring calculations have a role, there remains a requirement for a full 3-D local analysis of the discontinuity although this may be embedded in shell elements to minimize cost and time.

6.6 EPFM

LEFM assumes only small-scale yielding and K is meaningless in the presence of more widespread plasticity. However, in such cases, crack advance can be shown to occur at a critical value J_c of the nonlinear strain energy release rate J for an elastic material whose stress-strain law follows an identical curve to the elastic/plastic material (refs 21 & 22). This is the basis of *elastic-plastic fracture mechanics* (EPFM). J is best calculated by integrating round a contour surrounding the crack tip and is thus called the J -integral. It can be shown that the value of J is independent of the choice of contour, which can thus be selected to suit the analyst.

Strictly, J is inapplicable if the material unloads, as it does when a crack advances to leave a *plastic wake* but, theoretical objections notwithstanding, the J -integral has shown itself to be useful in practice.

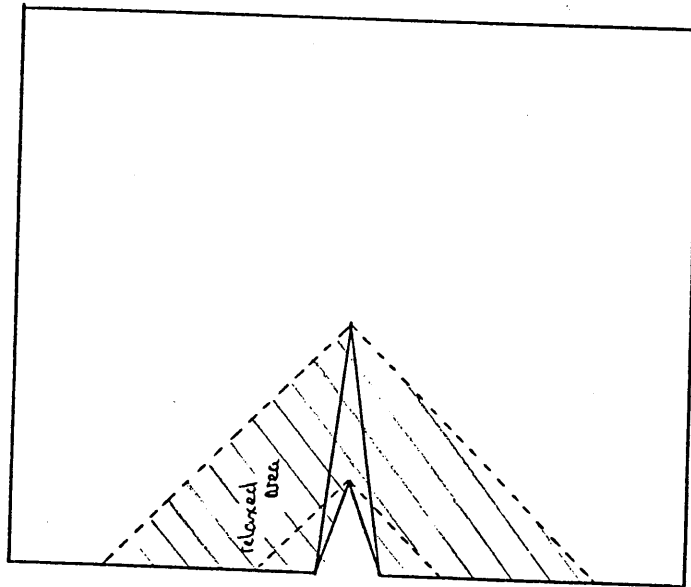
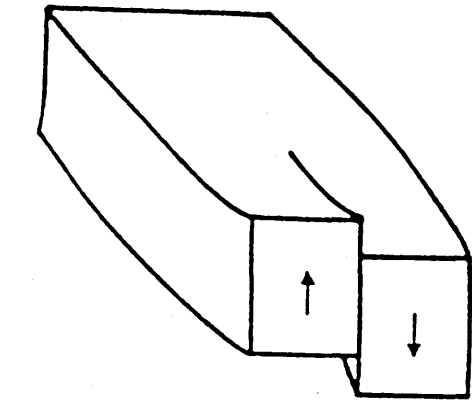
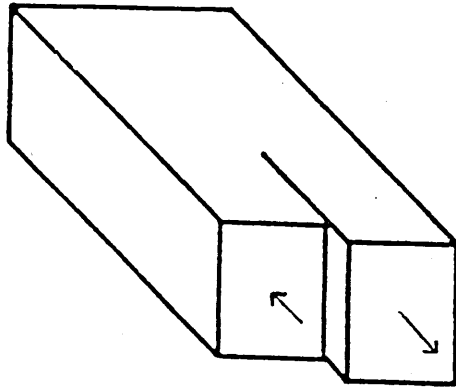


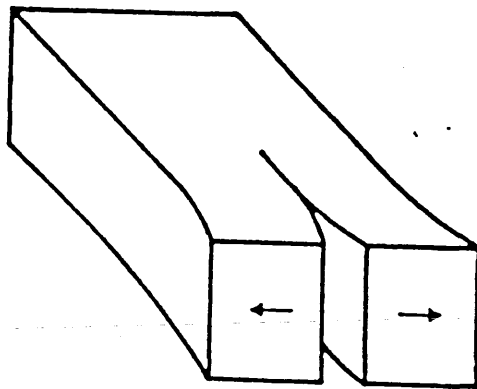
fig 6.1 Strain energy release



(c) Mode III



(b) Mode II



(a) Mode I

fig 6.2 Modes of fracture

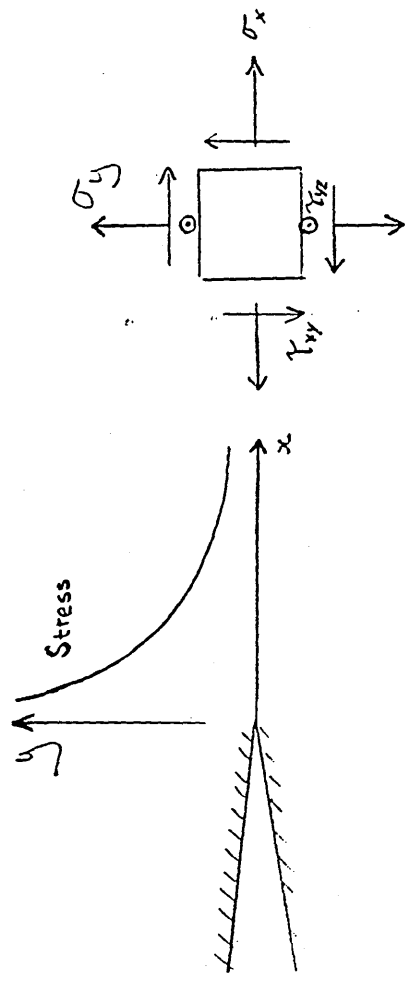


fig 6.3 Stress state near a crack tip

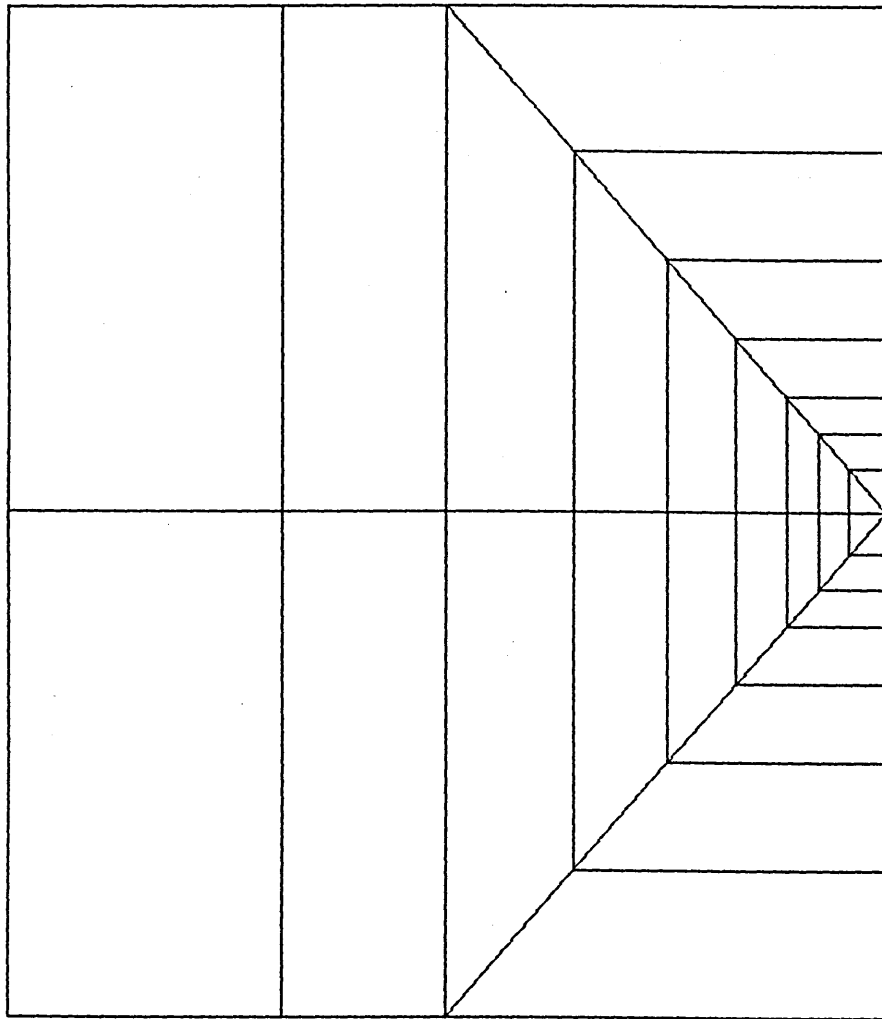


fig 6.4 Mesh for 2-D plane strain model

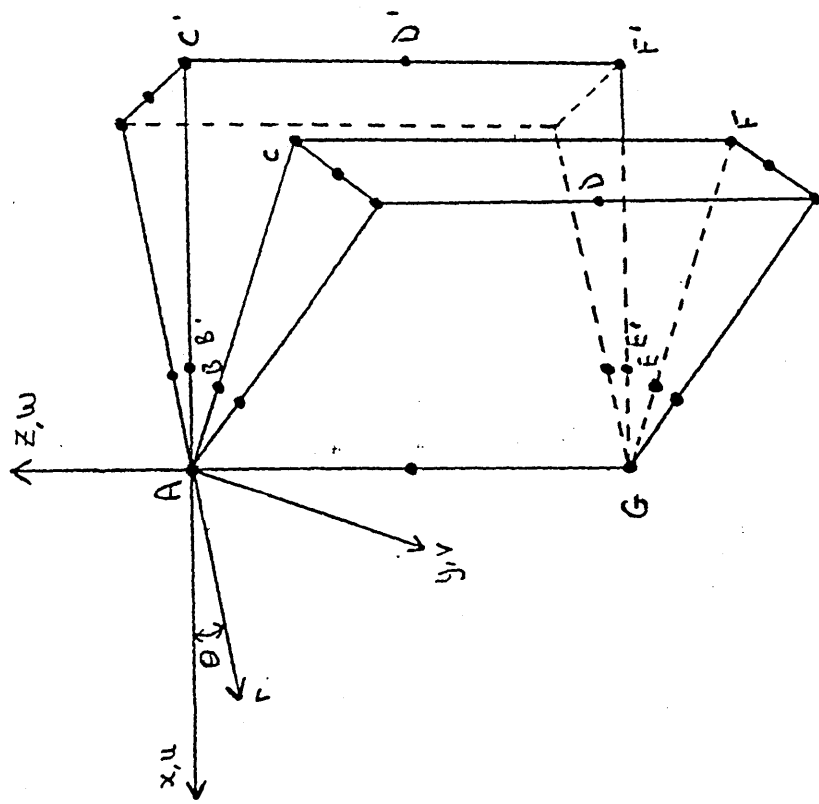
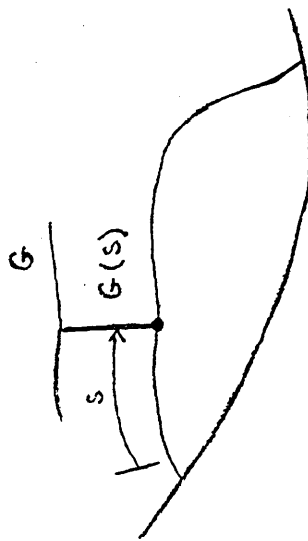
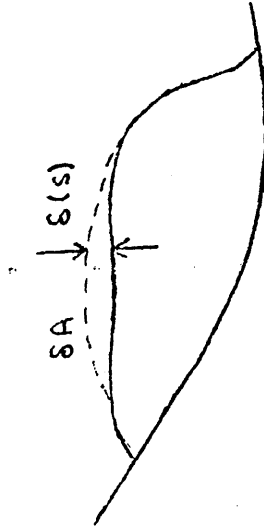


fig 6.5 K from 1/4 point nodal displacements

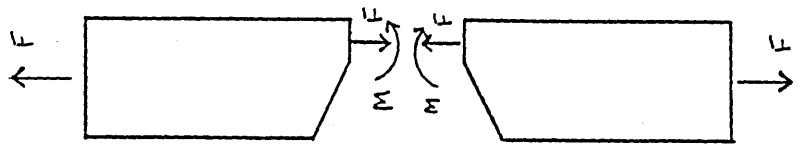


(a) Crack driving force as a function of s

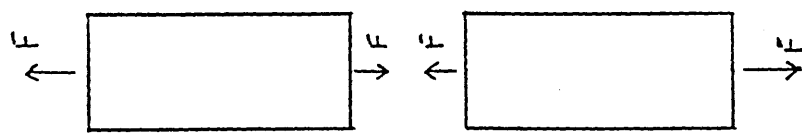


(b) Perturbation of a crack front

fig 6.6 Virtual crack extension



(a) Un-cracked case



(b) Cracked Case

fig 6.7 Linesprings

7.0 PLANE STRAIN ANALYSIS

As a first step towards a full 3-D analysis of a tubular joint, a very simple configuration, comprising a plane strain crack in a plate of finite width, was subjected to an FE analysis. Such a simple analysis is easily benchmarked against well-known analytic solutions (ref 14) but provides guidance in the design of a suitable mesh for the more complex configurations to be addressed later.

7.1 Theoretical Solution

For a mode I edge crack in a finite width strip as in fig 7.1:

$$K_I = Y \sigma \sqrt{\pi a} \quad [7.1]$$

For $a/W = 0.5$ and $h/W = 1$:

$$Y = 2.83 \quad [7.2]$$

and thus:

$$K = 2.83 \sigma \sqrt{\pi a} \quad [7.3]$$

Furthermore, for an LEFM solution:

$$J = G = K^2/E' \quad [7.4]$$

where:

$$E' = E/(1 - \nu^2). \quad [7.5]$$

7.2 FE Modelling

The eight noded plane strain isoparametric elements required to model this configuration were not available in SESAM and the work was carried out using FEMVIEW and ABAQUS. To force the quadratic interpolation functions of

these elements into a configuration which accurately models the $r^{-\frac{1}{2}}$ singularity at the crack tip, the mesh was focussed onto the crack tip, with the midside nodes in the focal elements moved to the quarter point position, as in figs 7.2a and 7.2b. Since the physical problem is symmetric, only a half of this was meshed, with appropriate boundary conditions assigned on the plane of symmetry.

Linear elastic isotropic material properties were assigned to the elements, with the values $E = 210$ GPa and $\nu = 0.3$ chosen to agree with those for typical offshore structural steels.

7.3 Results

Within the plane strain configuration, several variations on the element size and adjacent element aspect ratio (defined here as the ratio between the corresponding sides of adjacent elements) were processed. ABAQUS produces values for J rather than K_I and in general, it was found that the J measured around several concentric contours gave consistent results provided the contours were away from both the crack tip and back plane of the ligament (fig 7.3). It was noted however that, although consistent results were obtained for a number of different adjacent element aspect ratios between 1:1 and 2:1, this was not so if the aspect ratio was allowed to change between contours (fig 7.4).

The immediate area of the crack-tip is best modelled by the use of degenerate quadrilaterals in which one side has zero length. Such zero length lines may be defined either via coincident nodes or by citing the same node twice in the element definition (fig 7.5). In the latter case, only two degrees of freedom are retained at the crack tip, as is strictly required in an LEFM solution. In the former case, the crack tip has 18 degrees of freedom, and is, in theory, capable of opening as required for an EPFM solution. In practice, it was found that the difference in solutions due to this factor, in a linear elastic analysis, was as low as 1% in the two most widely differing results and generally of the order of $\frac{1}{2}$ % (fig 7.6). This lack of a significant difference is fortunate, in that many FE codes will not allow either coincident nodes or duplication of nodes within the element definition.

7.4 Conclusion

Finite Element techniques provide an accurate method of assessing K for a crack. While the results obtained are not affected by variations in mesh geometry care should be taken to ensure that regular, reasonably shaped elements are used.

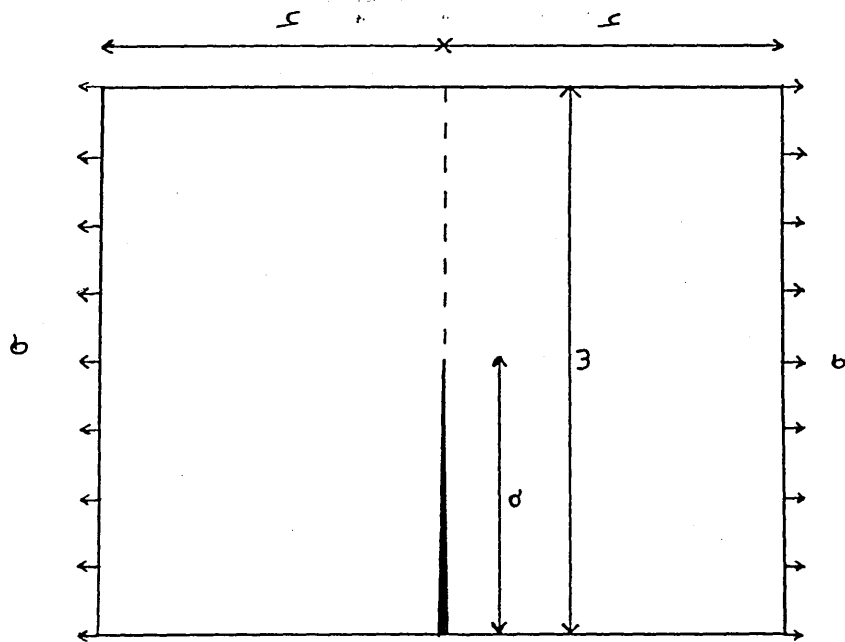
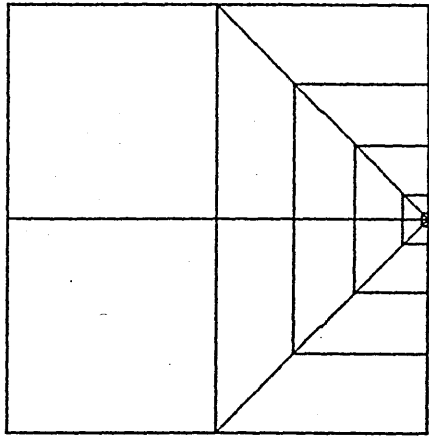
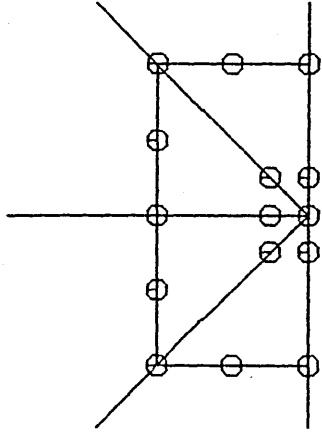


fig 7.1. Edge crack in a finite width strip



(a) Plane strain focussed mesh



(b) Crack tip nodes (see fig 7.5)

fig 7.2 Meshing for 2-D plane strain model

$$\frac{JE}{\sigma^2 a(1-v^2)}$$

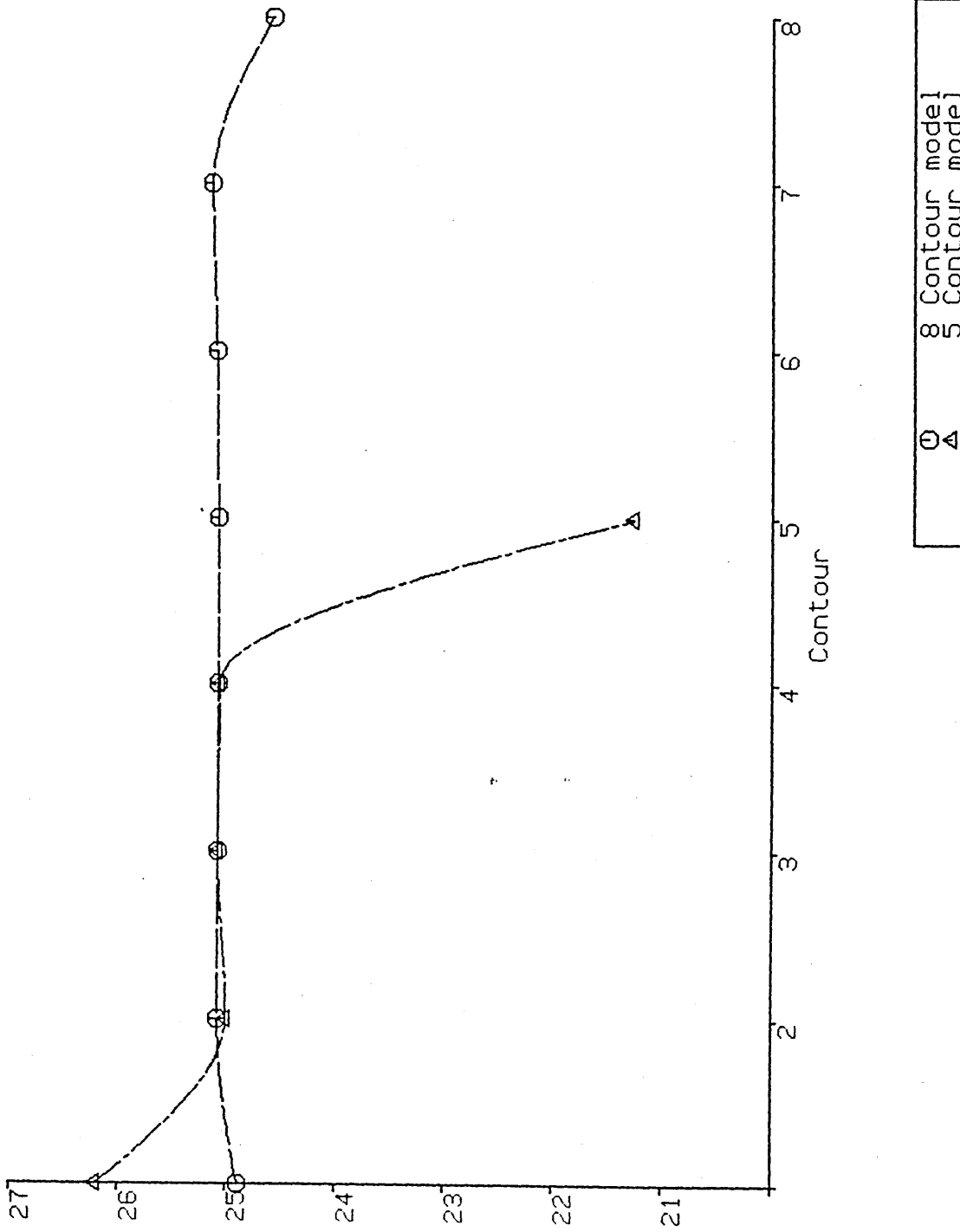


fig 7.3 J-Integral values for different contours

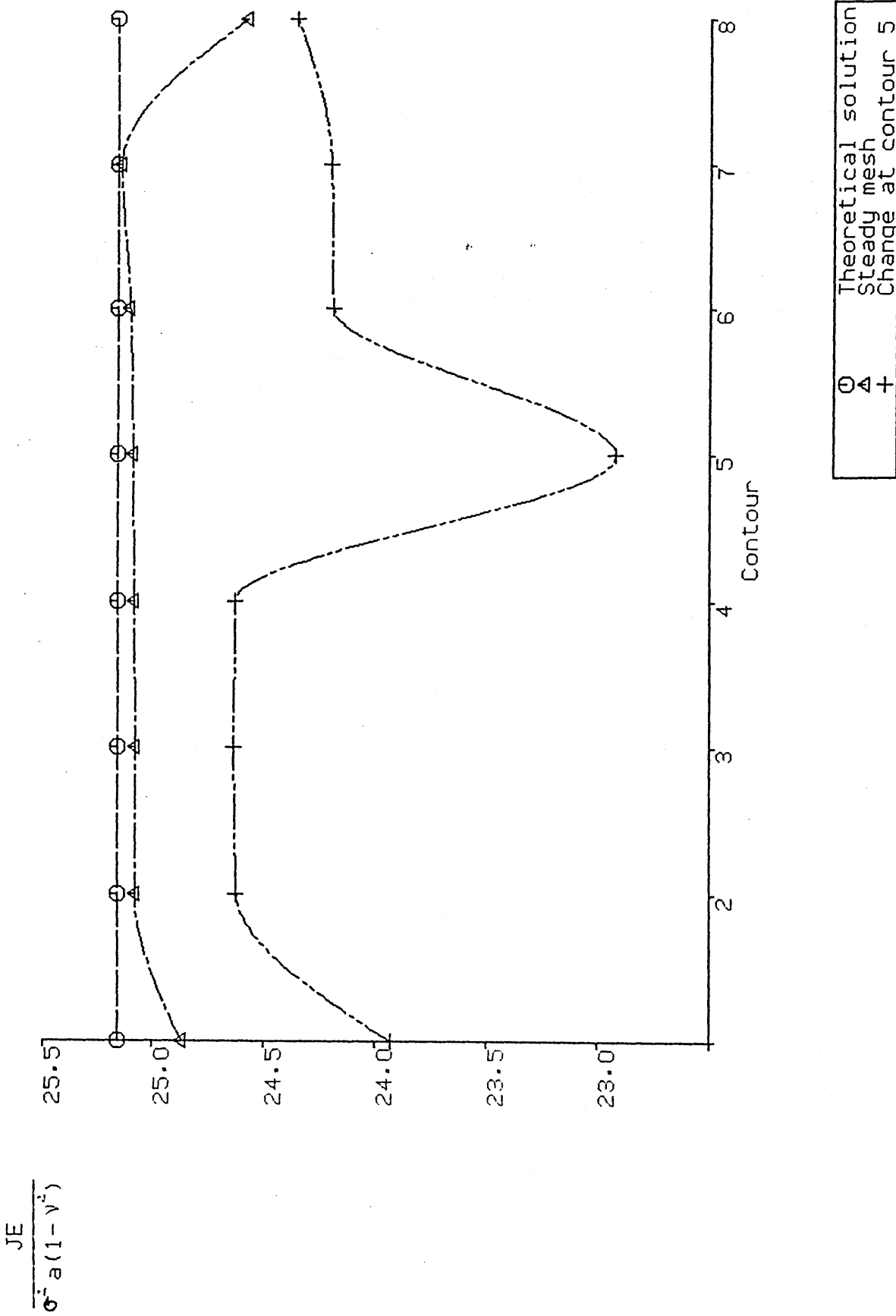
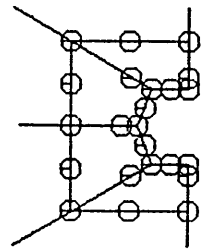
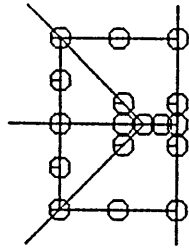


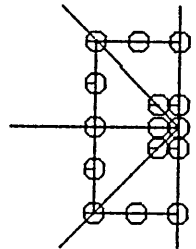
fig 7.4 Effect of change of aspect ratios on computed J-Integral values



13 DOF



10 DOF



2 DOF

fig 7.5 Different formats used to define crack tip node clusters

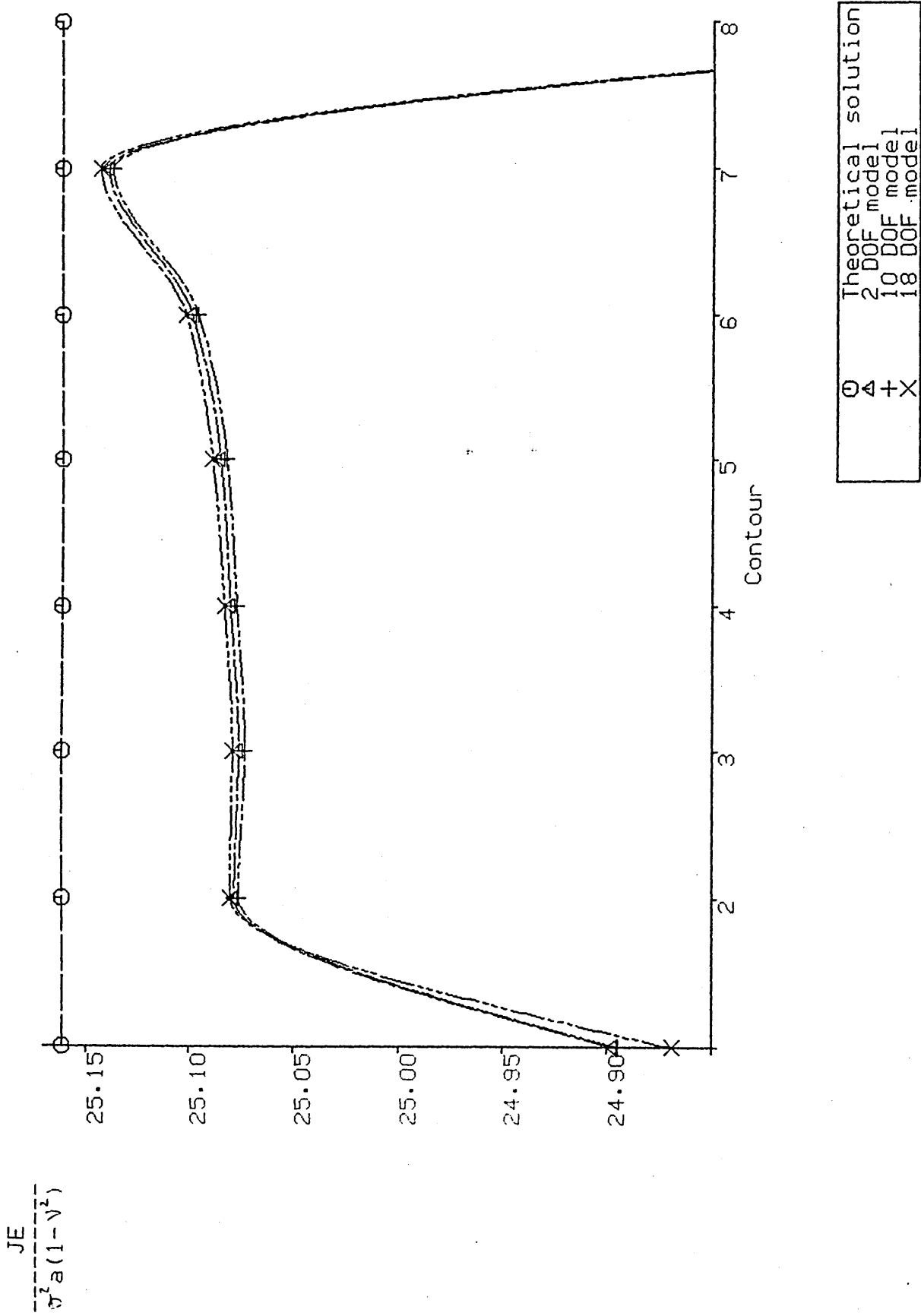


fig 7.6 Effect of varying the number of DOFs at the crack front

8.0 3-D ANALYSIS OF STRAIGHT CRACK FRONT

8.1 Analytic Solution

In order to extend the validity of the results given in section 7.3, the plane strain problem was reproduced in 3-space as a straight crack front in a 3-D brick. The analytic solution for this is as before (section 7.1).

8.2 FE Modelling

The mesh shown in fig 7.2a was projected into three dimensions (fig 8.1) with varying numbers of elements throughout the depth. Clearly, the difference in the dimensions of some of the elements shown in fig 7.2a will result in considerable distortion of the 3-D solid elements from their parent shape. A mesh was therefore created which varied the size of the elements through the thickness of the whole brick to allow the any effect on accuracy to be observed. This was repeated for a variety of elements through the depth. Fig 8.2 shows the mesh for a three element deep model in which the problem of the aspect ratios can be clearly seen.

Again, the package chosen was ABAQUS but the larger models in this series contained more than 6000 DOFs and were beyond the capabilities of the local VAX 11/750. These models were analysed on the UMRCC Cyber 205 but restriction on the maximum CPU time available on this machine prevented the largest of the models from being completed.

8.3 Results

Neither the distortion nor the aspect ratio between adjacent elements was found to have a significant effect on the results obtained and, while the deterioration in results at the boundaries of the body is still apparent (fig 8.3), the computed J values agreed well with the plane strain analytic solutions (fig 8.4).

8.4 Conclusions

For linear elastic analyses, using a carefully defined mesh, good agreement can be obtained between the FE results and the analytic results for simple cases. Relatively small variations in the computed values of J were obtained from fairly significant changes in the mesh. This stability in the results gives some confidence that 3-D analysis will not be oversensitive to the fine details of the mesh geometry.

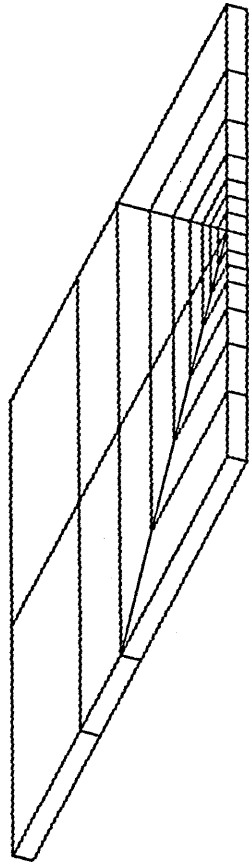


fig 8.1
3-D focussed mesh containing straight crack

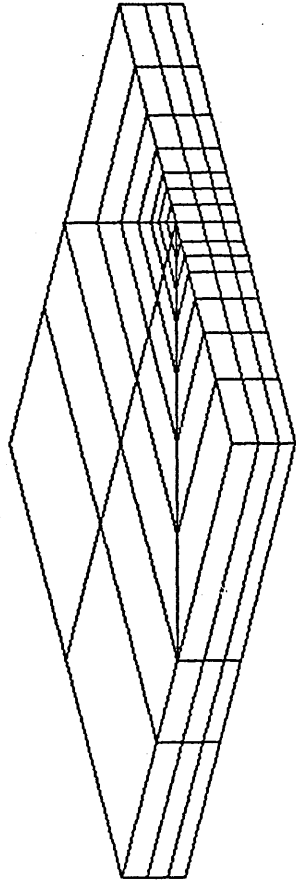


fig 8.2 Variation of element aspect ratio for fig 7.2a

$$\frac{JE}{\sigma^2 a(1-\nu^2)}$$

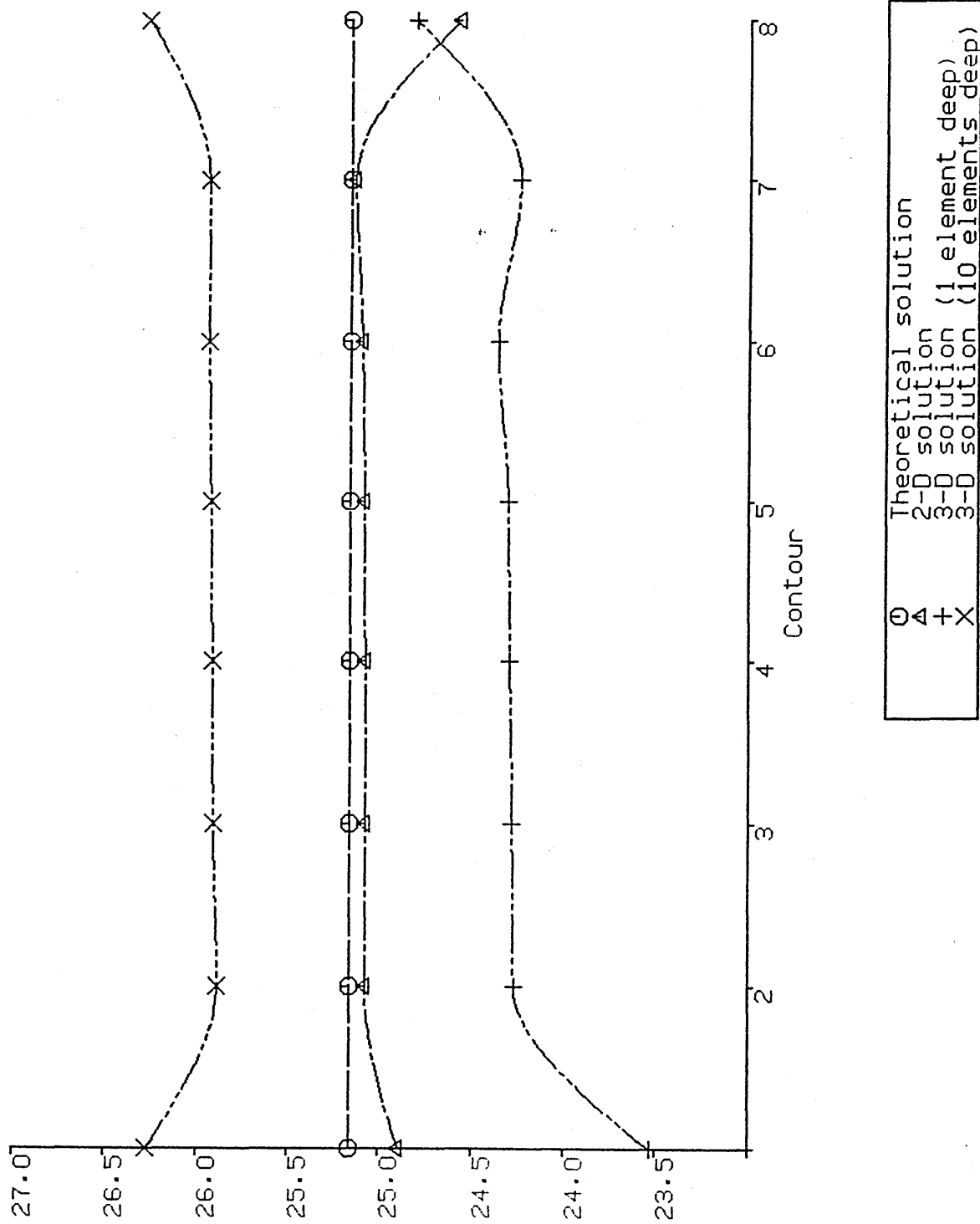


fig 8.3 Comparison of theoretical, 2-D and averaged 3-D solutions

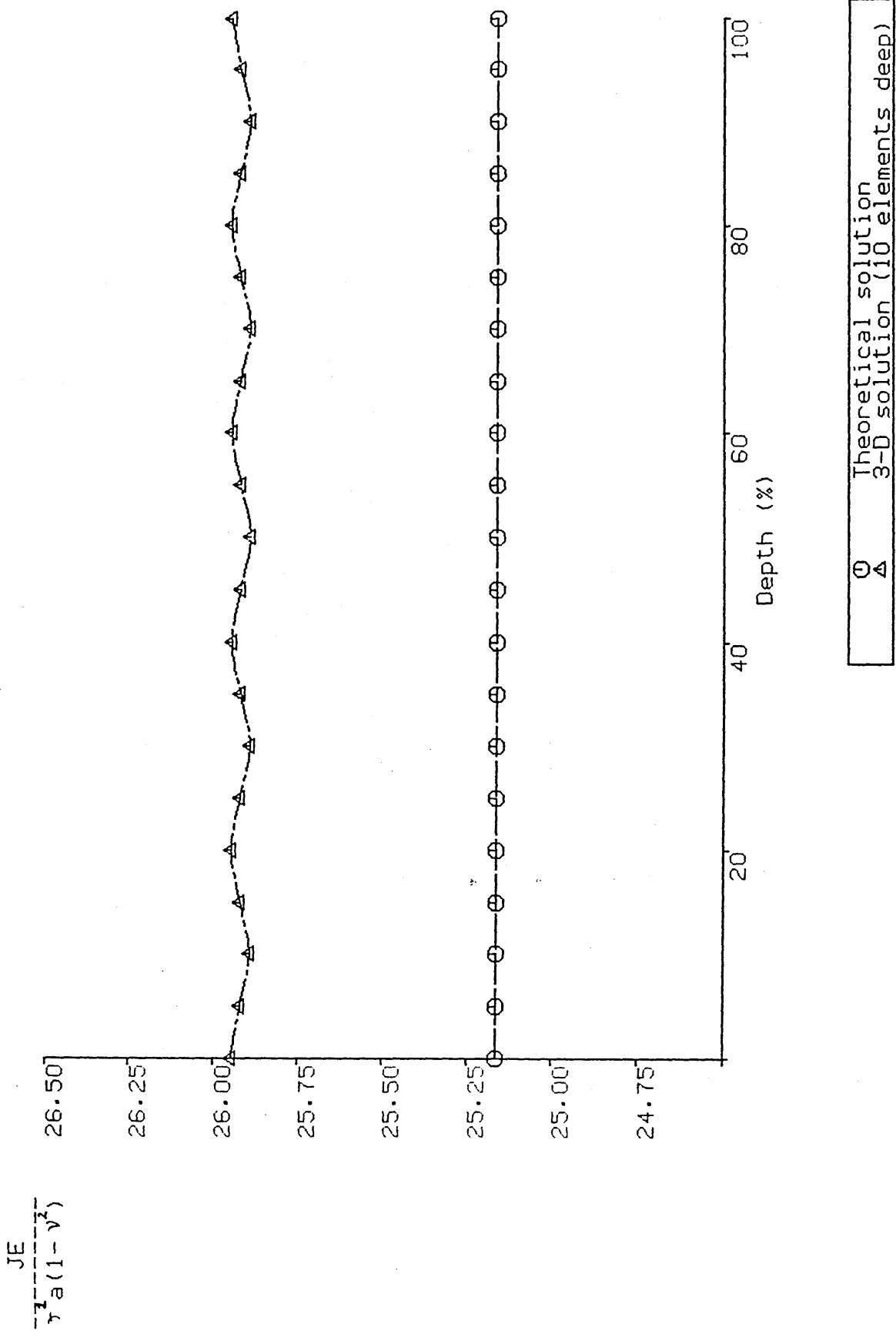


fig 8.4 Variation of results through depth of solid model

9.0 TUBULAR JOINT ANALYSES

9.1 Modelling

Meshing a tubular T-joint in 3-D space presents several serious problems to the engineer. While the chord and brace are geometrically simple and easily meshed with shell elements, reproducing the geometry of their doubly curved intersection with solid elements is a non-trivial problem, further compounded by the inclusion of a crack-like defect around the weld toe. Fig 9.1 shows a 3-D mesh containing an elliptical crack, developed from the mesh shown at fig 7.2a. This was generated using FEMGEN and despite the power of the package in the hands of an experienced analyst, a number of evident faults proved intractable. Firstly, the need to map patches of solid elements around the complex geometry of the crack, without transition zones, produces poor quality elements with high aspect ratios and unacceptable included angles. Secondly, the need for different numbers of elements across the length and breadth of the outer boundary makes substructuring difficult. Finally, mapping the block of elements in fig 9.1 onto the intersection of the chord and brace is tedious.

These problems were overcome with the release of the TUJAP suite, a subset of SESAM from Veritec. This contains PRETUBE, a specialised preprocessor which greatly facilitates meshing tubular intersections containing defects.

All of the 3-D joint meshes were generated using PRETUBE. This models the T-joint using a hierarchy of superelements, whose replication allows the complete joint to be analysed without the requirement for an inordinate amount of disc space and CPU time. This technique is computationally more expensive than analyses in which 2- or 4-fold symmetry is invoked but it is less costly in preprocessing time and removes the possibility of spurious symmetries in the results. For example, applying symmetry to a half-model with a single saddle crack effectively produces a model with two cracks: such effects require investigation.

The FE meshes comprise eight noded subparametric quadrilateral curved shell elements remote from the chord/brace intersection. Near this intersection, the geometry of the weld and the crack require the use of solid

elements and this area was meshed with superelements composed of 20-noded isoparametric hexahedrons (fig 9.2). The conjunction of these bricks and the shell elements was effected by 12, 15 and 18-noded transition elements (fig 9.3) as in fig 9.4. The crack tip elements are degenerate 20-noded hexahedrons in which one side has been collapsed to form the crack front (figs 9.5 and 9.6). A typical mesh for a complete T-Joint is shown at fig 9.7 while the $\frac{1}{4}$ joint in fig 9.8 allows the change in element types at the weld and crack to be clearly seen.

Realistic problems run through SESAM tend to require scratch files of the order of hundreds of Megabytes. However, by careful management of the superelement hierarchy and by using as coarse a mesh as experience allows wherever possible, the problem size can be reduced sufficiently to be run a microVAX II with 150 Mbytes of scratch space.

Results are presented graphically using either a non-dimensionalised K or J depending on the solver used (ABAQUS produces answers as J whereas TUSTRA produces both K and J) but where possible K is used as it is more appropriate to an elastic model. In those showing variation in K or J along a crack a best fitting curve has been drawn by use of the quadratic regression technique.

9.1.1 ABAQUS Models

To allow validation of the SESAM elements against the ABAQUS elements themselves benchmarked in section 8, the mesh generated for SESAM was tailored to suit ABAQUS. This is not a trivial matter, for the modelling philosophy in PRETUBE relies on the availability of multilevel superelements which are not available in ABAQUS. It is then necessary to combine all of the lower level superelements into one large "superelement". This process is very demanding on disk space and several attempts were made to force this through the available storage. Furthermore, in the normal assembly of a hierarchy of superelements, the processor condenses out coincident nodes. In the present case, this tends to lead to closure of the initially coincident nodes which define the undeformed crack and care was needed to ensure that these were retained. Finally, PRETUBE generates a complete crack within a

superelement but to bring the problem down to a manageable size for the ABAQUS analysis, it was necessary to make use of the symmetry of the model and use a half crack. In those cases where the crack fell on a line of symmetry for the T-Joint (pure tension and out of plane bending), there is a need to split a PRETUBE superelement. Again, this proved to be extremely time consuming.

This work had similar aims to those of a second group running ABAQUS at Glasgow and, to avoid duplication, the 3-D meshes were passed to this group for insertion of the boundary conditions and redefinition of the SESAM transition elements as ABAQUS 20-noded bricks. These results have been reported elsewhere (ref 12).

9.1.2 UCL Models

Finally, in order to validate the FE analyses against experimental results, four tubular T-Joint configurations were meshed, their geometries matching those included in the experimental fatigue crack growth work done at UCL (ref 10).

Initially, the uncracked joint was modelled as in Annexe 9.1 and subjected to axial loading on the brace member with both ends of the chord encastre (fig 9.9). This enabled the surface Stress Concentration Factor, K_T , to be found for this geometry. The remaining models each contained one of the crack sizes found in the experimental programme as shown in Annexe 9.1

The largest superelement in the T-joint meshes is that containing the crack, whose analysis typically requires about 50% of the total CPU time for the joint. It is the size of this element that principally determines whether or not the analysis can fit within the system parameters.

The size of the crack superelement varies significantly with the number of elements lying along the crack tip and in this case Crack 1 had 12 elements along the length of the crack, Crack 2 had 8 and Crack 3 had 10, giving a total superelement size of between 4500 and 6600 degrees of freedom.

9.2 Results

The SESAM results for a full joint (with no use of symmetry conditions) containing a single saddle crack and those for a model containing two symmetrically disposed cracks show a difference in the normalised values of G of the order of 3% as is shown in fig 9.10. The inaccuracy in the symmetric half-model is then considered an acceptable trade-off for a reduction in CPU time of the order of 25%, although the latter is clearly affected by the superelement replication and hierarchy. It was noticed that the general pattern (approximating to a parabola) of the results broke down in the elements near the surface. This was expected for two reasons: firstly the calculation of K near the material surface is unreliable and secondly, in this model, the elements at the end of the crack do not closely conform to the high local curvature of the structure (fig 9.11). Further, the SESAM analysis module TUSTRA uses virtual crack extension to calculate K and G at the crack tip nodes and assumes a Mode I opening. In contrast to the linespring analysis of Hancock and Du (ref 12) these results may be expected to be less reliable as the crack depth increases.

9.2.1 ABAQUS Comparison

Some of the results from the ABAQUS analysis using the PRETUBE generated mesh have been reported in ref 12 but here it is appropriate to compare the results of runs using SESAM and ABAQUS for an axial load and out of plane bending (fig 9.12a & 9.12b). It was found that the two solvers give close agreement in both cases, although the ABAQUS results are more strongly affected by the greater curvature in the end elements.

9.2.2 UCL Comparison

From the results obtained in the analysis of the uncracked joint the SCF at the weld toe in the saddle position was calculated and compared with the theoretical results of Gibstein, Kuang and Wordsworth (ref 24) and the experimental results (Annexe 9.2). The through thickness stress distribution found at the weld toe in the saddle position is shown in fig 9.13 from which it may be seen that the proportion of bending was 71% compared with an

empirical value of 85% found at UCL.

The distribution of K for the three crack geometries studied is shown as normalised results in figs 9.14 - 9.16. With the exception of the results at the right hand side of Crack 1, which can be discounted as spurious in this symmetrical model, all three sets of results were in accordance with expectations in that the SIFs are highest at the deepest point (centre) of the crack and in the deepest of the three cracks. Annexe 10.3 summarises the maximum K values and shows the derivation of the Y geometric parameter.

The discrepancy between the FE and experimental results (figure 9.17) was within 5% for the shortest crack length studied but this increased to 30% for $a/t = 0.8$. However, at this value of a/t the accuracy of the experimental value is questionable since other work (ref 25) has shown that experimentally derived Y values are very sensitive to the material constants assumed. Furthermore, for deeper cracks, the relative magnitudes of K_{II} and K_{III} in relation to K_I will increase (ref 26) as the crack starts to deviate under the weld and in such circumstances the SESAM results become less reliable. It was noticed that the results produced a sawtooth pattern, believed to be due to the differing degrees of overconstraint resulting from differing numbers of nodes at element ends and mid-points. Although the results are less accurate for a deeper crack, their accuracy for a shallow crack is of greater practical relevance as most cracks will be identified sufficiently early to provide foreclosure on the options open to the operator.

In order to validate a less computationally intensive method of assessing approximate values for stress intensity factors at a crack tip in a tubular joint, analyses were carried out in which a crack was modelled in a flat plate, the material thickness and crack dimensions being the same as for a tubular joint previously analysed (UCL Crack 1). Two load cases were applied both giving the same ratio of tension to bending as in the complete T-Joint model with the latter, load case 2, having the same value for tension. The results were normalised against the surface stress at the location of the crack mid-point in the uncracked geometry. The initial results (for UCL Crack 1) show (fig 9.18) a high level of agreement.

Further work (using UCL Crack 2) gave the results shown in fig 9.19

which shows a poorer degree of correspondence between the two methods was obtained, the results at the crack mid-point being better than at the ends. Two factors may be responsible for this. Firstly, the distortion of elements near the material surface will affect the results and secondly, as can be seen from Annexes 9.4 and 9.5, the stress field remote from the material surface in the tubular joint differs significantly from that found in the flat plate. As the comparison is made on the basis of the surface stress in both models it is reasonable to assume that, while this is an accurate method for shallow cracks, it is less reliable as the crack front moves deeper into the material and the stress field at the crack tip varies significantly from that predicted in the simple flat plate model. It would be possible to more accurately model the stress field in the crack tip region, ^{but} the amount of work involved would be such as to defeat the original aim of simplifying the analysis.

9.3 Conclusions

Apart from the inaccuracies at the material boundary, mentioned in section 7 and aggravated, in this section, by the variation in curvature of a semi-elliptical crack, the FE solutions give a high and reliable level of agreement with results found by other methods. Simple solutions, such as line-springs and flat plate models are reasonably accurate for deep cracks, however, for shallower cracks, it is necessary to accurately model the geometry of the joint in detail, and accept the computational cost, rather than try to replicate the stress distribution on a simpler model.

Tubular T Joint and Crack Geometries

Dimensions

Chord outer dia = 460mm
Chord wall thickness = 16mm
Brace wall thickness = 12.7mm
Brace outer dia = 325mm
Chord length = 2440mm
Brace length = 1245mm

$$\beta = 0.707$$

$$\gamma = 14.375$$

$$\tau = 0.794$$

$$\alpha = 10.609$$

Crack 1

a = 2.44mm c = 35.71mm chord crack at saddle position

Crack 2

a = 6.70mm c = 66.67mm as above

Crack 3

a = 12.00mm c = 111.43mm as above

a = crack depth

c = crack half length

Annexe 9.1

Stress Concentration Factors

Gibstein $1.04\{1.5-3.88(\beta-0.47)^2\} \gamma^{0.87} \tau^{1.37} \alpha^{0.057}$
= 11.305

Kuang $2.06\alpha^{0.057} e^{-1.2\beta^3} \gamma^{0.808} \tau^{1.333} \sin^{1.694} \theta$
= 9.772

Wordsworth $\beta\gamma\tau(6.78 - 6.42\beta^{0.5}) \sin(1.7+0.7\beta^2)\theta$
= 11.151

TUJAP from the uncracked geometry Principal Stress (max)
 $9.97 \times 10^{-4} / 8.02 \times 10^{-5} = \underline{12.43}$

Geometric Factors (Y) for Cracks in a Tubular T Joint

Maximum values - located at deepest point.

All stresses in Nmm^{-2}

$$\text{Crack 1} \quad a/t = \frac{2.44}{16.00} = 0.1525 \quad K = 0.223 \times 10^{-2}$$

$$\begin{aligned} \text{remote stress} &= 8.02 \times 10^{-5} \\ \text{hot spot stress} &= 12.43 \times 8.02 \times 10^{-5} \end{aligned}$$

$$Y = \frac{K}{\sigma \sqrt{\pi a}} = \underline{0.81}$$

$$\text{Crack 2} \quad a/t = \frac{6.70}{16.00} = 0.419 \quad K = 0.316 \times 10^{-2}$$

$$\begin{aligned} \text{remote stress} &= 8.02 \times 10^{-5} \\ \text{hot spot stress} &= 12.43 \times 8.02 \times 10^{-5} \end{aligned}$$

$$Y = \frac{K}{\sigma \sqrt{\pi a}} = \underline{0.69}$$

$$\text{Crack 3} \quad a/t = \frac{12}{16} = 0.75 \quad K = 0.367 \times 10^{-2}$$

$$\begin{aligned} \text{remote stress} &= 8.02 \times 10^{-5} \\ \text{hot spot stress} &= 12.43 \times 8.02 \times 10^{-5} \end{aligned}$$

$$Y = \frac{K}{\sigma \sqrt{\pi a}} = \underline{0.60}$$

Annexe 9.3

Stress Field at T-Joint Saddle

Stress at Mid Point of Chord at Saddle (uncracked UCL geometry)

$$\sigma_{xx} = 0.1778E-03$$

$$\sigma_{yy} = 0.3639E-04$$

$$\sigma_{zz} = 0.1236E-03$$

$$\tau_{xy} = -0.3528E-04$$

$$\tau_{xz} = 0.2194E-06$$

$$\tau_{yz} = -0.8246E-07$$

Principal Stress at Mid Point of Chord at Saddle (uncracked UCL geometry)

$$P_1 = 0.1862E-03$$

$$P_2 = 0.1236E-03$$

$$P_3 = -0.6645E-03$$

Annexe 9.4

Stress Field in Flat Plate

Stress at Mid Point of Flat Plate

$$\sigma_{xx} = -0.7473E-05$$

$$\sigma_{yy} = 0.1832E-04$$

$$\sigma_{zz} = 0.1355E-03$$

$$\tau_{xy} = -0.1066E-13$$

$$\tau_{xz} = -0.2503E-05$$

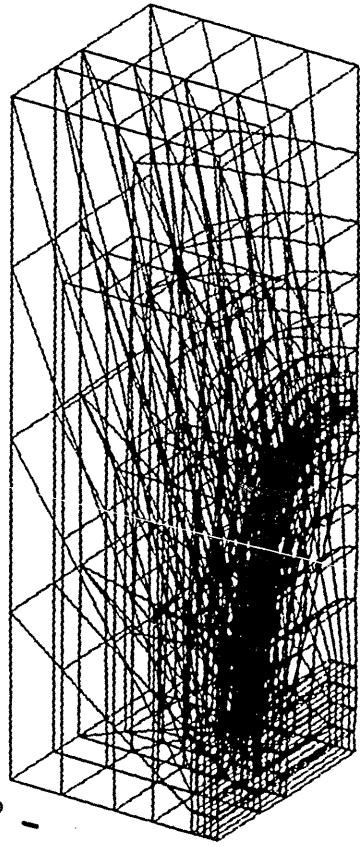
$$\tau_{yz} = -0.1208E-12$$

Principal Stress at Mid Point of Flat Plate

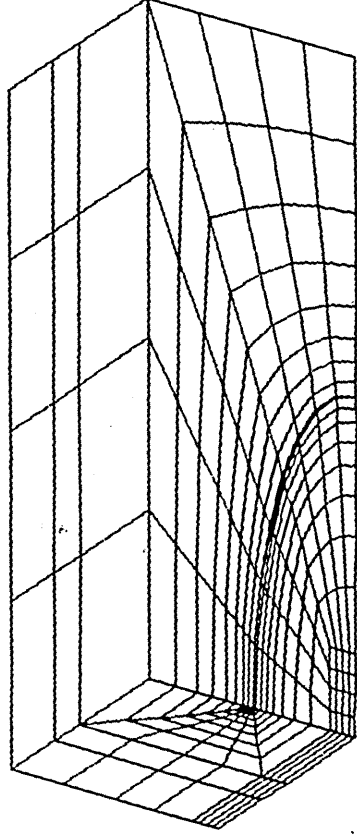
$$P_1 = 0.1356E-03$$

$$P_2 = 0.1832E-04$$

$$P_3 = -0.7517E-05$$



(a) Crack mesh



(b) Crack mesh (hidden view)

fig 9.1 FEMGEN generated crack mesh (showing a high number of seriously distorted elements)

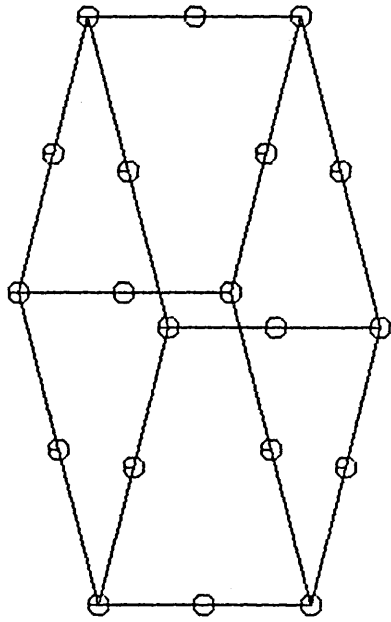


fig 9.2 20 Noded isoparametric hexahedron

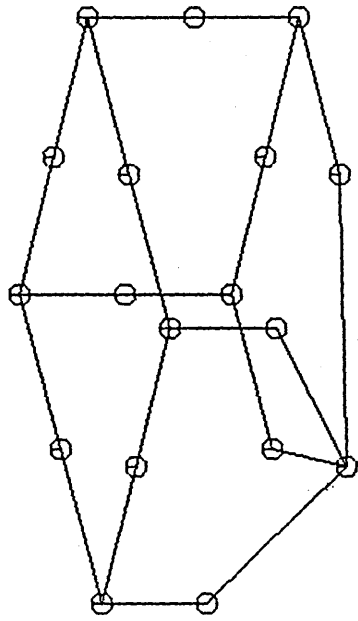


fig 9.3a 18 Noded transition element

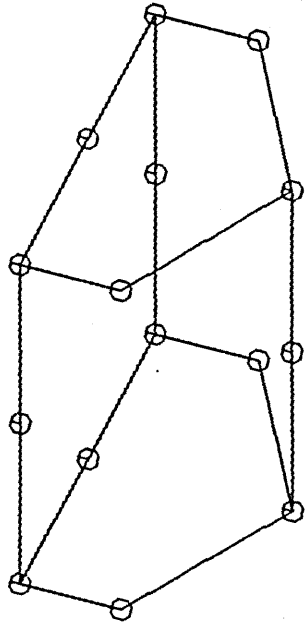


fig 9.3b 15 Noded transition element

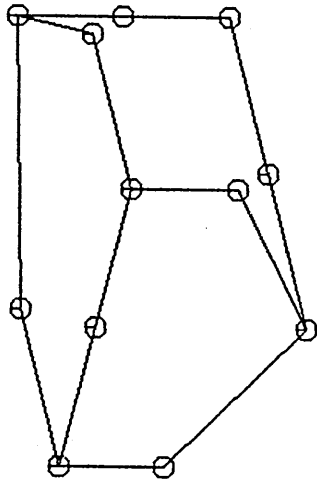
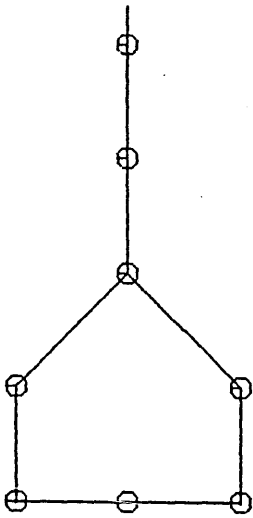


fig 9.3c 12 Noded transition element

SESAM transition elements



ABAQUS multi-point constraints

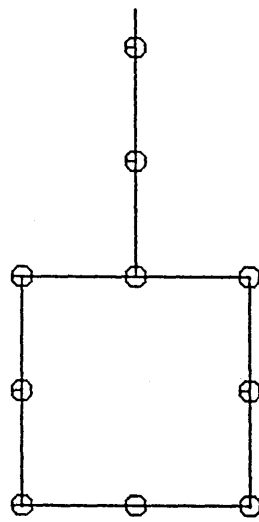
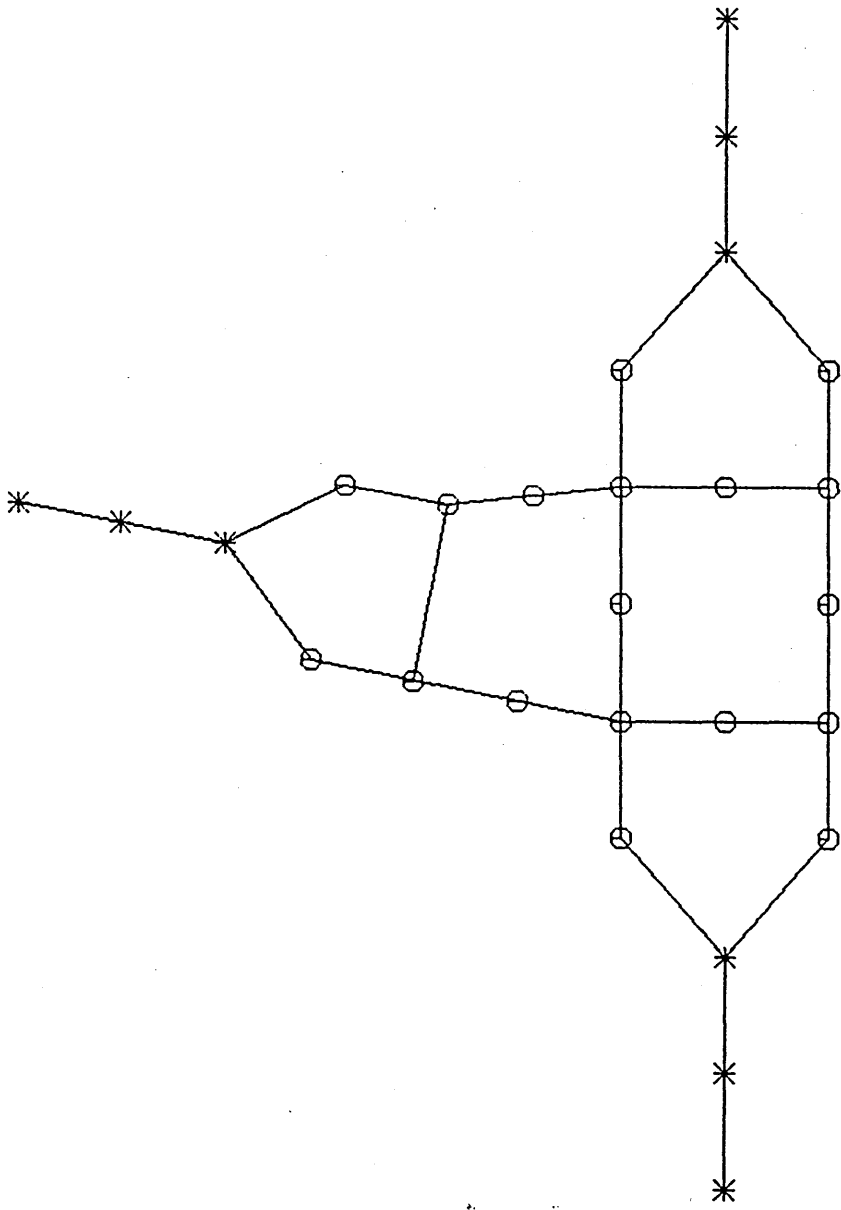


fig 9.3d. SESAM transition elements and ABAQUS multi-point constraints

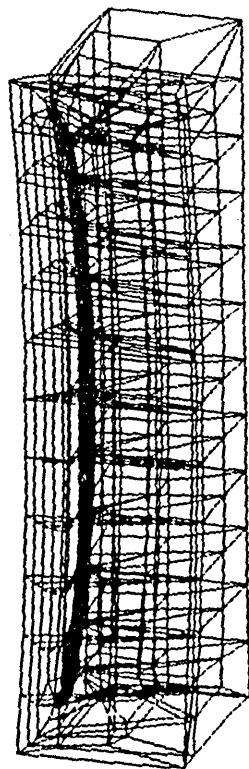


○	Solid nodes
*	Shell nodes

fig 9.4 SESAM meshing of solid welds

SESAM
POSTFEM

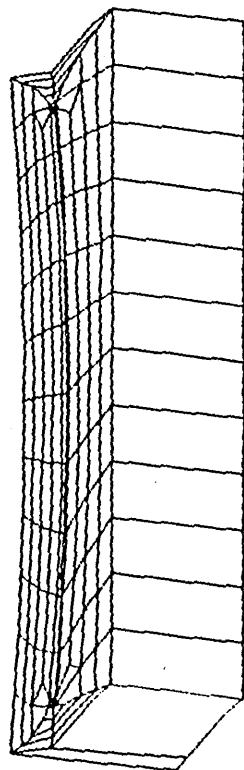
MODEL: 12



x
y z

SESAM
POSTFEM

MODEL: 12

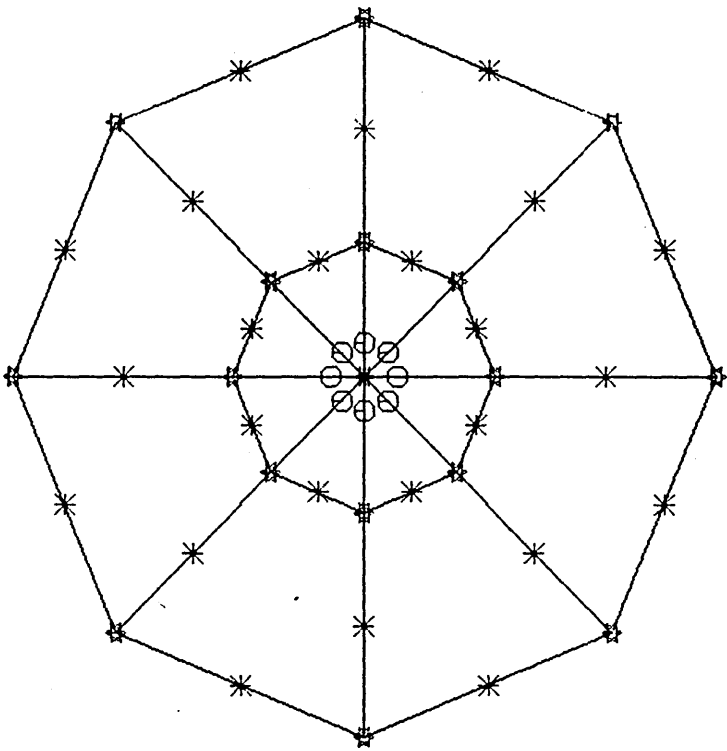


x
y z

(a) Crack mesh showing weld toe

(b) Crack mesh (hidden view)

fig 9.5 SESAM crack mesh



⊕	Midside nodes in quarter pt posn
*	Midside nodes
⊠	Corner nodes

fig 9.6 Focussing of mesh in SESAM crack superelement

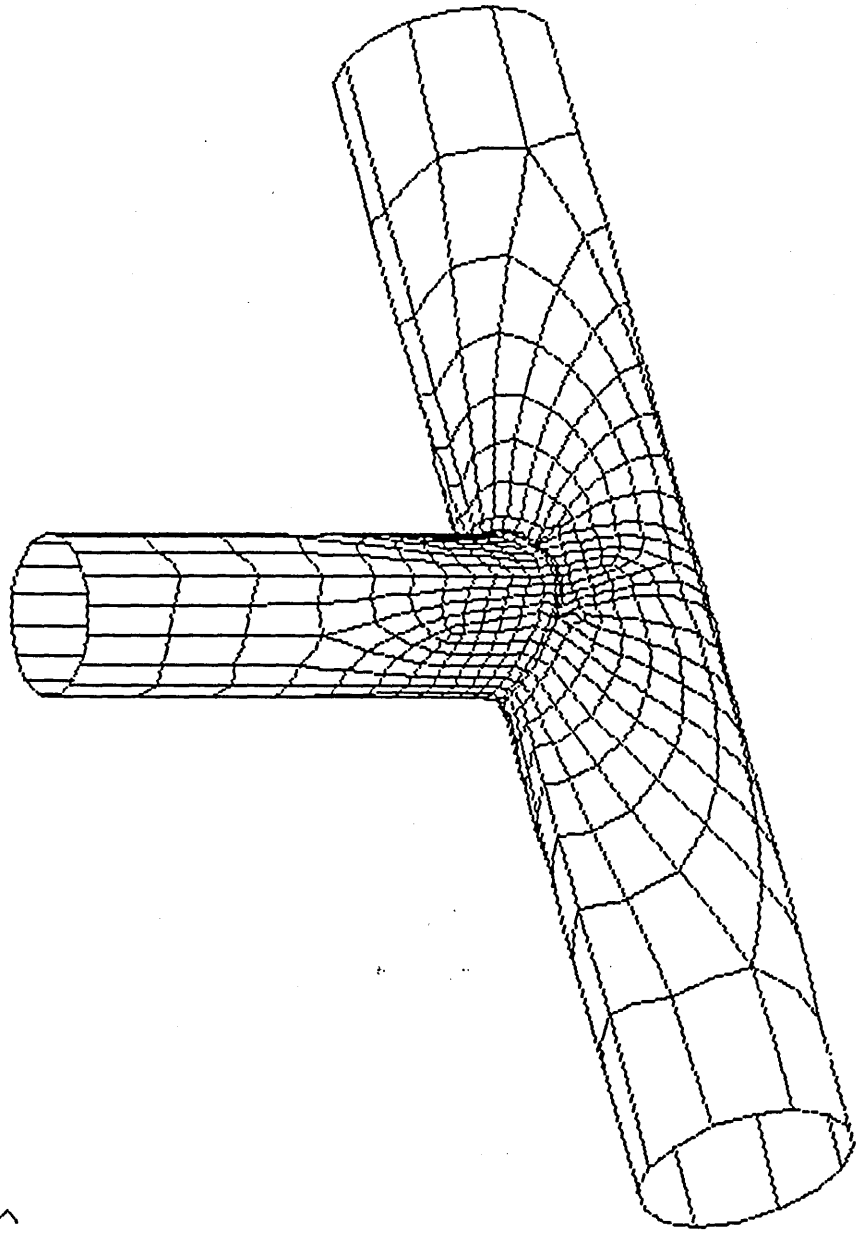


fig 9.7 Fully meshed T-Joint

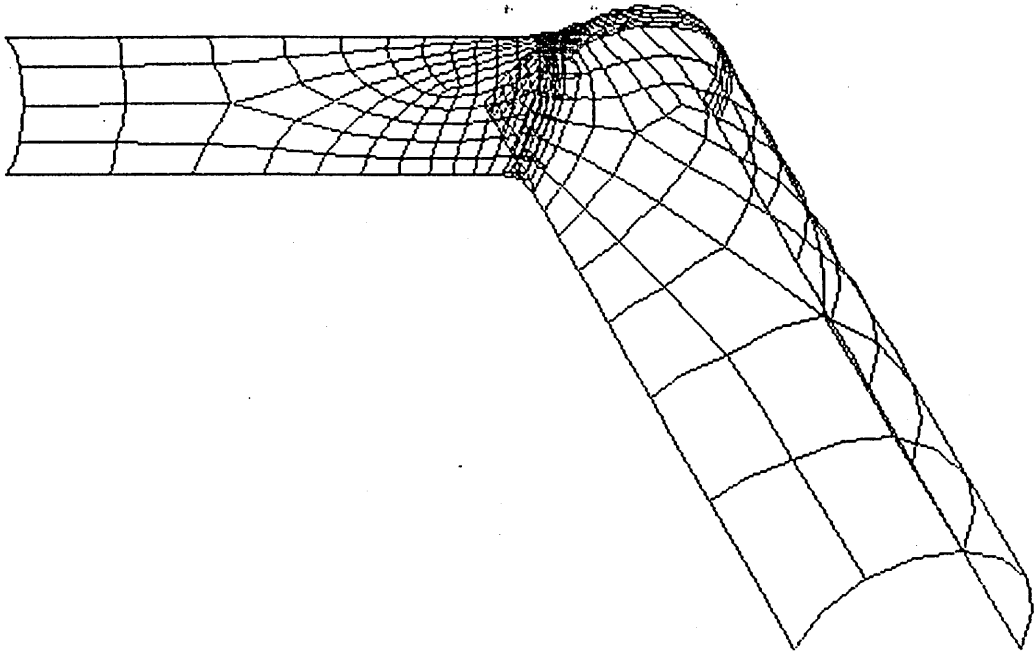


fig 9.8 Fully meshed 1/4 T-Joint with weld toe crack at chord saddle position

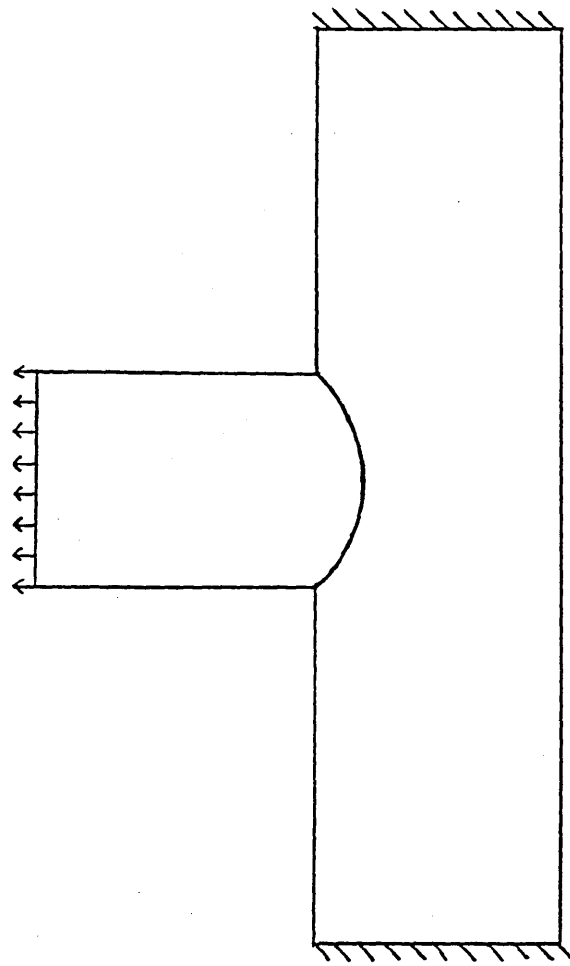


fig 9.9 Load cases, UCL models

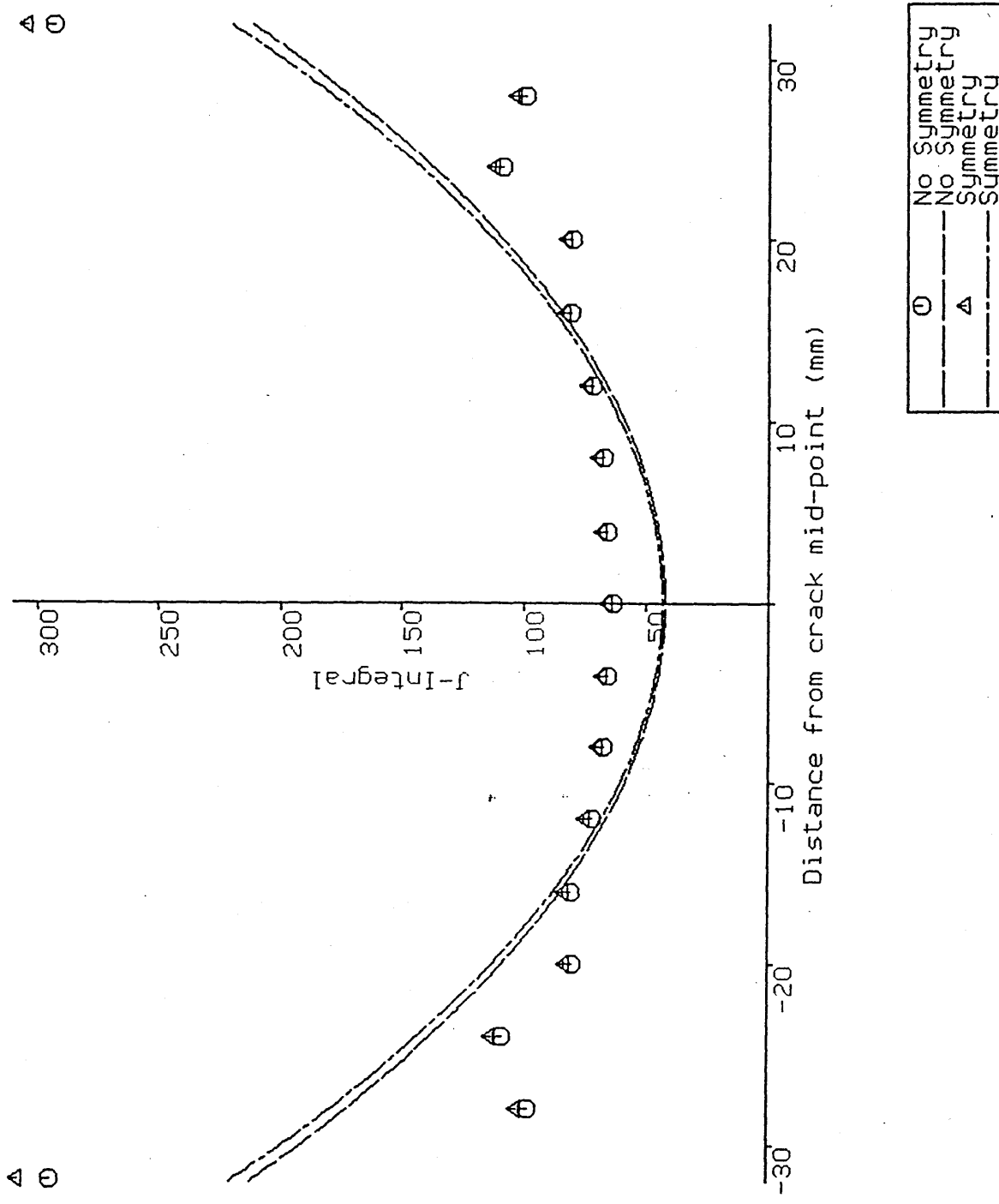


fig 9.10 Effect of assuming symmetry on a cracked T-Joint

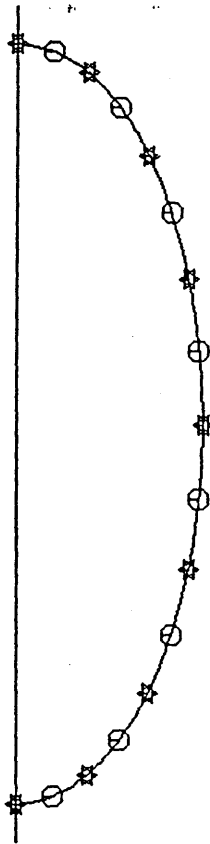


fig 9.11 Nodal clusters on a semi-elliptical crack

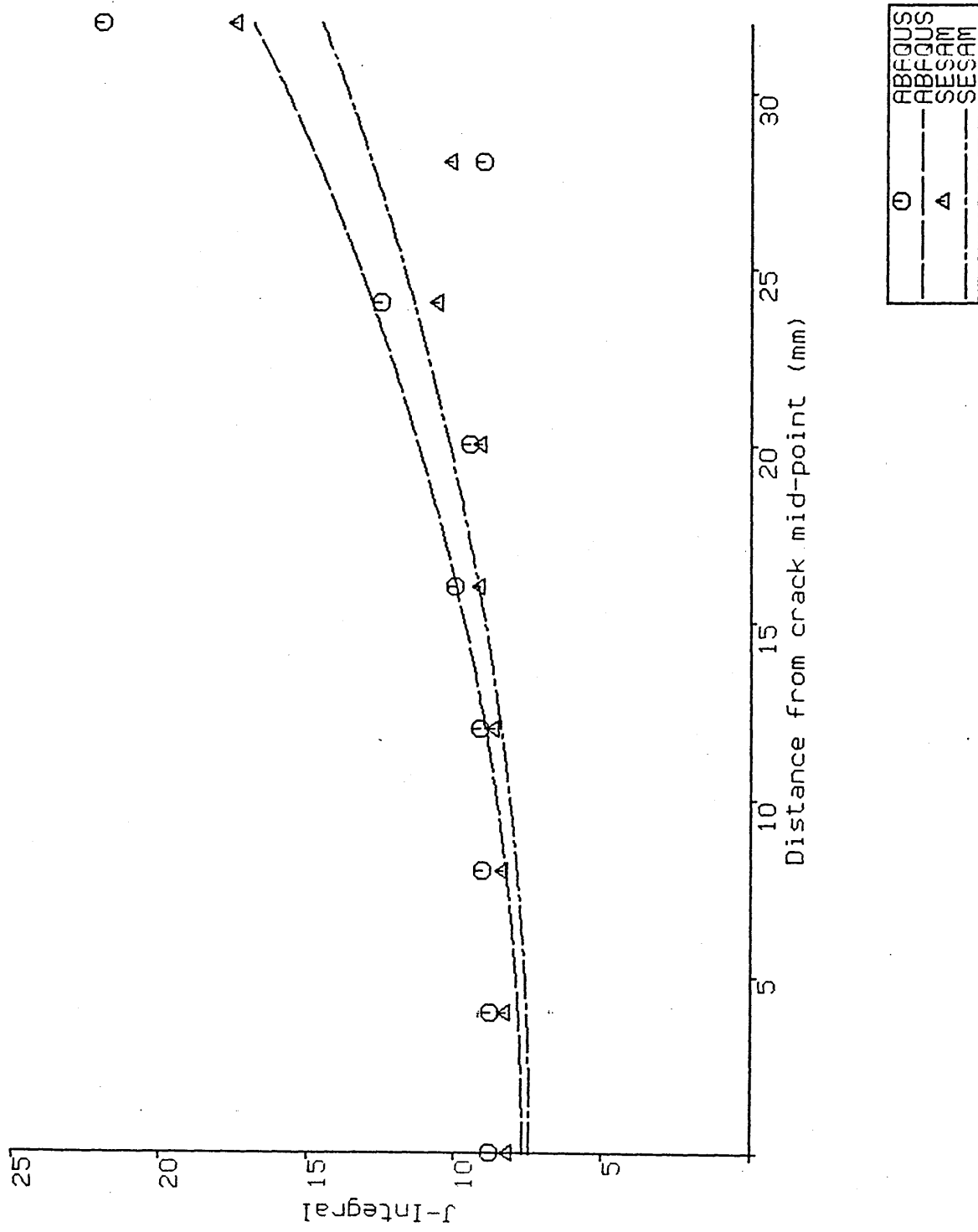


fig 9.12a Crack Driving Force: SESAM and ABAQUS, Axial Loading

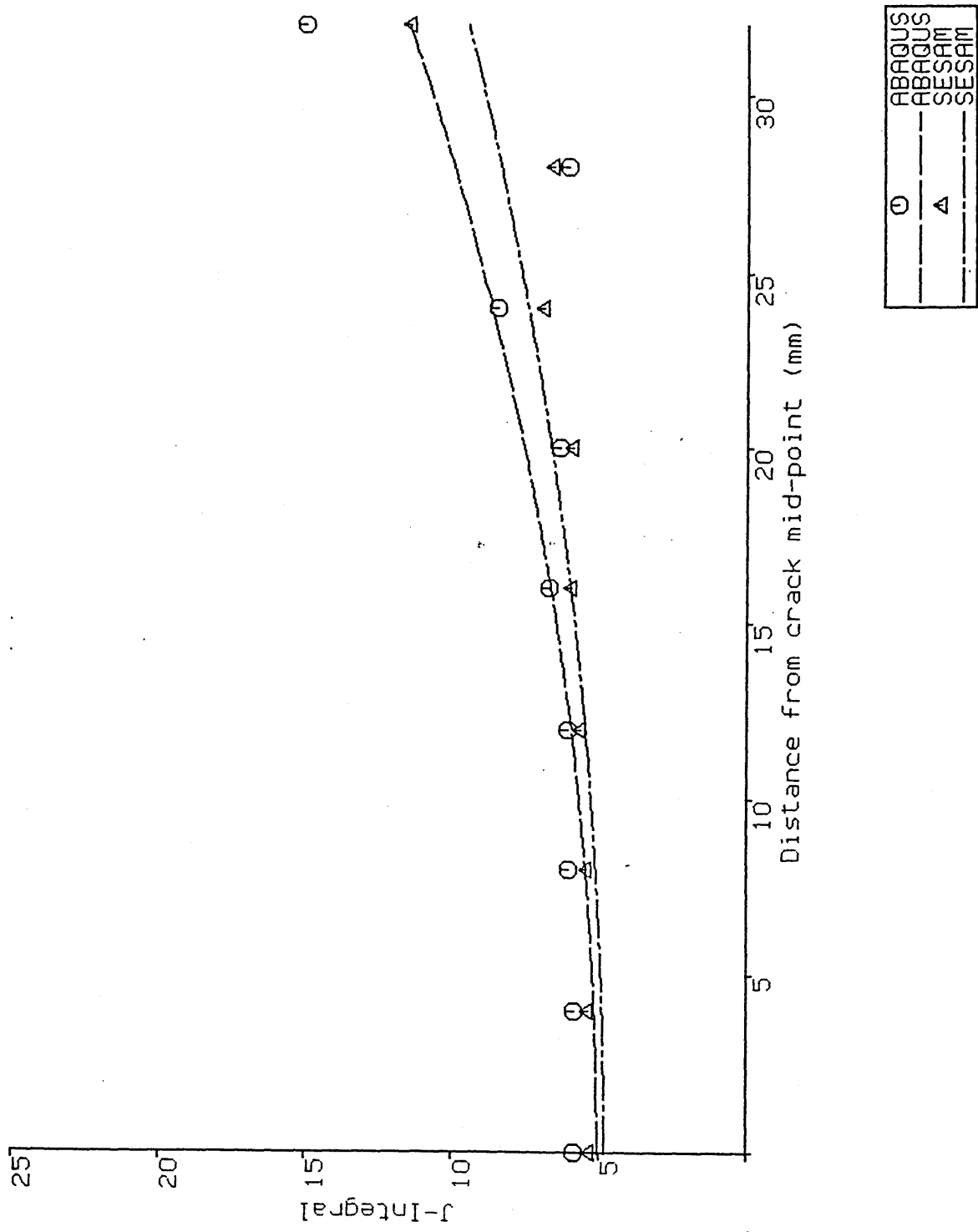
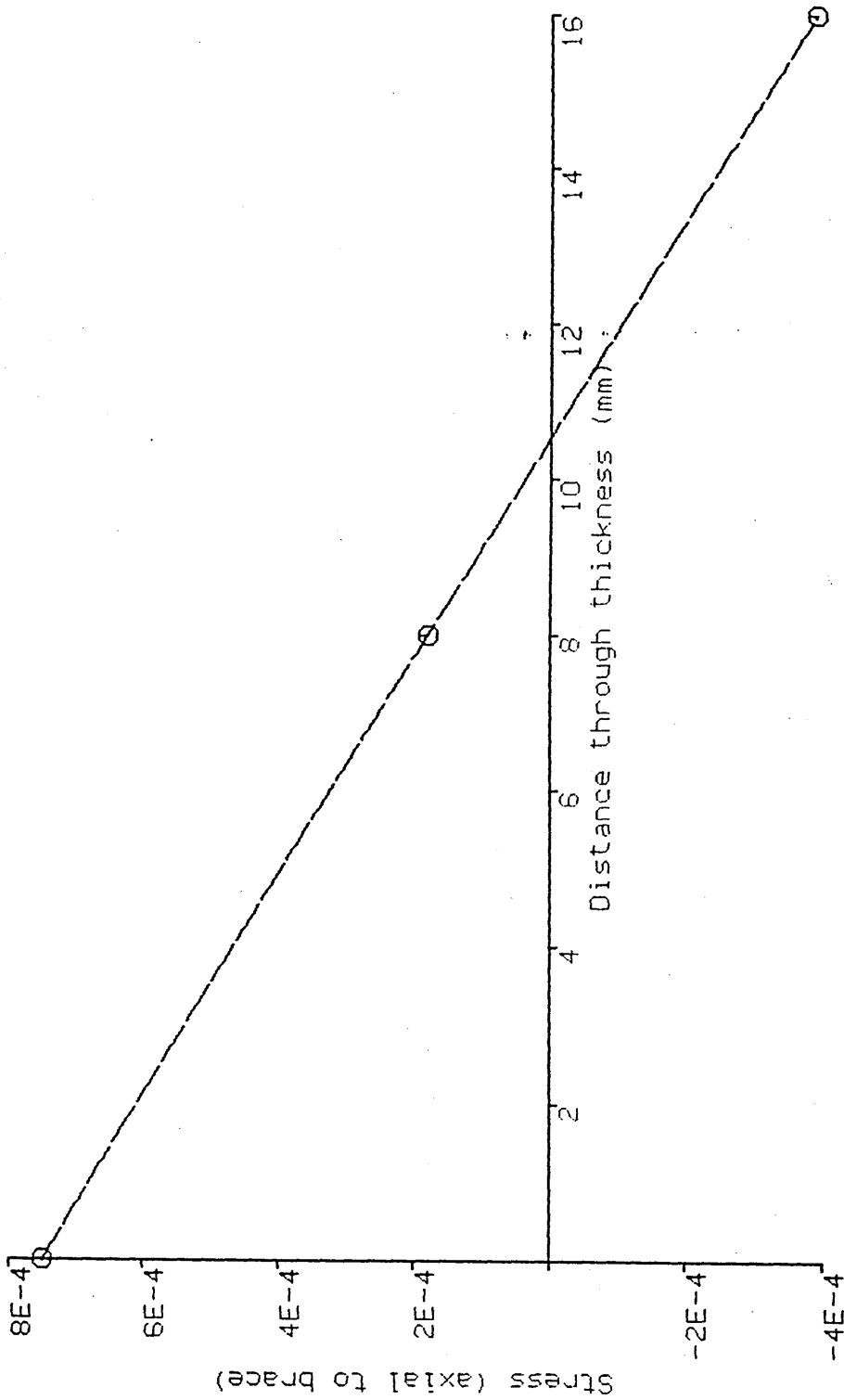


fig 9.12b Crack Driving Force: SESAM and ABAQUS, Out of Plane Bending



Ratio of bending:total = 71%

fig 9.13 Through thickness stress distribution, chord saddle position, UCL geometry.

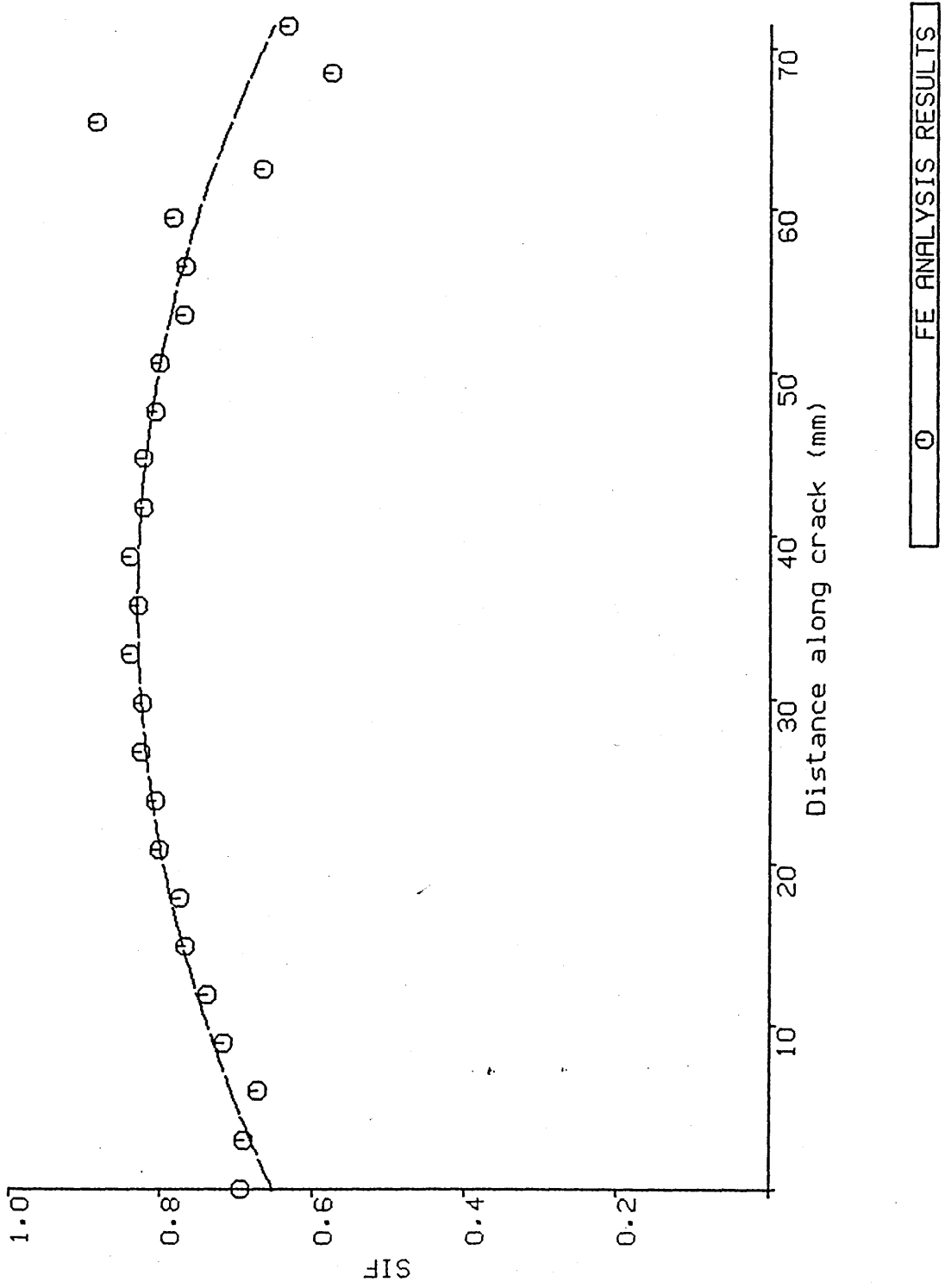


fig 9.14 Stress Intensity Factors: UCL CRACK 1.

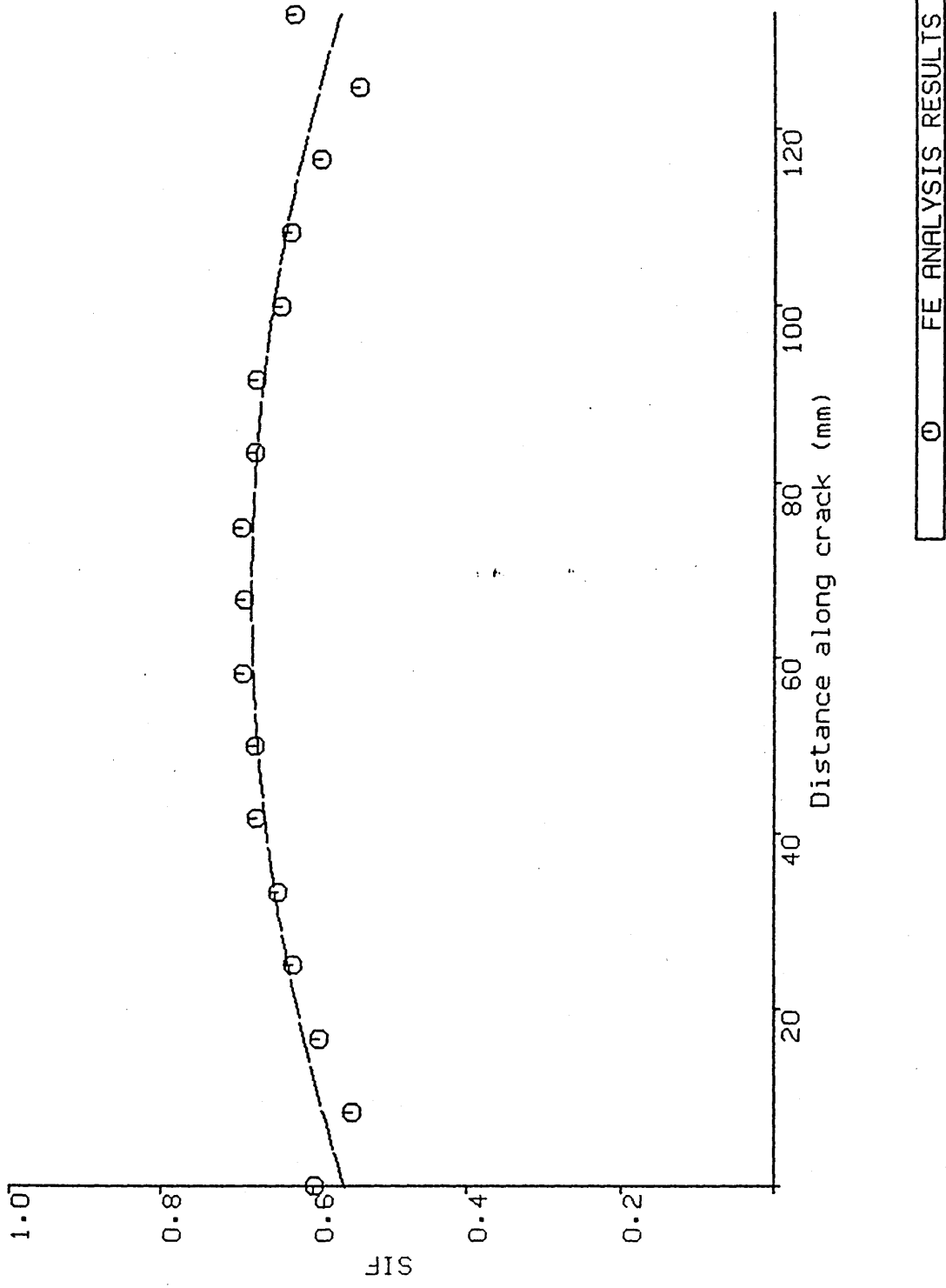


fig 9.15 Stress Intensity Factors: UCL CRACK 2

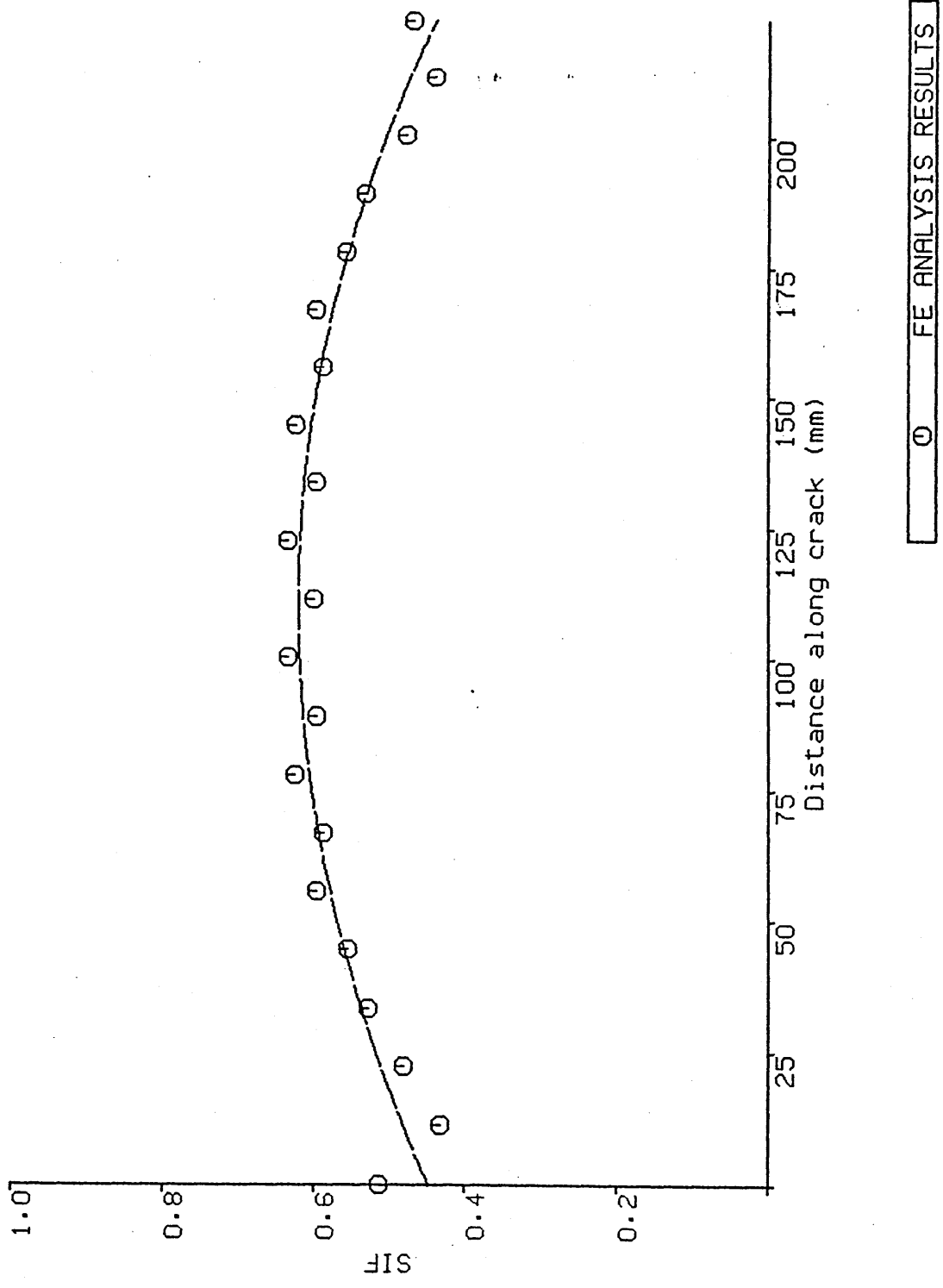


fig 9.16 Stress Intensity Factor: UCL CRACK 3

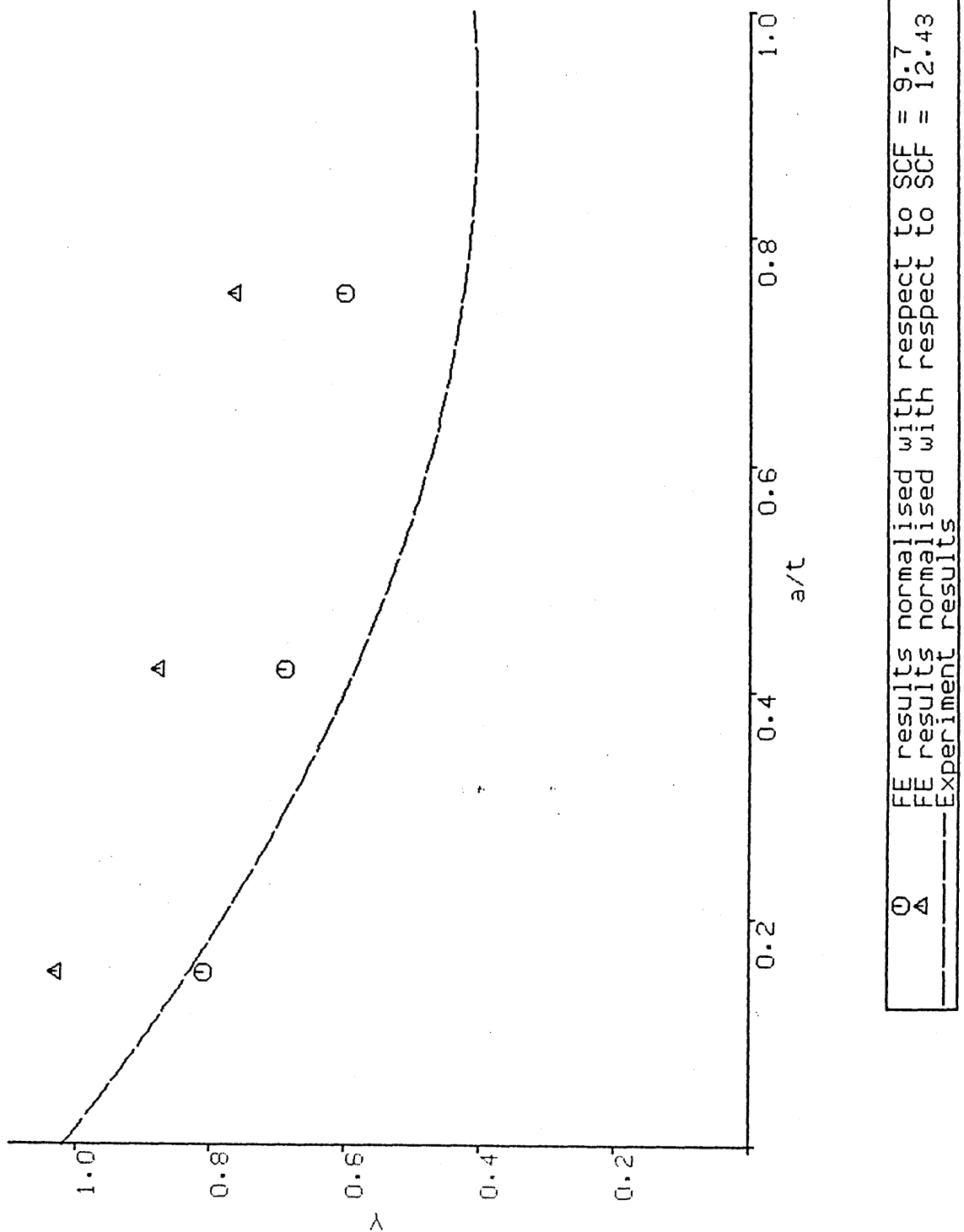


fig 9.17 SESAM vs weight function (UCL)

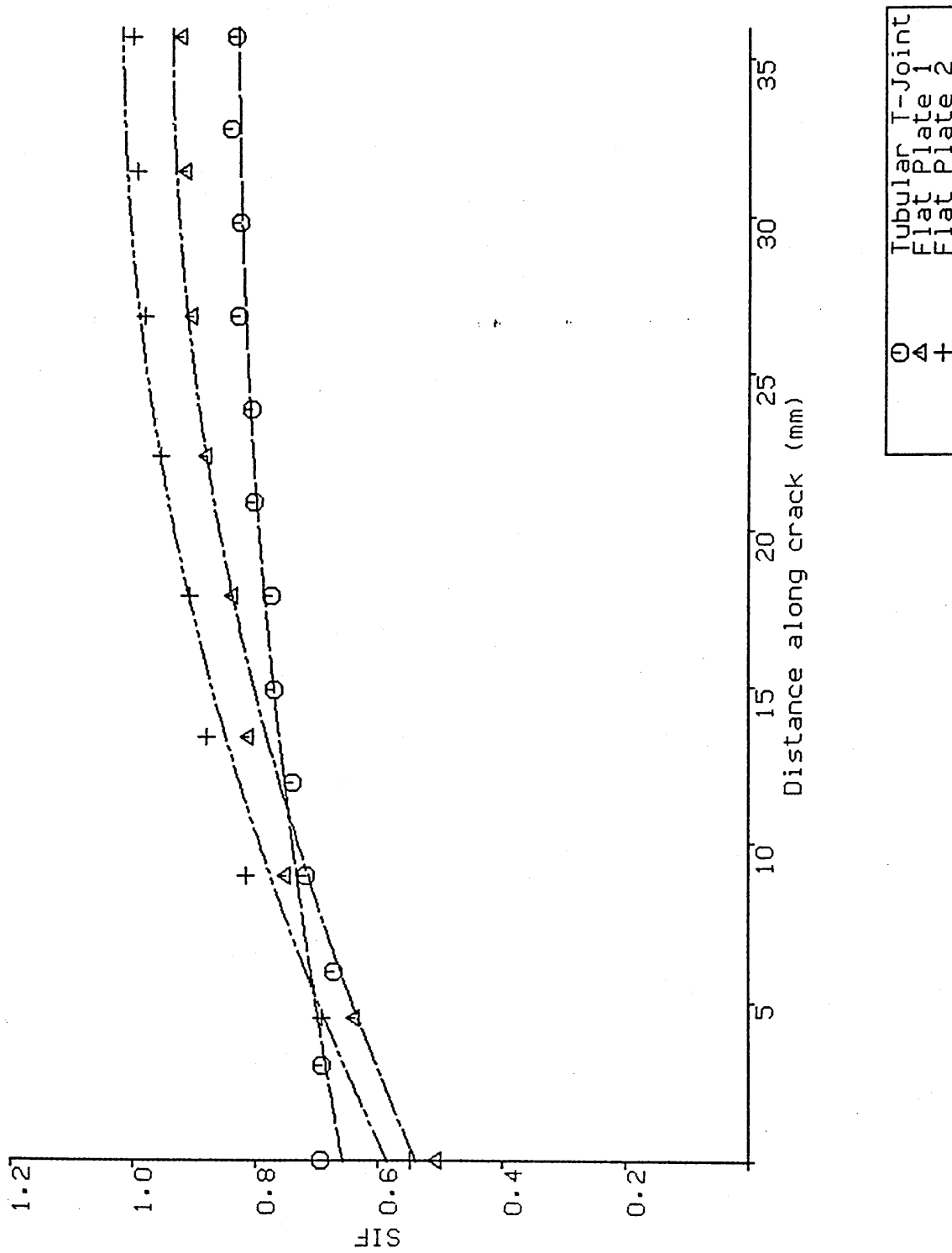


fig 9.18 Stress Intensity Factors: UCL CRACK 1, Flat Plate & T-Joint results

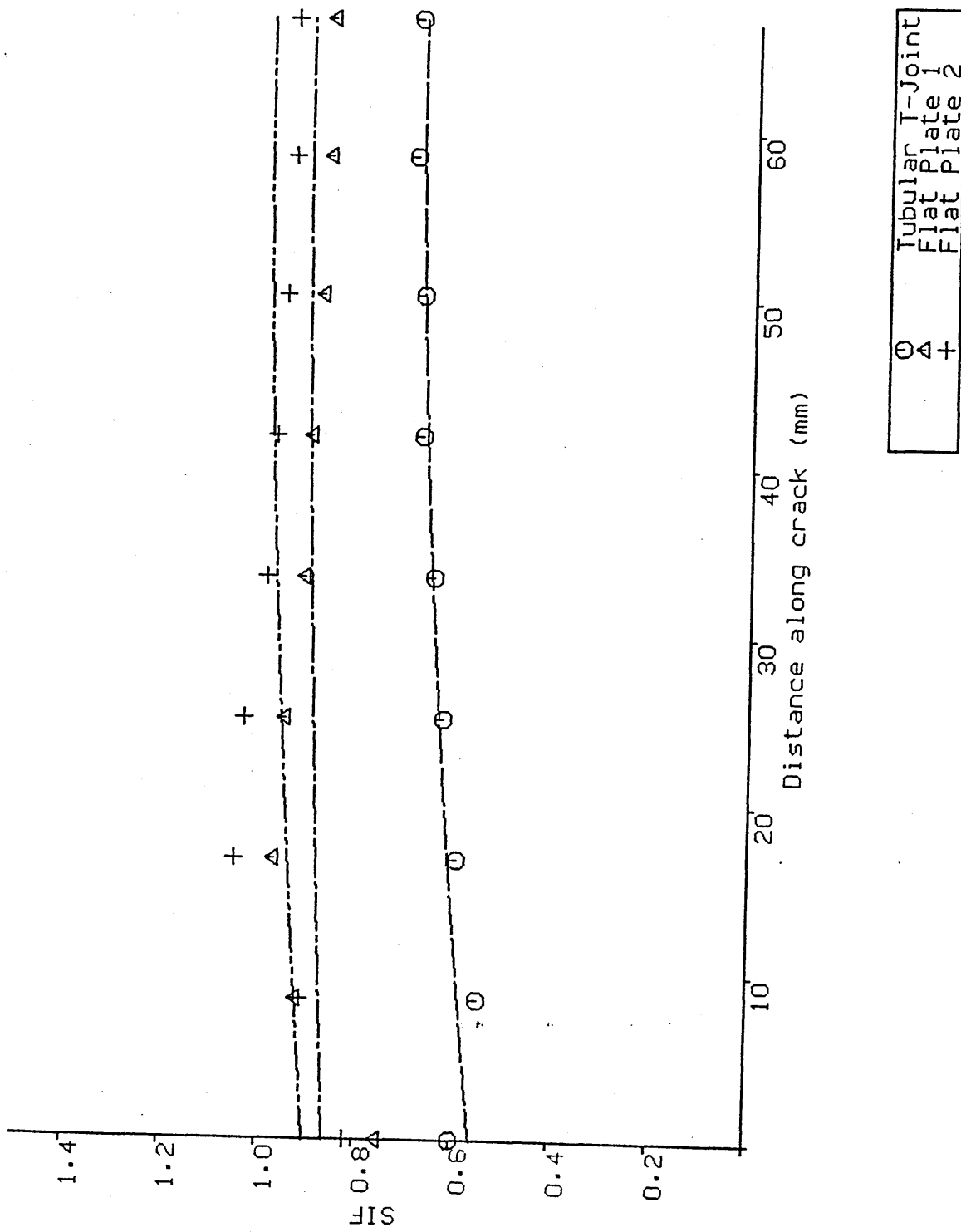


fig 9.19 Stress Intensity Factors: UCL CRACK 2, Flat Plate & T-Joint results

10.0 CONCLUSIONS AND DISCUSSION TO SECTION B

10.1 Discussion

By careful analysis of simple geometries and comparison of FE results with known (and accredited) empirical and theoretical solutions some understanding has been gained of the importance of a number of parameters in the control of the mesh. On the basis of these guidelines, gained in the analysis of simpler cases, a high level of confidence can be placed in the complex FE meshes used to model full joints. Furthermore, the comparison of the corresponding analyses with results from other sources has also tended to validate the system used here.

In addition to ensuring that the mesh geometry itself is not causing spurious numerical inaccuracies, care must be taken to choose and apply accurate, realistic and appropriate boundary conditions. Frequently, this involves a degree of simplification based on the judgement and experience of the analyst rather than a straightforward transfer of information.

Although the current results, indicate that FE analyses are acceptable for many applications, as the software and hardware continue to improve there will be a tendency towards progressively larger and more complex analyses. This trend will exacerbate the problem of validating results obtained from FE solutions, hence it is important that this validation and associated QA procedures become an integral part of the FE development process. The ability to carry out complex analyses at reduced cost will bring about a change in the approach to the analysis of T-Joints resulting in a FE analysis being carried out for each specific joint and even possibly the complete structure rather than the use of semi-empirical equations as at present.

10.2 Conclusions

The FE analysis of full 3-D crack meshes in tubular welded joints is a valid method of assessing SIFs. For deep cracks ($a/p < 0.75$) (ref 26) and axial loading Mode I predominates (ref 27). For other cases, the increased ratio of mode II to mode I loading makes the FE solutions using the virtual

crack extension method (which produces results approximating to mode I loading) less reliable. For such cracks however, the linespring technique is particularly accurate and so the two methods are complementary.

Recent developments, not then available, allow prediction of the different modes of opening using a 3-D model.

For short shallow cracks, the influence of the weld profile is significant, in which case a full 3-D model must be analysed. This is facilitated by programs such as SESAM's PRETUBE special purpose preprocessor. Such analyses are particularly useful in offshore operations in order to assess defects before they are beyond economic repair.

SECTION C: GRIND REPAIR OF TUBULAR WELDED JOINTS

11.0 Introduction

11.1 Background

When a crack is detected at a joint in an offshore structure there is a requirement on the operator to take some form of action to cope with this problem. Remedial grinding is the most frequent repair procedure used for removing crack-like defects in the tubular welded joints of offshore structures. It has been shown (ref 28) that even very deep remedial grinding can produce substantial benefits to the residual fatigue life of such structures. There is currently little guidance on the optimum ground groove profile for such repairs. The detailed mechanisms which lead to fatigue life improvements are also little understood.

The work carried out here, used the Finite Element technique and attempted to provide a wider understanding of the effect of grind repairs and to provide some guidance as to their applications.

11.2 Aim

Although the initial stage of this work was essentially a pilot study for future research, it was planned that it would cover two main areas. Firstly, it was intended to provide a justification of the use of 3-D FE analysis in this field by carrying out a comparison between FE results and results derived from other sources and secondly, a limited study of the effect of varying a number of groove geometry parameters was undertaken.

11.3 FE Stress Analysis

In early autumn 1988, VSS released to GMTC a research version of their preprocessor PRETUBE which contains an automatic meshing facility for grind repairs at the weld toe of a tubular joint. As this software was not yet

commercially available, VSS were unable to support it to the same extent as their other programs. In addition the level of documentation and user guidance available for this software was very low.

Due to the two factors mentioned above it was necessary to undertake an extensive programme of modelling to find, virtually by trial and error, the limiting parameters for the mesh and groove geometries available using this software.

To fully assess the capabilities of the program it was decided to carry out a series of analyses using realistic groove geometries. In order to facilitate this, British Gas released to GMTC details of an experimental programme involving grind repair of a tubular T-Joint. At a later stage in the programme details of a series of experiments carried out at The Welding Institute also became available.

12.0 RESULTS

12.1 Presentation of Results

For the purpose of this report "*along*" the groove is defined as the direction of movement of the cutting tool, while "*across*" the groove is the perpendicular path i.e. around the groove in the tubular circumferential direction.

The groove SCFs have been calculated using the original material thickness to calculate the nominal stress. This differs from the procedure used in the literature for the 2-D equations. Where these equations are used, the solutions have been adjusted to allow for this change.

12.2 Preparatory Work

The basic geometry made available by British Gas (fig 12.1), consisted of a double T-Joint subjected to in-plane-bending with grind repairs located at the brace crown position. This was analysed and the results used to derive both the SCF and the ratio of tension to bending at the brace crown position. The SCF results were compared with accepted formulae (ref 24) as shown at Annexe 12.1 and a high level of agreement was obtained. The accuracy of this result formed the basis for justifying the extension of the model to include ground grooves. The ratio of tension to bending was used later in the comparison of the groove results with 2-D equations.

At a later stage the basic geometry from the Welding Institute programme (fig 12.2), a single T-Joint subject to out of plane bending with the grind repairs at the chord saddle position was also analysed. The SCF results from this case are shown at Annexe 12.2. Although the value of SCF found in this case is below that predicted it remains close to the lower end of the range of predicted values and is therefore acceptable. A variety of factors within the model may account for the degree of difference, ie weld geometry, details of the load application, etc.

To develop a reasonable degree of understanding of the capabilities of

the available software an attempt was made to model a series of grind repairs in a tubular welded joint. This proved to be extremely time consuming. Firstly, the modelling of these geometries is an interactive process taking, at best, a full working day and on occasions up to a week. Secondly the program being used was found to be unreliable at times and frequently crashed for no apparent reason. Eventually a method was derived whereby the model was generated using the commercial version of PRETUBE, the groove was modelled using the research version, and the model was then returned to the commercial version. Several weeks were spent merely finding a way of generating a suitable model. A typical groove mesh is shown in fig 12.3, with stress contours shown in fig 12.4.

12.3 Analysis of BG Grooves

The information released by British Gas was in the form of experimental details covering work involving a series of weld toe grooves in the brace of a tubular T-Joint subjected to in-plane-bending (fig 12.1). A series of three grooves was selected from the experimental programme and analysed. All grooves were symmetrically located at the crown position and had a length of 6.2% of the brace circumference. Groove depths were 10%, 15% and 30% of the brace material thickness.

Results are shown in fig 12.5, which shows the strain along the groove centreline and the original strain at the weld toe. The strain was found to be highest for the deepest groove. Meshing effects near the surface of the material where the elements are badly distorted to fit the geometry result in inaccuracies at these points. Figure 12.6 shows the stress distribution over the groove surface and it is of interest to note that the distribution across the groove is not symmetrically distributed. In addition the ratio of bending/total stress through the remaining ligament was found for in each case to be 71%, little different from the 76% found in the as welded geometry.

In addition to modelling the experimental geometries a limited study was carried out to identify the importance of the groove radius. Each of the three experimental geometries was remodelled with varying groove radii the results being shown in figs 12.7 & 12.8.

These results were compared to the equations given in refs 29 & 30 by removing the factor due to the overall joint geometry from the FE solutions, with the results being shown in Annexe 12.3 and fig 12.9. Generally a reasonable level of agreement was obtained in this case although the results began to fall away for the cases with smaller radii.

The results of the three BG geometries were used to predict the remaining life of the structure using the Class T, S-N curve (ref 31), the results being shown at Annexe 12.4. The values obtained are compared with the original, as welded, fatigue lives, although in a situation requiring a grind repair the true basis of comparison would be the cracked rather than the as-welded case. This S-N curve consists of two sections, either side of 50Nmm^{-2} (10^7 cycles), and the comparison has been made for both cases. It was observed that, if the T-Curve is valid in this case, the fatigue life falls away sharply as the depth of the grind is increased, especially at low stress ranges. Fortunately, the fatigue lives of nodes subjected to low stress ranges are typically orders of magnitude greater than for higher stress ranges.

12.4 Analysis of TWI Grooves

A groove geometry was selected from the TWI programme (ref 32) and modelled. Unlike the grooves modelled in section 12.3 the groove in this case did not have a uniform depth. The groove depth fluctuated considerably along the groove length, making the modelling process considerably more difficult (fig 12.10). The results obtained are shown in fig 12.11. Initially the FE results were found to be about 20% lower than predicted by the experiment, however when the results are normalised against the SCF due to the original geometry a very high level of agreement was achieved. In addition, the centre of the grind was assumed to be equivalent to a flat plate and the results were compared against those predicted by Roark (ref 29) as in section 12.3, an exceptionally high level of agreement being obtained (Annexe 12.5).

BG Geometry: SCF at Weld Toe

Gibstein $\{0.95 - 0.65(\beta - 0.41)^2\} \gamma^{0.39} \tau^{0.29}$
= 2.39

Kuang $1.3\beta^{-0.38} \gamma^{0.23} \tau^{0.38} \sin^{0.21} \theta$
= 2.53

Wordsworth $1.0 + 0.63\{0.75\gamma^{0.6} \tau^{0.8} (1.6\beta^{0.25} - 0.7\beta^2) \sin(1.5 + 1.6\beta)\theta\}$
= 2.80 *reducing to 2.4 at weld toe.*

TUJAP from the uncracked geometry Principal Stress (max)
Nominal stress = 2.92 Nmm^{-2}
 $6.75/2.92 = \underline{2.31}$

TWI Geometry: SCF at Weld Toe

Gibstein $\{1.01 - 3.36(\beta - 0.64)^2\} \gamma^{0.95} \tau^{1.18}$
= 8.41

Kuang $1.02\beta^{0.787} \gamma^{1.014} \tau^{0.889} \sin^{1.557} \theta$
= 6.78

Wordsworth $\beta \gamma \tau (1.6 - 1.15\beta^5) \sin(1.35 + \beta) \theta$
= 8.38

TWI = 7.78

TUJAP from the uncracked geometry Principal Stress (max)
Nominal stress = 104 Nmm⁻²
636/104 = 6.11

BG geometry; SCF due to presence of groove

Comparison of results at groove mid-point with available 2-D solutions

Roark's eqns from ref 29

Neuber's eqns from ref 30 (Neuber's Nomograph)

As welded geometry, Bending Stress/Total Stress = 0.76

Ground geometries, Bending Stress/Total Stress = 0.71

1. $d/t = 0.10$

	Neuber	Roark	SESAM (3-D)
Tension	1.48	1.61*	
Bending	1.60	1.47*	
Combined	1.57	1.50*	1.42

2. $d/t = 0.15$

	Neuber	Roark	SESAM (3-D)
Tension	1.51	1.84*	
Bending	1.69	1.71*	
Combined	1.65	1.74*	1.53

3. $d/t = 0.30$

	Neuber	Roark	SESAM (3-D)
Tension	1.74	2.01	
Bending	1.90	1.89	
Combined	1.86	1.91	1.82

* lies outwith the stated range of applicability of these eqns.

Annexe 12.3

BG geometry: reduction of fatigue life due to depth of groove

Remaining fatigue lives found from Class T, S-N curve (ref 31 fig 4.5)
and expressed as a percentage of the original life.

Nominal stress > 50 Nmm⁻²

Model	Fatigue life
as welded	100%
d/t = 0.10	29%
d/t = 0.15	23%
d/t = 0.30	13%

Nominal stress < 50 Nmm⁻²

Model	Fatigue life
as welded	100%
d/t = 0.10	13%
d/t = 0.15	10%
d/t = 0.30	4%

Annexe 12.4

TWI geometry; SCF due to presence of groove

Comparison of results at groove mid-point with available 2-D solutions

Roark's eqns from ref 29

Undeformed geometry, Bending Stress/Total Stress = 0.73

	Roark	SESAM (3-D)
Tension	2.82	
Bending	2.74	
Combined	2.76	2.77

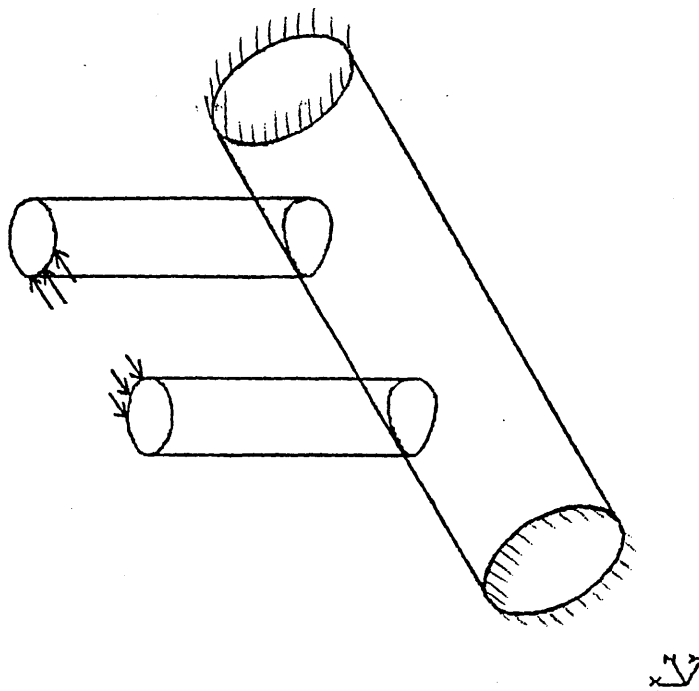


fig 12.1 British Gas experimental geometry

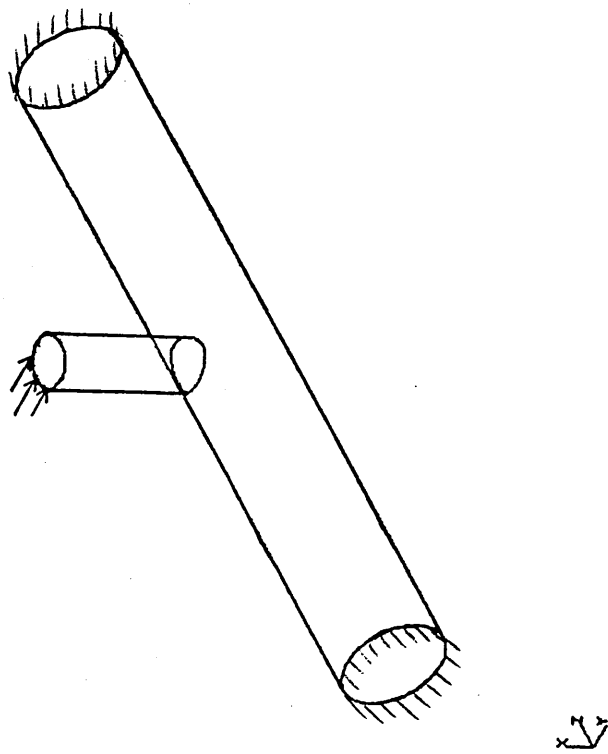
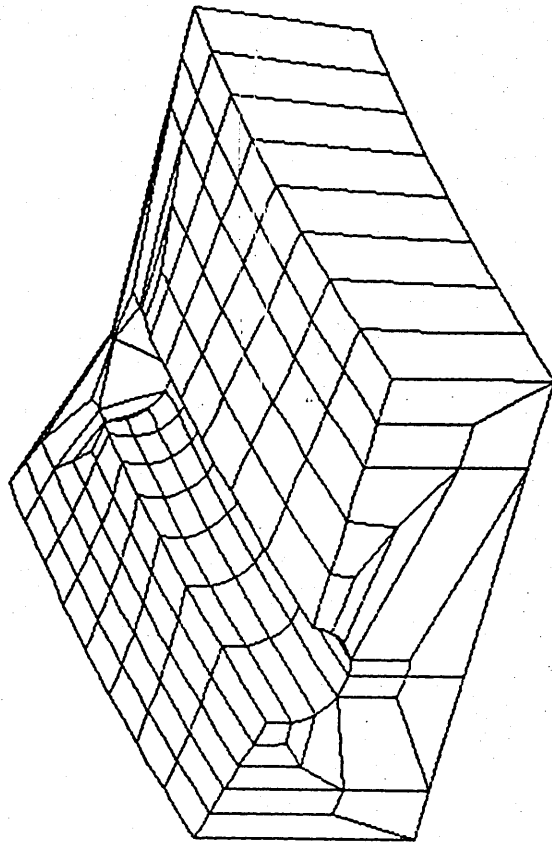


fig 12.2 The welding Institute experimental geometry



x
y
z

fig 12.3 Typical grind repair mesh

POSTFEM
> FIN
FINISH

LS1
AVERAGED NODAL VALUES
VALUES WERE CALCULATED

DATA
EYE
FINISH
HELP
INDEX
LABEL
OPTIONS
PRESENT
RESULTS
SET
VIEW

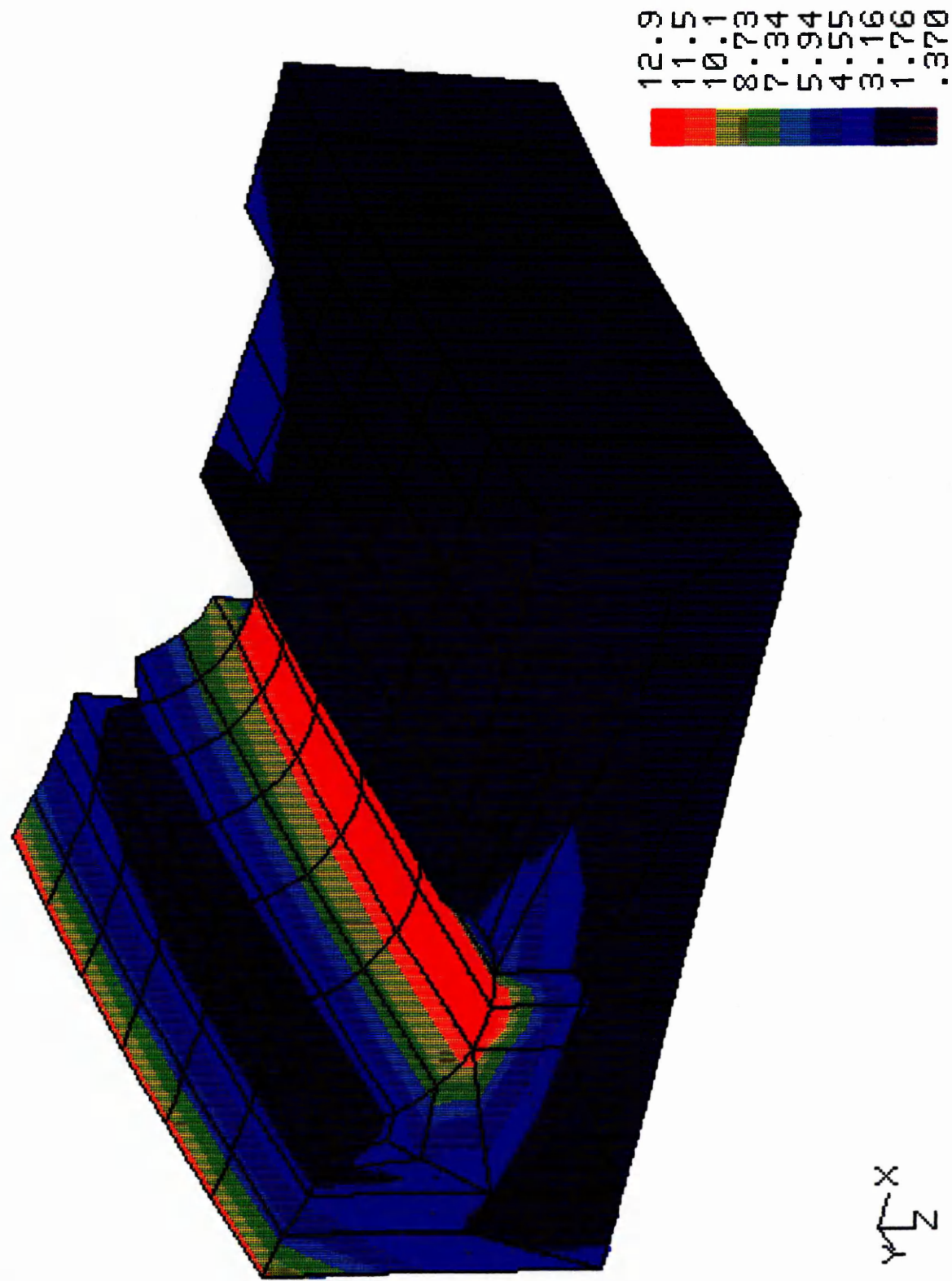


fig 12.4 Typical grind repair stress contours

STRAIN ALONG GROOVE BASE
IPB

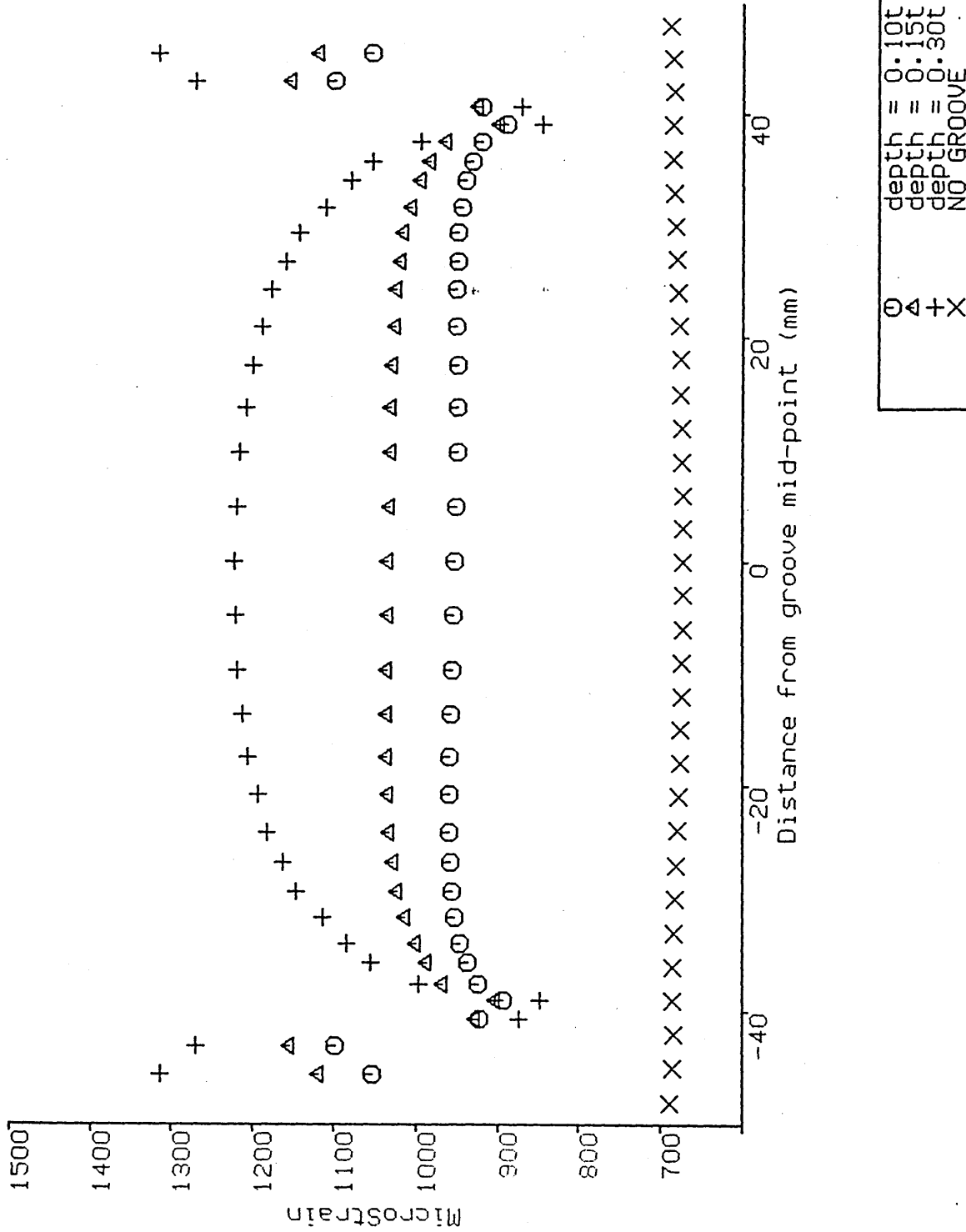


fig 12.5 Grind repair:strain along weld toe and groove base

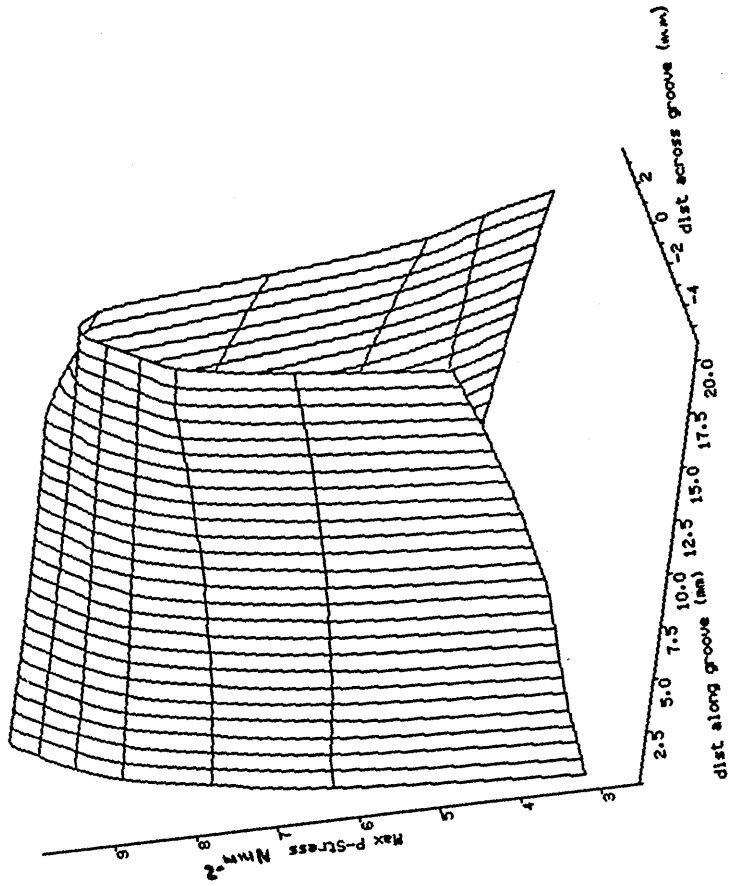


fig 12.6 Stress on groove surface

STRAIN ALONG GROOVE BASE
 IPB: Groove depth = 15%

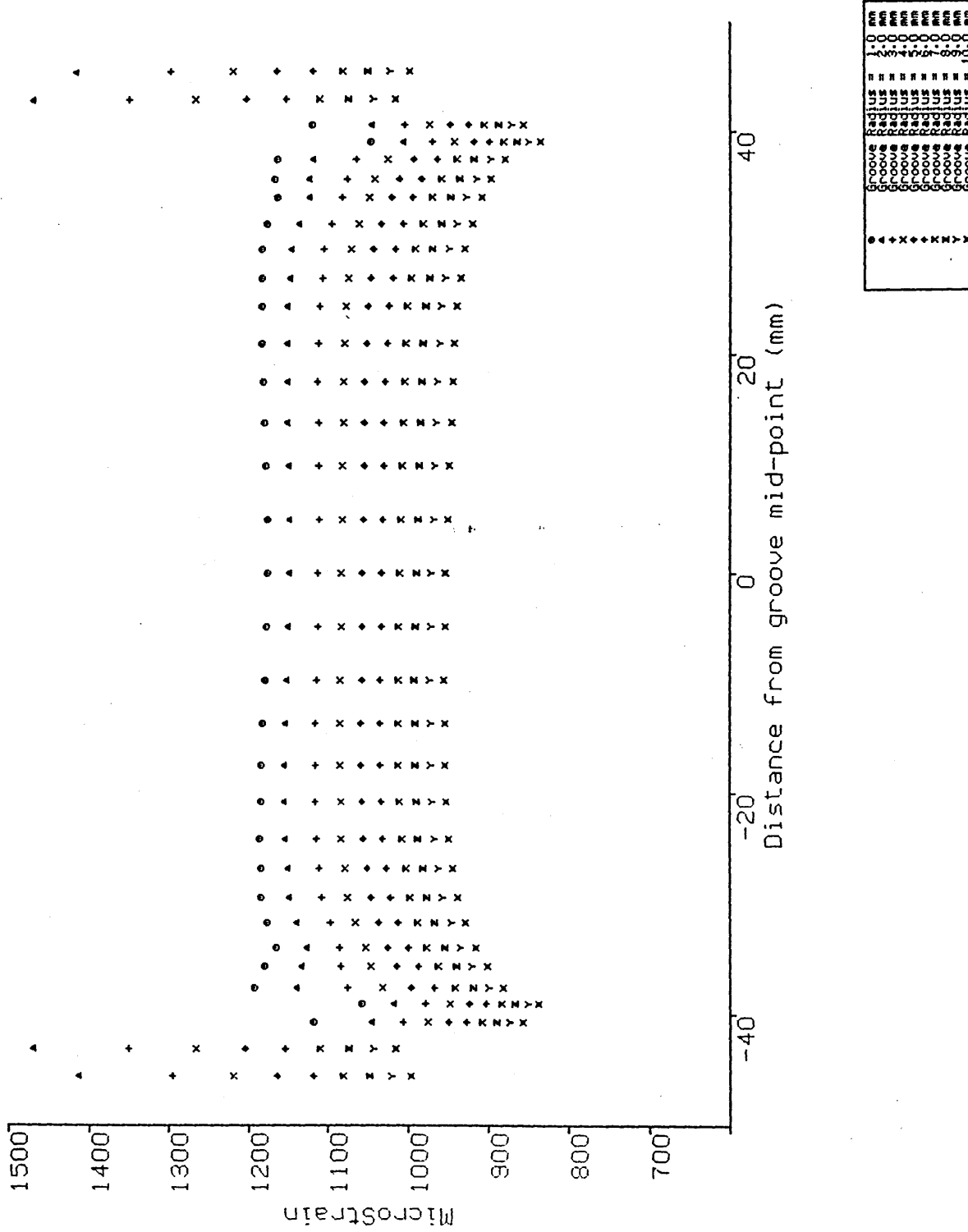


fig 12.7 Effect of varying groove radius

EFFECT OF VARYING GROOVE RADIUS

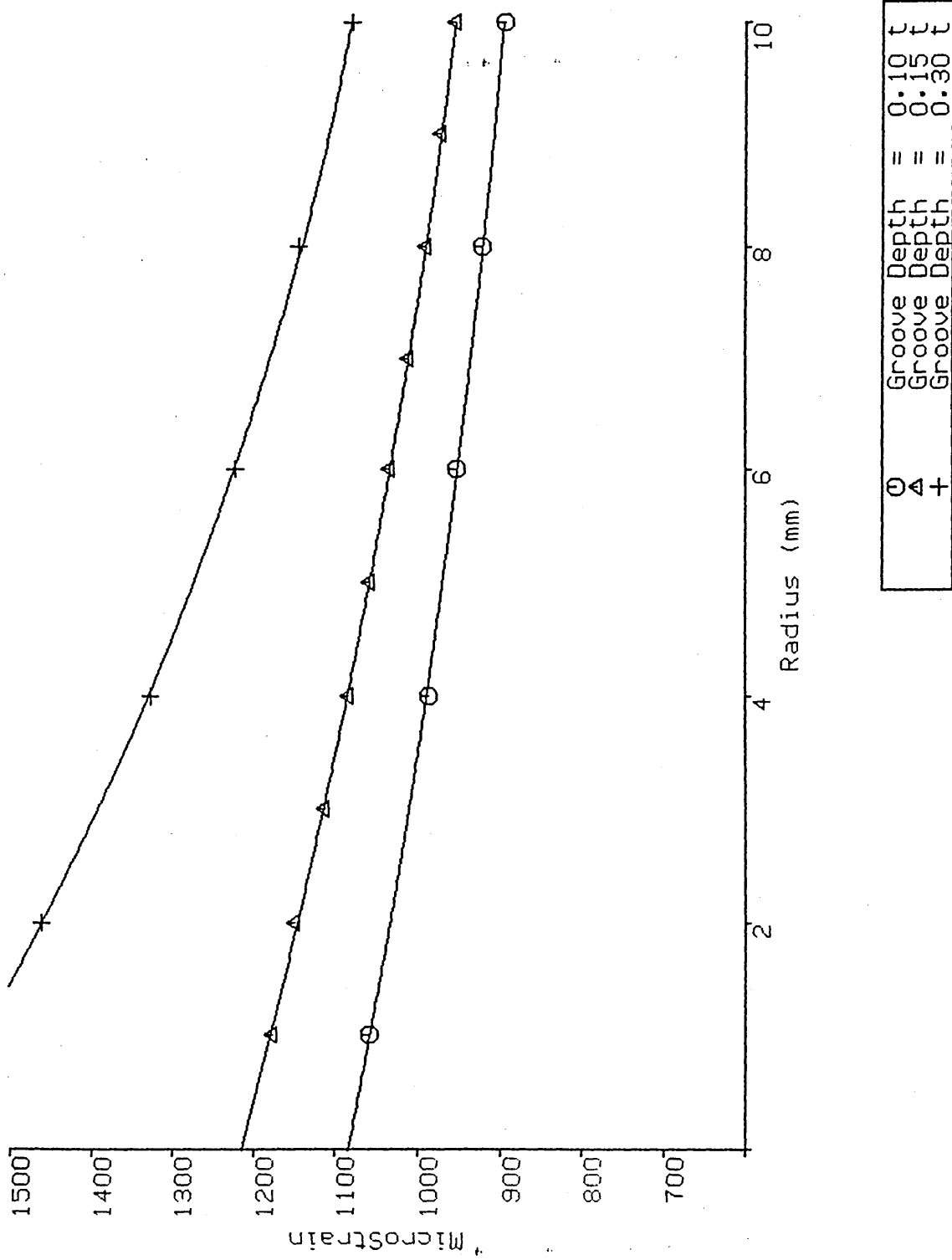
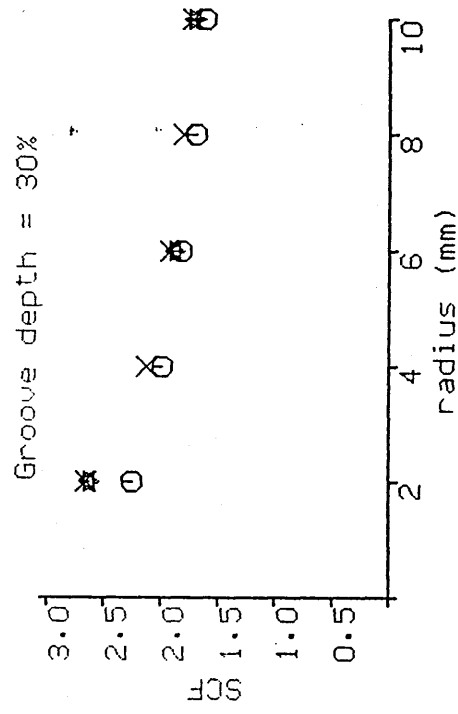
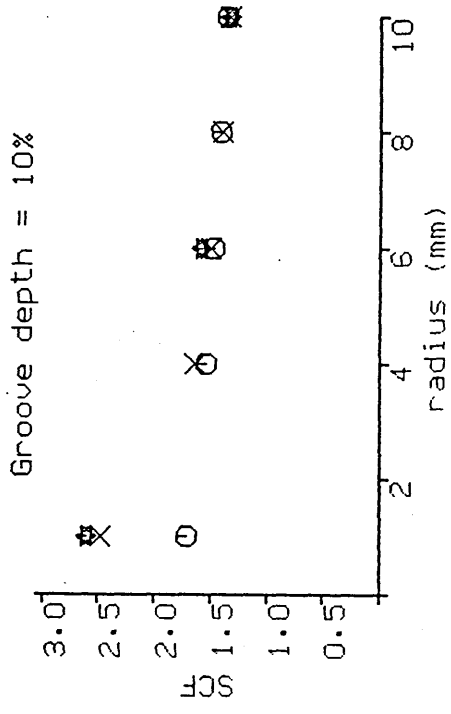
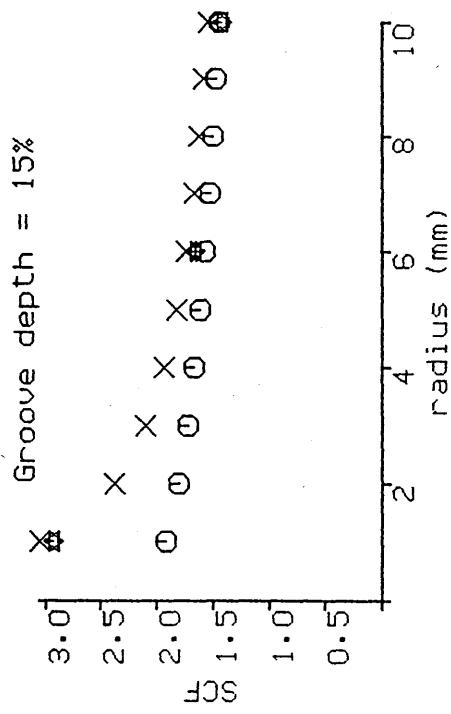


fig 12.8 Effect of varying groove radius on different groove depths



○	FE Results
×	Roark (2-D eqns)
*	Neuber's nomograph

fig 12.9 Comparison of 3-D FE results with 2-D eqns (some outside range of eqns)

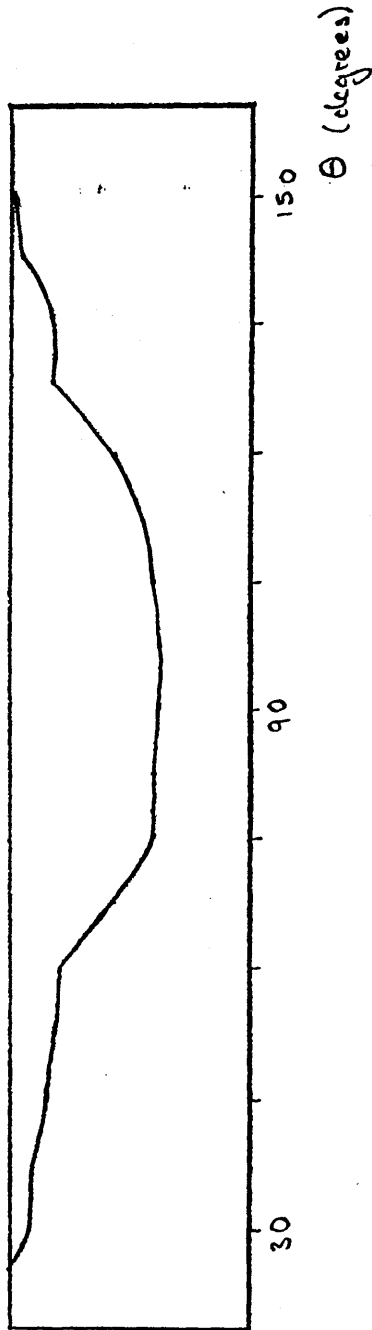


fig 12.10 The welding Institute groove geometry

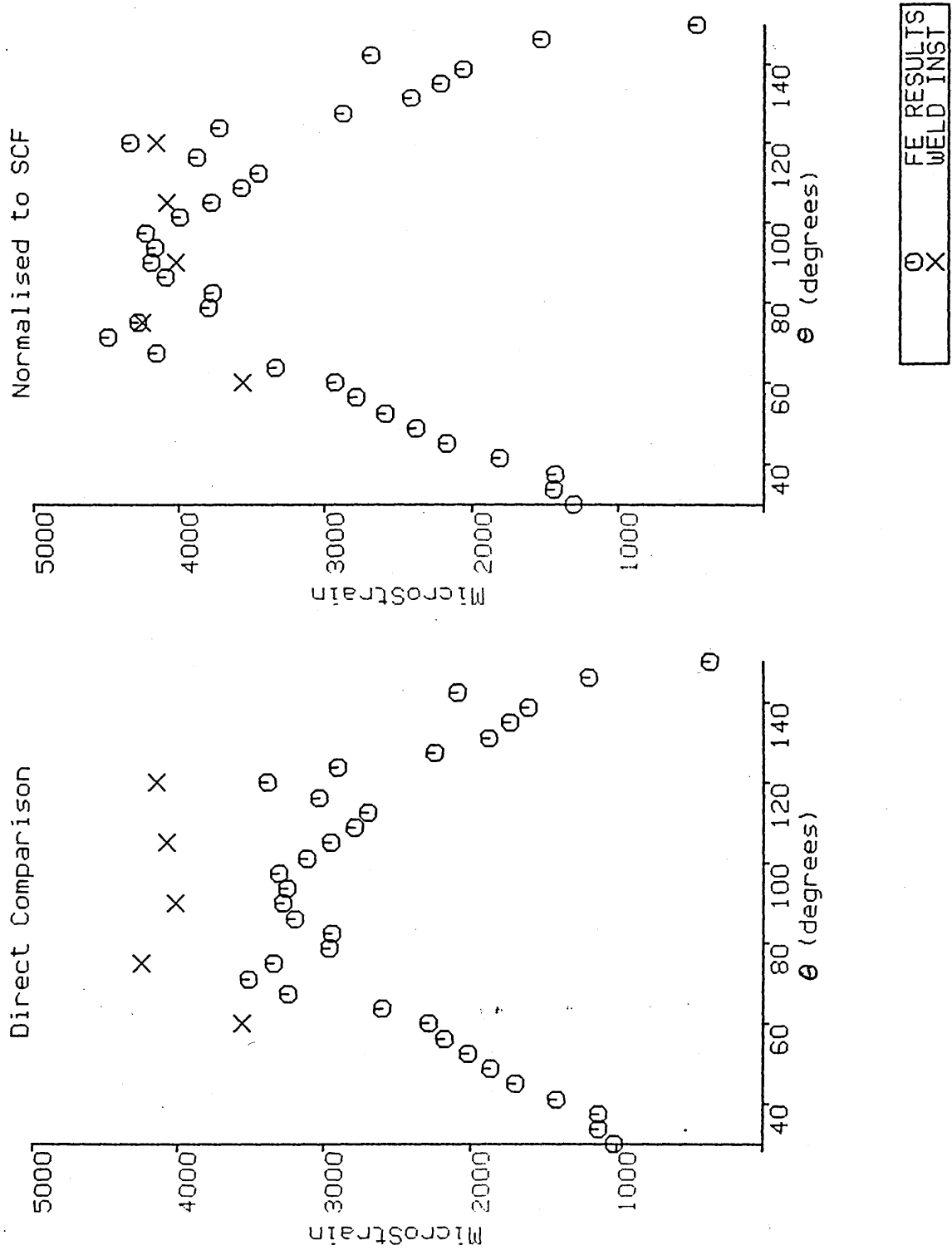


fig 12.11 Comparison of FE results with TWI experimental results

13.0 DISCUSSION AND CONCLUSION TO SECTION C

13.1 Discussion

The comparison of FE derived SCFs for tubular joints with 2-D empirical flat plate results is particularly encouraging. Although the level of agreement between 3-D FE and 2-D eqns is generally good it falls off sharply for grooves of very small radius. It is unlikely, however that very small grooves (ie radius < 3.0 mm) would be used for remedial grinding in offshore structures as it would be difficult to ensure that the full crack had been removed in one pass.

The ability of FE to model grind repairs in complex connections appears to be good, however care must be taken to allow for other factors within the model which may affect the results obtained. In this particular case the weld profile is a likely source of error (see also sect 10.1). As the ability of FE meshing techniques allows the operator to model progressively more accurately (eg details such as the groove geometry) it is important that all relevant areas of the mesh are modelled to the same degree or the results are modified to allow for the variation.

In addition, the results from the comparison with TWI highlight another problem with this field. The strain gauge results appear to be reasonably constant (within 85% of each other) yet the FE results show the detail of a much higher level of fluctuation (65%). It is likely that with an irregular groove front the strain gauges in such experiments will fail to identify local highly stressed areas. If it is to be possible, with the present level of technology, to accurately predict the SCF on a groove it is likely that more care will be required to produce a regular groove front. The local high stress areas found on an irregular groove front are analagous to the high SIFs found on irregular crack fronts (ref 33).

Although a very limited range of models has been analysed the values of SCF found are encouragingly low, all values being below 3.0. Thus, this sample implies that grind repair is a possible effective solution to some of the cases of fatigue cracking found in these joints. It should be noted, however, that in this work, the range of groove geometries are limited eg depth never

exceeded 60% of the material thickness and in all but one case was less than 30%. It is of particular significance to note that even though the SCF for a shallow grind is extremely low the slight increase in SCF caused by increasing the depth may have a significant effect on the fatigue life of the node, thus emphasising the importance of locating and treating cracks at the earliest possible stage. However the dramatic reductions in fatigue life predicted by using the T-Curve for ground joints are not borne out in practice, thus a new S-N curve is required for these joints.

This work has pointed to a number of general trends relating to the effect of varying groove depth and radius. The SCF found in the groove increases with two parameters: an increase in depth and decrease in radius. For shallower grooves the variation of SCF with groove radius is significantly less than for deeper grooves. The results obtained show very little effect due to radius for a 0.10t groove, the difference between a 1mm and 10mm diameter groove being less than 25% compared with 45% for a 0.30t groove. The corresponding difference for a 6mm groove (a size typically used offshore) and a 10mm groove is 7% and 14%. From the trend of results obtained it seems likely that there exist an optimum groove radius of the order of 20mm. It was not possible to analyse this size of groove and indeed it is likely to be too large for practical use anyway. These results imply that operators should grind as early as possible (where the SCF and radius effects are both low) and that for later, deeper cracks the operator should ensure that a reasonably large radius groove is cut.

The apparent, significant, reduction in fatigue life found due to the presence of a ground groove is at odds with accepted results in this field (ref 28). As the SCF values agree with those predicted by other methods this discrepancy is almost certainly due to an inaccuracy in the S-N curve. It would appear that the Class T S-N curve recommended for tubular welded joints (ref 31) is not appropriate for the case of a joint repaired by grinding. Considerable experimental work will need to be undertaken to allow a more accurate S-N curve to be derived.

13.2 Conclusions

The level of agreement between 3-D tubular FE and 2-D flat plate equations is generally good but falls off sharply for grooves of very small

radius.

The ability of FE to model grind repairs in tubular joints appears to be good, however care must be taken to allow for other factors within the model which may effect the results obtained.

It is likely that with an irregular groove front will have localised highly stressed areas which are extremely difficult to model accurately. Grooves should, where possible, have a regular groove front since the requirement for additional material removal is balanced by the reduction in local SCFs.

The values of SCF found in this study are all below 3.0, implying that grind repair is an effective solution to repair many cracks found in welded structures.

When using grind repair techniques the work should be carried out as early as possible to minimise the necessary groove depth. Where deeper grooves are required a larger diameter groove should be produced to reduce the stress concentration associated with deeper grooves.

The Class T, S-N curve appears not to be applicable for a welded tubular joint which has been repaired by grinding.

14.0 Overall Conclusions

The ongoing development in computing hardware and software have not yet reached the stage where it is both feasible and cost effective to consider the analysis of specific defective joints within structures with a view to assessing their effect on the fatigue life of the overall structure. While it is likely that this facility will exist in the near future, the FE analysis of such defective joints is, at present, normally used as a guide to the general behaviour of such joints rather than specific analyses of real life faults. The work covered by this thesis has contributed to this understanding in two ways. Firstly, by allowing the comparison of FE derived results with accredited results from other sources it has helped to justify the future use of FE techniques in solving these problems. Secondly, the results obtained have contributed to the extension of the existing database giving guidance to the behaviour of defective tubular welded joints.

The comparison of FE results with accepted equations and experimental results has shown a high degree of correlation. Three areas of concern are however, highlighted: application of loads; realistic boundary conditions; accurate modelling of relevant details. These are essentially problems for the analyst rather than the programmer. While in a laboratory experiment it is relatively straightforward to apply simple, easily quantifiable, loads to a specimen the loading on a true joint within a structure is invariably more complex, thus posing a greater problem for the analyst. In a similar way, boundary conditions for a joint in a full structure will be difficult to accurately assess and apply. In addition, as the FE code is used to analyse increasingly more detailed meshes it is essential that the degree of accuracy of the measurement of the joint geometry keeps pace with the mesh. Ultimately, it may be possible to analyse a complete structure using the true (as constructed rather than as designed) joint geometries thus eliminating these problems.

The specific results obtained from these analyses allow a number of inferences to be drawn. Specific conclusions on each section have been given already (sects 4, 10 & 13), however, a number of underlying threads can now be brought together. The use of 2-D solutions to analyse even relatively simple 3-D problems is fraught with danger but can be an extremely useful tool. The 2-D, typically plane strain, solutions may be significantly different

from the complex 3-D stress state. Care must be taken to validate the use of 2-D solutions in each specific area of work.

REFERENCES

1. The Welding Institute. Single Sided Welding of Closure Joints in Large Tubular Fabrications. Research Proposal, Dec 1988
2. Maddox SJ. Fitness for Purpose Assessment of Misalignment in Transverse Butt Welds Subject to Fatigue Loading. The Welding Institute Report No. 279/1985.
3. Worswick MJ and Pick RJ. Influence of Weld Misalignment and Weld Metal Overmatch on the Prediction of Fracture in Pipeline Girth welds. Int. J. Pres. Ves. & Piping, vol. 21, page 209-234, 1985.
4. Berge S & Myhre H - Fatigue Strength of Misaligned Cruciform and Butt Joints. Norwegian Maritime Research. Vol 5. April 1977
5. Burdekin FM - The effects of Deviations from Intended Shape on Fracture and Failure. Significance of Deviation from Design Shapes. I Mech E. Mar 1979
6. Petershagen H & Zwick W - Fatigue Strength of Butt Welds Made by Different Welding Processes. IIW Doc XIII-1048-82. 1982
7. Kuriyama Y, Saiga Y, Kamiyama T & Ohno T - Low Cycle Fatigue Strength of Butt Welded Joints with Angular Distortion. IIW Doc XIII-621-71. 1971
8. Andrews RM. Single Sided Welding of Closure Joints in Large Tubular Fabrications. Progress Report No. 5556/13/88. The Welding Institute, 1987.
9. Andrews RM - Private Conversation. June 1989
10. Connolly M & Dover W - Contained in Defect Assessment in Offshore Structures 1985/87. Methodology Working Group 1987
MARINE TECHNOLOGY DIRECTORATE

11. Raju JS & Newman JC - Stress Intensity Factors for a Wide Range of Semi-elliptical Surface Cracks in Finite Thick Plates. Engineering Fracture Mechanics. Vol 11, 1979
12. Du ZZ and Hancock JW - Stress Intensity Factors of Curved Semi-elliptical Cracks in a Tubular Welded Joint using Line-Springs and 3-D Finite Elements. The University of Glasgow, Internal Report, 1988
13. Hodgson CW and Thomson RD - Assessment of Fracture Mechanics Parameters for Realistic Defects in Tubular Welded Joints. International Conference on Quality Assurance and Standards in Finite Element Analysis. ^{NAFENS} Brighton 1987
14. SESAM80 TUSTRA Theoretical Manual. Veritec Marine Technology Consultants 1985
15. Hellan K - Introduction to Fracture Mechanics. McGraw-Hill, 1985
16. Huang X - A Fracture Mechanics Analysis of the Fatigue Reliability of Tubular Welded Joints. PhD Thesis. The University of Glasgow, 1986
17. Westergaard HM - Journal of Applied Mechanics. Vol 61, 1939
18. Parks DM - A Stiffness Derivative Finite Element Technique for Determination of crack Tip Stress Intensity Factors. International Journal of Fracture. Vol 10, 1974
19. Parks DM - Computational Methods in Applied Mechanics and Engineering. Vol 12, 1977
20. ABAQUS Theory Manual - Hibbitt, Karlsson and Sorensen, Inc. 1984
21. Rice JR - A Path Independent Integral and the Approximate Analysis of Strain Concentration by Notches and Cracks. Journal of Applied Mechanics. Vol 35, 1968

22. Rice JR - Mathematical Analysis in the Mechanics of Fracture. Fracture (ed by Liebowitz). Vol 2 Academic Press, New York. 1968
23. Smith RA - An Introduction to Fracture Mechanics for Engineers Part 1: Stresses Due to Notches and Cracks. Materials in Engineering Applications Vol. 1 Dec 1978
24. Department of Energy - Background to New Fatigue Design Guidance for Steel Welded Joints in Offshore Structures. ^{HMSO} 1987
25. Knott JF - Fundamentals of Fracture Mechanics. Butterworth, London 1973
26. Ritchie D & Voermans CWM - Stress Intensity Factors in an Offshore Tubular Joint Specimen. 4th International Conference on Numerical Methods in Fracture Mechanics. San Antonio, Texas. 1987
27. Rhee HC - The Behaviour of Stress Intensity Factors of Weld Toe Flaw of Tubular X-Joint. OTC. Houston, Texas. 1986
28. Grind Repair of Welded Structures - Veritec Report MP 85-3175, May 1985. ^{VSS Oslo}
29. Roark RJ & Young WC - Formulae for Stress and Strain. McGraw Hill 5th Edition 1975
30. Ugural AC & Fenster SK - Advanced Strength and Applied Elasticity. Elsevier 2nd SI Edition 1987
31. Department of Energy - Offshore Installations: Guidance on Design and Construction. 3rd Edition. 1984
32. Tubby PJ - Fatigue Performance of Repaired Tubular Joints. The Welding Institute. 1988

33. Smith IJ - The Effect of Geometry Change upon the Predicted Fatigue Strength of Welded Joints. Third International Conference on Numerical Methods in Fracture Mechanics. Pineridge Press, Swansea 1984
34. Wylde JG & Haswell J - Fatigue Performance of Fillet Welds with Toe Cracks Removed by Grinding. Fatigue of Welded Constructions. April 1987. *Conference Proceedings*
35. Hodgson CW and Cowling MJ. Interim Report on FE Analysis of Misaligned and Offset Butt Welds In Tubular Joints. Glasgow Marine Technology Centre, Jan. 1988.
36. The Welding Institute. Single-Sided Welding of Closure Joints in Large Tubular Fabrications. Research Proposal, Dec. 1985.
37. Buisman BC & Scholte HG - Investigation of the Fatigue Behaviour of a butt Welded Tubular Connection with Root Defects. Steel in Marine Structures. Elsevier Science Publishers. Amsterdam 1987
38. Department of Energy - Background to New Guidance on Structural Steels and Steel Construction Standards in Offshore Structures Welded Joints in Offshore Structures. 1987
39. Dover WD and Dharmavasan S - Fatigue fracture Mechanics Analysis of T and Y Joints. Offshore Technology Conference, Houston 1982
40. Ingrassia AR and Manu C - Stress-Intensity Factor Computation in Three Dimensions with Quarter Point Elements. International Journal for Numerical Methods in Engineering. Vol 15, 1980
41. Kumar, German MD and Shih CF - An Engineering Approach for Elastic-Plastic Fracture Mechanics . Electric Power Research Institute 1981
42. Rice JR and Levy N - The Part Through Surface Crack in an Elastic Plate. Journal of Applied Mechanics, 1972

43. Tada H, Paris P and Irwin G - The Stress Analysis of Cracks Handbook. Del Research Corporation , St Lious 1973
44. The Welding Institute - Faults in Fusion Welds in Constructional Steels. Introductory Notes, Welding Technology Slides, Set 2. 1975

